Universitat Autònoma de Barcelona

DEPARTAMENT DE FÍSICA
INSTITUT DE CIÈNCES DE L'ESPAI (IEEC/CSIC)

MEASURING LARGE SCALE STRUCTURE USING ANGULAR CROSS-CORRELATIONS

by

JACOBO ASOREY BARREIRO

ADVISORS

HECTOR MARTÍN CROCCE
ENRIQUE GAZTAÑAGA BALBÁS

TUTOR

ENRIQUE FERNÁNDEZ SÁNCHEZ

Barcelona, July 2013

MEASURING LARGE SCALE STRUCTURE USING ANGULAR CROSS-CORRELATIONS

Memòria presentada al Departament de Física de la Universitat Autònoma de Barcelona per **Jacobo Asorey Barreiro** per a optar al grau de Doctor en Física

JACOBO ASOREY BARREIRO

ADVISORS

Dr. H. MARTÍN CROCCE
Dr. ENRIQUE GAZTAÑAGA BALBÁS

TUTOR

Dr. ENRIQUE FERNÁNDEZ SÁNCHEZ

Bellaterra, Juliol de 2013.

Para mis padres

Acknowledgments

En primer lugar, quiero agradecer a Enrique su confianza en mi para iniciar esta aventura y abrirme la puerta para poder introducirme en este Universo. Le agradezco que me haya transmitido su experiencia y conocimientos y por guiarme durante estos años. A Martín, gracias por su paciencia, su apoyo, sus consejos, dedicación y esfuerzo y por sus siempre útiles prácticas sugerencias. Sin ellos, no habría sido posible. Debo agradecer a Enrique Fernández que haya sido el tutor de esta tesis.

También quiero agradecer a Anne, Christopher, Francisco, Jorge, Pablo, Ricard, Sam, Santi, Steph y a todos del grupo de cosmología por ayudarme siempre, por responder a mis preguntas y por hacer el trabajo y las asistencias a congresos grandes experiencias.

I want to express my gratitude to Antony Lewis for hosting me during the amazing month at Sussex where I learn a lot and for collaborating with me afterwards. I also want to thank everybody that I met during my stay there because they made me feel comfortable. I am also thankful to Ofer Lahav for allowing me to visit UCL during almost two months. It was a really good experience and allow me to learn new skills, for which I am especially grateful to Cris Sabiu. Thanks to all the wonderful people that I met there for making my stay at the pre-olimpic London unforgettable.

Tengo que agradecer al programa JAE del CSIC, co-financiado por el Fondo Social Europeo, el soporte económico durante estos años. El agradecimiento es extensible a los contribuyentes que lo han hecho posible. Quiero dar las gracias a Alina, Delfi, Guadalupe, Isabel, Josefa y Josep por solucionar siempre mis problemas administrativos e informáticos. También le debo eterno agradecimiento a las personas que recuperaron mi ordenador de trabajo después de su “traslado”, con el consiguiente ahorro de tiempo.

No puede faltar la alusión a los que me ayudaron a mantener el cyber caliente en invierno y frio en verano: Albert, Antonia, Arnau, Carlos, Daniela, Elsa, Felipe, Jonatan, Jorge, Kai, Kike, Martin, Nataly y Nikos, ni a Andreu, Ane, Antonio, Pau y Pris; ni a la banda del IFAE, Adiv y Alicia, ni a los lamas. Que grandes momentos he pasado con todos vosotros. Gracias a todos por hacer mis años en Barcelona una inolvidable experiencia. Por supuesto, siempre recordaré las charlas de café con Diego, intentando resolver todas las cuestiones sin encontrar ninguna respuesta. A

mis compañeros del últimos año en el ETSE, muchas gracias por crear un estupendo clima en la oficina. Vull agraïr als meus companys de master y de català que em fessin tan fàcil el primer any a Barcelona.

Le debo mucho a mis compañeros badalianos: Alejandro, Alberto y Rubén, por hacerme tan fáciles estos aos de convivencia y por aguantar mis periodos insportables (y los soportables). Echaré mucho de menos los momentos con vosotros. He aprendido mucho sobre todo con vosotros y me he hecho más mayor, emocionalmente.

Gracias a mis compañeros de universidad en Zaragoza y Southampton por hacerme tan llevadero el paso de tantos años de aprendizaje. Quiero agradecer a Margarita García por acogerme en mi primera experiencia laboral en ciencia. Agradezco a todos los profesores que han contribuido a mi educación académica. Le debo muchos conocimientos y felicidad a todos los veranos que he pasado en Benasque y a todas las personas que me han cuidado. Por último, quiero agradecer a mis amigos maños su apoyo, fidelidad y sana locura. Quero agradecerlle a miña familia o afecto que sempre me tiveron y pola sua maneira de ser. Especialmente, quiero agradecer a mis padres su eterna confianza en mi, sus críticas constructivas, su apoyo, su paciencia, su cariño por transmitirme el amor por la ciència y por las cosas buenas de la vida (y advertirme de las malas). Y por saber que siempre estáis ahí para ayudarme.

We are but warriors for the working-day;
Our gayness and our gilt are all besmirch'd
With rainy marching in the painful field;
There's not a piece of feather in our host–
Good argument, I hope, we will not fly–
And time hath worn us into slovenry:
But, by the mass, our hearts are in the trim;

Henry the fifth, Act IV, Scene III, W. Shakespeare

We often think that when we have completed our study of one
we know all about two, because "two" is "one and one."
We forget that we still have to make a study of "and."

Arthur S. Eddington

Abstract

In this thesis we propose to use galaxy clustering, more concretely angular cross-correlations, as a tool to understand the late-time expansion of the Universe and the growth of large-scale structure.

Galaxy surveys measure the position of galaxies (what traces the dark-matter field) in spherical coordinates (z,θ,ϕ). Most galaxy clustering analyses convert these positions to distances assuming a background cosmology. This approach thus requires doing the full data analysis for each background cosmological model one wants to— test. Instead we propose to select galaxies in radial shells, according to their redshifts, and then measure and analyze the angular (2D) correlations in each bin circumventing the model assumption.

On the one hand our approach projects and looses 3D information along the line-of-sight for distances smaller than the shell width. On the other hand, it allows a single analysis, as no cosmological model needs to be assumed. Remarkably we find that if we include in the analysis also the angular cross-correlations between different shells, we can recover the radial modes corresponding to the separations between radial bins. We found that the optimal binning to recover 3D information is given by the largest between the minimum scale considered for spatial clustering, $2\pi/k_{max}$, and the photometric redshift error.

Photometric galaxy surveys, such as Physics of the Accelerating Universe (PAU) and Dark Energy Survey (DES), access higher number densities and higher redshifts than current spectroscopic surveys, at the price of loosing radial accuracy. Angular analysis in redshift bins is then the natural framework for such surveys.

We found that, for such photometric surveys, the constraints on the growth index of structure improve by a factor two when we include the cross-correlations. In addition, we show that one can use two different galaxy populations to trace dark matter and hence reduce sample variance errors. The cross-correlations of both populations in the same field leads to an overall gain of a factor five. This allows measurements of the growth rate of structure to a 10% error at high redshifts, $z > 1$, complementing low-z results from spectroscopic surveys. This gain is maximized for high bias difference and high densities.

We also worked with N-body simulations to include non-linear gravitational effects and turn them on and off (e.g redshift space distortions or the radial distortions produced by photometric redshifts). We built galaxy survey mocks from the MICE simulations and measure galaxy clustering to compare with our previously mentioned models of angular correlations. We found a good agreement between theory and simulation measurements.

In the future, we expect to apply this framework for cosmological parameter estimation, especially focusing on DES and PAU surveys.

Resumen

En la tesis, proponemos usar el estudio de la agrupación de las galaxias, en particular usando correlaciones cruzadas angulares, para entender la etapa tardía de expansión del Universo y el crecimiento de estructura a gran escala.

Los cartografiados extragalácticos miden la posición de las galaxias (que son trazadores del campo de materia oscura) en coordenadas esféricas (z,θ,ϕ). Muchos análisis de la distribución de galaxias convierten estas coordenadas en distancias, asumiendo una cosmología. Este tipo de análisis requiere rehacer todo el análisis de las medidas para cada modelo cosmológico con el que se quiera comparar. Como alternativa, proponemos seleccionar las galaxias en intervalos radiales, de acuerdo a la medida de sus desplazamientos de longitud de onda al rojo, z, para posteriormente analizar las correlaciones angulares (2D) en cada intervalo.

Mediante esta manera de abordar el análisis se pierde información 3D a lo largo de la línea de visión, para escalas menores que la anchura de cada intervalo. Pero evitamos tener que asumir ningún modelo cosmológico de partida. Hemos visto que un análisis basado en funciones angulares de correlación cruzadas entre diferentes intervalos puede recuperar los modos radiales correspondientes a separaciones dadas por la distancia entre bines. La división en intervalos óptima para recuperar la información 3D viene dada por la escala mínima considerada en el análisis espacial, $2\pi/k_{max}$, y por la escala dada por el error en el z fotométrico.

Los cartografiados extragalácticos fotométricos, como Physics of the Accelerating Universe (PAU) y el Dark Energy Survey (DES), nos permiten acceder a mayores densidades de galaxias y a zonas más profundas del Universo que las alcanzadas en los cartografiados espectroscópicos actuales, pero perdiendo resolución radial. El análisis angular en distintos intervalos es la manera natural de analizar este tipo de cartografiados.

Hemos visto que, para este tipo de cartografiados, la determinación del índice de crecimiento de estructura mejora un factor dos si incluimos las correlaciones cruzadas. Además, mostramos que si usamos dos poblaciones de galaxias como trazadores de materia oscura reducimos la varianza cósmica. Usando las correlaciones entre ambas poblaciones en el mismo área, los resultados mejoran un factor cinco. Esto nos permite determinar a un 10% el crecimiento de estructuras para $z > 1$, lo que nos permite complementar

los resultados a bajo z obtenidos mediante espectroscopía. La ganancia se magnifica para trazadores que se agrupen de manera muy diferente y con alta densidad.

Hemos usado simulaciones de N-cuerpos para incluir efectos no lineales, de manera que podemos activarlos o desactivarlos (como las distorsiones en el espacio de z o las debidas a z fotométricos). Se han construido catálogos a partir de las simulaciones MICE para medir el agrupamiento en la distribución de galaxias, comparándolo con los modelos teóricos de las correlaciones angulares. Hemos hallado una buena correspondencia entre ambos.

Los planes futuros pasan por utilizar esta metodología para la estimación de parámetros cosmológicos, particularmente para DES y PAU.

Contents

Chapter 1

Introduction

The roots of our present understanding of the Universe date back to the first three decades of the XX century. When Einstein developed General Relativity he realized that it was possible, for the first time, to describe in mathematical terms the Universe as a whole by means of a relativistic theory of gravity. In 1917, he published the first paper giving a static solution for the background gravitational field of the Universe. Very soon, after Einstein's proposal, Alexander Friedmann found a different solution of Einstein's equations for a homogeneous and isotropic universe. In that solution the Universe was expanding. In the twenties Lemaître found the same solution that Friedmann but he used the measurements of the recession velocity of nearby galaxies and the distances to them, obtained using the cepheid period-luminosity relations, to show that the solution provided by Friedmann was a realistic description of the Universe. Some years later Hubble used more observational data to show that the recession velocity of galaxies is proportional to their distance, as in an expanding Universe is expected. Finally, Robertson and Walker constructed the metric tensor that describes homogeneous and isotropic Universes. Currently, the most extended model for the background Universe is the Friedmann- Lemaître-Robertson-Walker (FLRW) Universe where the background gravitational metric is defined by a curvature parameter while the temporal evolution is described by a function of time called scale factor. In energetic terms, the Universe was dense and hotter in the past.

In 1965, Penzias and Wilson, detected the *Cosmic Microwave Background Radiation* (CMB), which is the cooled remnant of the photons that decoupled from baryons when the Universe was nearby 400 000 years old. The existence of this radiation is a proof of the Hot Big Bang model, together with the abundances of light elements. In 1992, COBE satellite observed the anisotropies of order $O(10^{-5})$ in the temperature of the CMB. The fact that we live in galaxies implies that the Universe, at perturbative level, is not completely homogeneous. Therefore, CMB anisotropies encode the state of this inhomogeneities at early-time expansion.

At the end of the last century, the measurements of the expansion rate, using type Ia Supernova, pointed out that the expansion is accelerated. Therefore, to account for this acceleration, a new energy component called dark energy was added to the cosmological inventory. A particular explanation for dark energy consists on adding a cosmological constant to Einstein's equations, as an energetic component, (Zeldovich 1968; Weinberg 1989). The negative pressure of the dark energy would produce the accelerated expansion. Nowadays, the most important cosmological problem consists on understanding the nature of dark energy, (Albrecht et al. 2006; Weinberg et al. 2012).

The scope of this thesis is the analysis of galaxy clustering, as a probe of large scale structure of the Universe, using angular auto and cross-correlations between radial shells. What extragalactic surveys catalogues contain is a three-dimensional map of the galaxy distribution. As galaxy trace the matter density contrast field, they provide a great tool to study the spectrum of inhomogeneities at the late-time expansion of the Universe, which is the era in which dark energy rules the accelerated expansion.

Those three-dimensional maps are obtained determining the angular position of the galaxies and the redshift. The latter is the shift on the observed wavelengths of a galaxy with respect to the rest frame emitted wavelengths due to the expansion of the Universe.

Therefore, the natural analysis would be in the spherical coordinates given by the redshift, as a tracer of the distance to each galaxy and the two angular coordinates that determine the positions in the sky of galaxies covered by the camera when developing a survey. Since the beginning of the first redshift surveys, the most common approach to clustering analysis have been a 3D approach, that used the survey volume to determine how the clustering of galaxies differ from a random distribution. Galaxies are distributed, in the linear regime, according to the matter field. The theoretical description of the growth of structure and the evolution of the primordial spectrum of inhomogeneities during the expansion history of the Universe is a 3D picture. Then, a priori, it is easier to compare directly with theory using cartesian or Fourier space.

But, we are limited by the observational constraints and in this case the main one is that if we want to convert the (z, θ, ϕ) coordinates in distances, we have to assume a fiducial cosmology for the expansion history. Hence, we are biasing the analysis, in terms of determination of cosmological parameters. In order to account for the distortions introduced by this biasing, the Alcock-Paczynski effect, (Alcock C., Paczynski B. 1979), the cosmological constraints are obtained after adding the factors that describe the distortions for radial and transverse modes.

There is a much natural approach, consisting on selecting the galaxies in different redshift bins and then statistically measure the angular distribution of clustering, compared with a random distribution. In this case, we are projecting the radial information, loosing the modes corresponding to distances smaller than the radial shell width. But we can include in the observables, the measure of the correlation between the different radial shells. That would introduce the radial modes accounting for the separation of the bins. Depending on the bin width, the radial resolution accounted by this *tomographic analysis* of the survey volume will improve or not. In this thesis, we studied this from the parameter estimation point of view. We explore at which width the parameter constraints from 3D analysis are recovered using the 2D tomography.

In redshift space, galaxy positions are distorted with respect to the real positions because of their peculiar velocities. At linear scales, the divergence of peculiar velocities is given by the density contrast. This introduces an anisotropy in the radial direction, (Kaiser 1987) that depends on the growth history, for a given background expansion history. It is expected that the combination of redshift distortions with lensing measurements would allow us to compare dark energy models with modify gravity theories, (Reyes et al. 2010; Gaztañaga et al. 2012; Cai & Bernstein 2012). Then, it is known that if we use two tracers of matter in redshift space, as for example luminous red galaxies and emission line galaxies, we are oversampling radial and transverse modes, reducing sample variance, (McDonald & Seljak 2009). This studies have been usually done in 3D space. We propose to use the same approach but using angular correlations. This is mainly motivated by the fact that the two tracers approach depends strongly on the shot noise of the different samples. Photometric surveys are designed in order to have a high number density and to reach deeper redshifts. But, as radial information is randomly affected by the photo-z we should bin the redshift range and study the projected correlations. The fact that the top-hat edges in redshift space differ from the boundaries in real space allow enhances the amplitude of clustering at large angles, as given by redshift distortions, (Nock, Percival,& Ross 2010; Crocce, Cabré, & Gaztañaga 2011; Ross et al. 2011; Asorey et al. 2013). We forecast the constraints that a survey such as Dark Energy Survey (DES) or the Physics of the Accelerating Universe Survey (PAU).

Finally, in order to be ready for the analysis of the data delivered by DES or PAU when available, we go further than forecasting by comparing the model for the angular correlations with the measured angular and cross-correlations from a lightcone output of the MareNostrum Institut de Cinces de l'Espai simulations (MICE).

In chapter 2 we describe the cosmological model and the large scale structure. In chapter 3 we show the optimal binning that allows 2D tomography to recover 3D information, in linear theory. Then, in chapter 4 we consider how to determine the growth history using different galaxy samples from photometric surveys. Finally, we compare the model assumed in this thesis with the output of a N-body simulations, in order to improve the layers of reality in the study.The results presented in chapters 3 have been published in the article (Asorey et al. 2012) and the results shown in chapter 4 have been submitted for publication, (Asorey et al. 2013)

Chapter 2

Cosmological Model and Large Scale Structure

In this chapter we summarize the main aspects of the ΛCDM cosmological model which are relevant for the galaxy clustering analysis that will be introduced in next chapters. The presentation is essentially based on the references cited in the text.

2.1 Background expanding Universe

The most likely description of the Universe is based on the *Cosmological Principle*. This principle states that the Universe is homogeneous and isotropic, at order zero. With this principle, the metric g_{ij} of the Einstein's equations is fully described by the scalar factor $a(t)$ and the sign of the curvature of the Universe, k, that is positive, negative or zero wether the Universe is closed, open or flat. In this thesis we assume that the space is flat as has been granted by the analysis of the anisotropies of Cosmic Microwave Background Radiation (CMB), (Lange et al. 2001; Jarosik et al. 2011).

The conformal FLRW metric for a flat Universe is given by

$$ds^2 = a(\eta)^2 \left(d\eta^2 - \delta_{ij} dx^i dx^j\right) \tag{2.1}$$

in terms of the conformal time

$$\eta = \int \frac{dt}{a(t)}, \tag{2.2}$$

where $a(\eta)$ the scale factor, normalized to 1 today. If not explicitly stated otherwise, we use natural units ($\hbar = c = k_B = 1$)

If $\bar{\rho}$, $\bar{p}$ are the energy density an pressure of all the cosmological background fluids with energy momentum tensor given by

$$T^{\mu}{}_{\nu} = (\bar{\rho} + \bar{p}) u^{\mu} u_{\nu} - p\, \delta^{\nu}{}_{\nu}. \tag{2.3}$$

where the 4-velocity in the background is $u^\mu = (1,0,0,0)$ and $\sqrt{u^\mu u_\nu} = 1$.

In such a cosmological background, Einstein's equations reduce to Friedmann's equations

$$a'' = \frac{4\pi G}{3}(\bar{\rho} - 3\bar{p})\,a^3, \quad (a')^2 = \frac{8\pi G}{3}\bar{\rho}\,a^4, \tag{2.4}$$

where the primes denote the derivatives with respect to the conformal time η. Usually, the expansion history of the Universe is parametrized using the Friedmann parameter

$$H = \frac{1}{a}\frac{da}{dt}, \tag{2.5}$$

$$\mathcal{H} = \frac{da}{d\eta} = aH \tag{2.6}$$

where (2.5) is usually the definition of the Hubble parameter while (2.6) gives the same information but we are using conformal time, given by (2.2). This quantity is crucial in order to know the rate of expansion at each epoch. It appears in every geometrical factor.

Let us define the comoving distance traveled by light from the emitter to us

$$r(z) = \int_0^z \frac{dz}{H(z)} \tag{2.7}$$

where we have introduced the shifts on the wavelengths due to the expansion of the Universe, the redshift z. In the next chapters, we usually use redshift as the temporal variable because this is what is measured in galaxy surveys.

From conservation equation, given by ${T^\mu}_{\nu,\mu} = 0$, we can extract the equation of conservation of energy and the continuity equation. Therefore, in the expanding Universe, the conservation law

$$\frac{\partial\bar{\rho}}{\partial\eta} + H(\bar{\rho} + 3\bar{p}) = 0, \tag{2.8}$$

tell us how the energy evolves with time. Depending on which component dominates the evolution at each time, the evolution would be different.

From the above equations one can entirely describe the evolution of the expansion of the background Universe. The Universe is made up of photons and relativistic matter, neutrinos, non-relativistic baryons, non-relativistic pressureless dark matter and a dark energy component, with negative pressure, which is the main problem to solve in modern cosmology. The critical density,

$$\rho_c(t) = \frac{3H^2(t)}{8\pi G},$$

is the total energy-density of a flat Universe. Usually, instead of the background densities for the other fluid components of the Universe we use the ratio of each density with respect of the critical density. We can rewrite Friedmann equation as

$$H^2(t) = H_0^2 \Omega(t) \tag{2.9}$$

with

$$\Omega(t) = \sum_x \frac{\rho_x(t)}{\rho_c(t)},$$

the sum running over the different components of the energy-momentum tensor, $x = \{\mathrm{rad}, \mathrm{mat}, \mathrm{DE}\}$. H_0 is the Hubble constant which is defined as the Hubble parameter at current time. Therefore, $\Omega = 1$ today. This allow us to parametrize the energy content of each component as $\Omega_{r_0}, \Omega_{m_0}, \Omega_{DE_0}$. If the nature of dark energy is the cosmological constant Λ, then $\Omega_{DE_0} = \Lambda/3H_0^2$. Those are the relevant parameters that describe the expansion of the Universe. One of the main goals in observational cosmology consists on constraining these parameters.

Finally, from equation (2.8) we can define the evolution with the expansion of the different density parameters:

$$\Omega_r(a) = \Omega_{r_0} a^{-4} \frac{H_0^2}{H(a)}, \quad \Omega_m(a) = \Omega_{m_0} a^{-3} \frac{H_0^2}{H(a)}, \quad \Omega_{DE}(a) = \Omega_{DE_0} \frac{H_0^2}{H(a)}. \tag{2.10}$$

At different times the expansion of the Universe is driven by different energy components. According to this, those are the different epochs in terms of expansion history.

i) Radiation-dominated era

According to the conservation law (2.8), the evolution of radiation density parameters is given in equation (2.10). At early times the Universe was radiation-dominated. When $a_{eq} = 10^{-4}$ the Universe became matter dominated because the radiation energy density is diluted faster than the matter energy density. This equality depends on the current ratio between radiation and matter density parameters today. Let us recall that by radiation we also mean relativistic particles.

At this stage, the horizon grows very fast and therefore the smaller superhorizon scales re-enter into the observable Universe. During this phase, baryons are tightly coupled to photons. This would affect strongly the growth of structures because there is a suppression of clustering at the scales that re-enter into sub-horizon region at that time. This is reflected in the current distribution of inhomogeneities at linear scales where we can observe this suppression of the quasi-scale invariant power spectrum of matter inhomogeneities produced at the end of Inflation.

ii)Matter-dominated era

During matter-dominated expansion, the energy of photons continue to decrese and at $a_{rec} = 10^{-3}$ protons and electrons are able to bind together and form atoms. Then, the Universe became transparent and releases the photons that are observed today, much cooler, in the Cosmic Microwave Background Radiation. As gravity is the only force acting on cold dark matter and baryons only interact with photons through Thompson scattering, inhomogeneities grow linearly with the scale factor because the initial overdensities attract more and more matter as time increases.

iii)Dark Energy era

Since the density of dark energy $\bar{\rho}_{de}$ is constant when its equation of state is $w = -1$, as expected from a cosmological constant origin at some moment with small redshift ($z < 1$) the Universe starts to be driven by Dark Energy. This is a fluid with negative pressure which in the ΛCDM case corresponds to a cosmological constant in Einstein equations. Because of the negative pressure, the expansion is accelerated. According to this, recent observations show that the Universe is 13.8 Gyr old and the Dark Energy era last till nowadays.

2.2 Inflation and Initial Conditions

The most accepted scenario for the evolution of the Universe at early times is *Cosmic Inflation* (Starobinsky 1980; Guth 1981; Starobinsky 1982; Albrecht& Steinhardt 1982; Linde 1982; Linde 1983). According to this theory, at early times the expansion of the Universe was accelerated in a similar way to todays Dark Energy era due to negative pressure of the universe, generated in that case by a scalar field, the inflaton, decaying into the minimum of a potential with a small kinetic term (slow roll inflation).

This initial accelerated exponential expansion allowed all the regions of the universe that are not apparently causally connected to become connected. In inflationary models, the output is always a flat Universe.

In terms of large scale structure studies, the most interesting outcome of Inflation is that it provides an explanation for the origin of inhomogeneities in the Universe, (Mukhanov & Chibisov 1981; Hawking 1982; Guth & Pi 1982; Starobinsky 1982; Bardeen, Steinhardt & Turner 1983). The existence of quantum fluctuations during Inflation generated perturbations of the LFRW metric that are the seeds of current inhomogeneities. In this work we shall restrict ourselves only to scalar perturbations because they are directly connected with matter inhomogeneities.

Nowadays, from all the alternatives, inflationary cosmology fits better current observations (Planck Results XXII 2013). Among Inflation scenarios there are different models, depending on the number of scalar fields or the mechanism that stops Inflation (graceful exit). Note that, despite the fact that Inflation fits well with data, it is not a completely confirmed scenario.

At the end of inflation, in terms of structure formation the value set for the gravitational potential for scales greater than the horizon is frozen.

This is the primordial potential that leads to the initial power spectrum of scalar perturbations. For the modes corresponding to the smaller scales, their horizon crossing occurs when the Universe is radiation dominated they are diluted which explains the suppression of the spectrum of these smaller scales. The information of how the amplitude of each mode is suppressed is given by the *transfer function* $T(k)$. Inhomogeneities with scales greater than the modes with the size of the horizon at matter-radiation equality, are preserved and generate the primordial power spectrum because they crossed the horizon when the Universe was matter-dominated and for them the transfer function is the unity. They only have a linear growth factor due to gravitational instability.

Primordial Matter Power Spectrum

The inflationary prediction for the primordial power spectrum of curvature perturbations is given by a power law

$$P_0(k) = A_s k^{n_s - 1} \tag{2.11}$$

where n_s is the spectral index and A_S a normalization amplitude. If $n_s = 1$ the power spectrum is scale invariant and is known as Harrison-Zeldovich power spectrum(Harrison 1972; Zeldovich 1972; Peebles & Yu 1970). In that case all the modes entered with the same amplitude when crossing the horizon and then the primordial power spectrum is scale invariant. Scale invariant power spectrum has been ruled out by recent results from Planck satellite (Planck Results XXII 2013). The observed primordial power spectrum is almost scale invariant but not exactly scale invariant, as was originally guessed. We shall consider this primordial power spectrum taking into account only scalar fluctuations and no tilt in the power spectrum nor running index in this initial power spectrum.

2.3 Cosmological perturbations

In theoretical terms, gravitational inhomogeneities can be described by perturbations of the metric tensor. In perturbation theory using Boltzmann equations to describe the interactions between the inhomogeneities of different fluids that compound the energetic content of the Universe we can obtain theoretical estimations of the power spectrum of temperature anisotropies of CMB. This is related to inhomogeneities in the radiation component, or the power spectrum of the distribution of matter overdensities after decoupling. Large scale structure analyses from galaxy surveys are observing precisely this distribution of inhomogeneities at late times expansion of the Universe. Therefore, it is very important to analyze the evolution of cosmological perturbations from this perspective.

There are excellent reviews on linear cosmological perturbations in the literature. We refer to (Kodama & Sasaki 1984; Mukhanov, Feldman &

Brandenberger 1992; Ma & Bertschinger 1995; Malik & Wands 2009) and relevant chapters of (Peebles 1980; Liddle & Lyth 2000; Dodelson 2003; Mukhanov 2005)

Let us consider first order scalar perturbations to FLRW metric and to the energy-momentum tensor.

From Einstein's equations it is possible to derive simpler equations that describe the evolution of metric perturbations in terms of matter inhomogeneities and temperature inhomogeneities of the radiation field. But these homogeneities also vary because of the expansion of the Universe and the collision terms. Then, Boltzmann equations provide the missing conditions to completely describe the evolution of these inhomogeneities. In the simplest scenarios, it is possible to obtain analytic solutions, using different assumptions but to be more consistent we have to solve numerically all these coupled equations in order to find the spectrum of temperature inhomogeneities at recombination times, which is needed for CMB anisotropies studies or the matter inhomogeneities after matter-radiation decoupling.

The most general small perturbations $\delta g_{\mu\nu}$ of the conformally flat FLRW metric $g_{\mu\nu}$ are given by:

$$\delta g_{00} = 2a^2\phi, \tag{2.12}$$

$$\delta g_{0i} = a^2 B_i, \tag{2.13}$$

$$\delta g_{ij} = 2a^2 C_{ij}, \tag{2.14}$$

where, we implicitly assume that $|\delta g_{\mu\nu}| << |g_{\mu\nu}|$. The perturbations of the metric elements can be decomposed in

$$B_i = B_{,i} + S_i, \tag{2.15}$$

$$C_{ij} = \psi\delta_{ij} + E_{,ij} + \frac{1}{2}\left(F_{i,j} + F_{j,i}\right) + \frac{1}{2}h_{ij}, \tag{2.16}$$

where ϕ,B,ψ and E are the scalar components of the metric perturbations, whereas S_i and F_i are vector perturbations and h_{ij} is the tensor metric perturbation. From now on, for simplicity, we shall not consider vector or tensor perturbations. Thus, the perturbed metric is reduced to

$$ds^2 = a(\eta)^2\left[(1+2\phi)d\eta^2 + 2B_{,i}\,dx^i d\eta - \left((1-2\psi)\delta_{ij} - 2E_{,ij}\right)dx^i dx^j\right] \tag{2.17}$$

Let us consider also perturbations of energy-momentum tensor around the background tensor, that corresponds to a perfect fluid, of equation (2.3)

$$T^{\mu}{}_{\nu} = (\rho + p)u^{\mu}u_{\nu} - p\delta^{\mu}_{\nu} + \Sigma^{\mu}{}_{\nu}\ . \tag{2.18}$$

The different components of this tensor are given by

$$T_0{}^0 = (\bar{\rho} + \delta\rho) \tag{2.19}$$

$$T_{0i} = (\bar{\rho} + \bar{p})(v_i - B_{,i}) \tag{2.20}$$

$$T^i{}_0 = (\bar{\rho} + \bar{p})v^i \tag{2.21}$$

$$T^i{}_j = -(p + \delta p)\delta^i{}_j + \Sigma^i{}_j, \tag{2.22}$$

where we use the perturbed metric at first order to lower or raise indices and neglected higher order terms. $\Sigma^i{}_j$ is the anisotropic stress tensor, while $\bar{\rho}, \bar{p}$ are the background density and pressure, respectively, that define the perfect background fluid, which are measured in a comoving observer at rest. The anisotropic tensor is introduced by the component of the Universe with an anisotropic energy-momentum distribution. Finally, $v^i = \frac{dx^i}{d\tau}$ is the velocity of the fluid due to the perturbations.

In terms of large scale structure, we are only interested in the scalar perturbation because they are related to gravitational instabilities.

From the perturbed metric and energy-momentum tensor we can derive the Einstein first order perturbed equations in any gauge by:

$$\nabla^2\psi - 3\mathcal{H}(\psi' + \mathcal{H}\phi) = 4\pi G a^2 \delta\rho, \tag{2.23}$$

$$-\nabla_i(\psi' + \mathcal{H}\phi) = 4\pi G a^2 (\bar{\rho} + \bar{p})(v_i - B_{,i}) \tag{2.24}$$

$$\left[\psi'' + 2\mathcal{H}\psi' + \mathcal{H}\phi' + (2\mathcal{H}' + \mathcal{H}^2)\phi\right]\delta^i_j + \frac{1}{2}(\nabla^2\,\delta^i_j - \nabla^i\nabla_j)(\phi - \psi) \tag{2.25}$$

$$= 4\pi G a^2(\delta p\,\delta^i_j - \Sigma^i{}_j) \tag{2.26}$$

where $v = \sqrt{v^i v_i}$ is the total scalar velocity potential. We only have to add the evolution equations of the perturbations at first order.

We shall neglect the anisotropic stress of the energy-momentum tensor and in such a case the anisotropic component of the stress tensor vanishes and $\psi = \phi$.

a) Gauge choice

A suitable choice of coordinates in required in order to solve the perturbation equations. Depending on the gauge choice solutions they look rather different. However, the observations are based on gauge-invariant quantities.

In the longitudinal or newtonian gauge,(Bardeen 1980), the gauge-invariant quantities are ϕ and ψ. All other scalar components are zero. A different gauge is the synchronous gauge, (Lifshitz 1946). In this gauge, the gauge degrees of freedom are E and ϕ. This is used by numerical codes that solve the evolution of perturbation (Zaldarriaga & Seljak 1996; Lewis, Challinor & Lasenby 2000), because $\psi = 0$ and therefore proper time is the time of the FLRW metric.

b) Perturbed linearized Einstein Equations

The first order Einstein equations for scalar perturbations, (2.23-2.26) in the newtonian gauge and Fourier space are

$$k^2\psi = -\,4\pi G a^2 \bar{\rho}\left(\delta - 3\frac{\mathcal{H}}{k}(1+w)v\right) \tag{2.27}$$

$$k^i k_j(\phi - \psi) = +\,8\pi G a^2 \Sigma^i{}_j \tag{2.28}$$

where $\delta = \delta\rho/\bar{\rho}$ is the normalized scalar matter inhomogeneity or density constrast.

In addition to Einstein equations, which impose constrains on the scalars, we have to consider continuity and Euler equations, given by $D_\mu T^\mu{}_0 = 0$ and $D_\mu T^\mu{}_i = 0$, respectively,

$$\begin{aligned} \delta' &= -(1+w)(\theta - 3\psi') - 3\mathcal{H}\left(\frac{\delta p}{\delta\rho} - w\right)\delta, && (2.29) \\ \theta' &= -\mathcal{H}(1-3w)\theta - \frac{w'}{1+w}\theta + \frac{\delta P/\delta\rho}{1+w}k^2\delta - \frac{2}{3}k^2\frac{w}{1+w}\Sigma^i_i + k^2\phi && (2.30) \end{aligned}$$

where and $\theta = \nabla^i v_i$ is the divergence of the velocity perturbation in the newtonian gauge, i. e., the divergence of the fluid velocity, and w is given by the equation of state of the fluid, $w = p/\rho$.

i) Cold Dark Matter

Cold Dark Matter assumption implies that this fluid is pressureless, $w = 0$, and collisionless, i. e., it only interacts through gravity. Therefore, the evolution equations for CDM are

$$\begin{aligned} \delta'_c &= -\theta_c + 3\psi' && (2.31) \\ \theta'_c &= -\mathcal{H}\theta_c + k^2\phi && (2.32) \end{aligned}$$

ii) Baryonic matter

Baryons behave in a complicated way, compared with CDM evolution. First, baryons interact with the photon fluid. Moreover, this interaction is different before and after recombination. After recombination electrons interact through Compton scattering with the photons. Before recombination both fluids are tightly coupled and we have to evaluate the evolution of the coupled fluid.

After recombination, the evolution of baryon fluid is driven by continuity and Euler equations and the differences with the cold dark matter fluid are the pressure term and an additional term due to the Compton scattering of electrons and photons

$$\begin{aligned} \delta'_b &= -\theta_b + 3\psi' && (2.33) \\ \theta'_b &= -\mathcal{H}\theta_c + c_s^2 k^2\delta_b + \frac{4\bar{\rho}_\gamma}{3\bar{\rho}_b} a n_e \sigma_T(\theta_\gamma - \theta_b) + k^2\phi && (2.34) \end{aligned}$$

where $\sigma_T = 0.6652 \times 10^{-24}\mathrm{cm}^2$ is Thompson cross section, n_e the number density of electrons, μ the mean atom mass and c_s the sound speed of baryon fluid given by

$$c_s^2 = \frac{p'_b}{\rho'_b} = \frac{k_B T_b}{\mu}\left(1 - \frac{1}{3}\frac{d\ln T_b}{d\ln a}\right). \qquad (2.35)$$

On the other hand the variation of baryon temperature is given by

$$T_b' = -2\mathcal{H}T_b + \frac{8}{3}\frac{\mu}{m_e}\frac{\bar{\rho}_\gamma}{\bar{\rho}_b} a n_e \sigma_T (T_\gamma - T_b). \tag{2.36}$$

iii) Photons

The relevant properties of photons from a large scale structure perspective is how they can affect the matter spectrum. They interact in two different ways. Before recombination, photons and baryons are tightly coupled. Therefore, there are some imprints in this coupled fluid. These imprints are oscillations on the power spectrum due to the propagation of sound waves in the baryon-photon fluid. Those oscillations are called Baryonic Acoustic Oscillations (BAO). They have been detected in CMB anisotropies spectrum and also diluted in the matter power spectrum, although the significance in the latter case is not very high and one of the main goals of extragalactic redshift surveys is the detection of BAO imprint on the spectrum.

After recombination, CMB photons interact with baryons because of Thompson scattering, as shown in equation (2.34)

$$\Theta' + \vec{p}\cdot\vec{\nabla}\,\Theta + \psi' + \vec{p}\cdot\vec{\nabla}\,\phi = n_e\, a\, \sigma_T[\Theta_0 - \Theta + \vec{p}\cdot\vec{v}_b] \tag{2.37}$$

where $\vec{p}$ denotes the photon direction and Θ the perturbation of photon distribution, which can be related to the relative temperature fluctuations $\Theta = \frac{\delta T}{T}$.

2.4 Growth of structure

At the late expansion phase of the history of the Universe, in matter and dark energy dominated phases, we can use newtonian perturbation theory for (cold) non-relativistic matter at scales that are smaller than the Universe. In this period of time is when structures are formed because of the gravitational instabilities produced by the spectrum of inhomogeneities that exists after decoupling.

The growth function, $D(t)$ (Heath 1977; Peebles 1980) describes the process in which, given a potential field, overdensities grow because the attract more and more matter. For cold dark matter perturbations at sub-horizon evolution, we can neglect, in the matter-dominated phase, the anisotropic stress. Therefore, scalar perturbations in conformal newtonian gauge satisfy $\phi = \psi$ because of the constrain imposed by Einstein equations, in formula (2.26). Recalling that $d\eta = dt/a(t)$ and taking second derivatives of equation (2.31), including equations (2.32) and (2.27) and neglecting derivative on ϕ for sub-horizon evolution we obtain a linearized second order differential equation

$$\frac{\partial^2\delta}{\partial t^2} + 2H\frac{\partial\delta}{dt} = 4\pi G\bar{\rho}\delta. \tag{2.38}$$

The solution of this second-order differential equation can be written in the following form

$$\delta(k,t) = D_1(t)A(k) + D_2(t)B(k) \tag{2.39}$$

where D_1 is the growing mode that describes the growth of structure ($\dot{D}_1 > 0$) while D_2 is the decaying mode that suppresses initial inhomogeneities ($\dot{D}_2 < 0$) and initial conditions are given by $A(k)$ and $B(k)$. We shall only consider the growing mode and in this work we use the notation $D(t) = D_1(t)$ where $D(t)$ is called growth function.

In a ΛCDM universe, the growth factor is obtained the hypergeometric function:

$$D(a) = \frac{5\Omega_m(a)H(a)}{2}\int_0^a \frac{da'}{a'^3H(a')} \tag{2.40}$$

where we normalize it in order to follow the same convention than we use for the scale factor, and therefore $D(1) = 1$. In a universe with only cold dark matter, the growth factor is proportional to the scale factor a.

Usually, the linear growth rate:

$$f(a) = \frac{d\ln D}{d\ln a} \tag{2.41}$$

is commonly used in the literature. It has been shown that for the standard scenario in which gravity is described by General Relativity the linear growth factor can be parametrized as (Lahav et al. 1991; Wang & Steindhardt 1998; Linder 2005)

$$f(z) = \Omega(z)^\gamma \tag{2.42}$$

where γ is the growth index and for the standard GR case $\gamma = 0.554$ (Peebles 1980; Linder 2005). This parameter depends on the dark energy model and in the gravity. Therefore, determining this parameter is a perfect tool to distinguish between dark energy and modify gravity models, given a background expansion history.

Finally, we can show the expression for the growth factor in terms of redshift, which is the coordinate that we will observe when measuring the spectral emission of galaxies with galaxy surveys:

$$D(z) = exp\left(-\int_0^z \frac{dz f(z)}{(1+z)}\right) \tag{2.43}$$

Another observable of interest is the matter peculiar velocity.

Peculiar velocity of matter

The matter peculiar velocity is given by the velocity of the perturbations. From equation (2.31) we get

$$v(k,\eta) = \frac{i\delta(k,\eta)}{k} = \frac{i\delta(k,\eta)}{k}\frac{d\ln D}{d\ln\eta} = \frac{ifaH\delta(k,\eta)}{k} \tag{2.44}$$

the peculiar velocity of the matter perturbation field.

2.5 Transfer function

The transfer function describes the behaviour of perturbations between horizon crossing and radiation-matter equality. Therefore these transfer functions are unity for the modes that correspond to scales greater than the horizon at radiation/matter transition. Let us define this mode as k_{eq}. The initial conditions that we consider for the growth factor are given by the initial conditions at the horizon crossing times the transfer function, i.e. The transfer function output are the initial conditions of equation (2.39) Transfer functions are given by the coupled Einstein perturbed equations and the evolution of the perturbations of the different components of the Energy-Momentum tensor. There are some analytic solutions, (Bardeen et al. 1986; Eisenstein & Hu 1998) but in general, if we need the exact solution we have to solve numerically this system of differential equations (usually numerical codes also compute the power spectrum), (Zaldarriaga & Seljak 1996; Lewis, Challinor & Lasenby 2000).

Transfer function is defined as:

$$T(k) = \frac{\delta(k)}{\delta(k_{eq})} \tag{2.45}$$

2.6 Matter power spectrum

Finally, after solving the evolution of the modes related to small scales after the horizon crossing in the radiation and matter-dominated stages, which as we have seen above is given by the *transfer function* and the *growth factor* we can define the linear matter power spectrum of inhomogeneities as:

$$P(k,z) = \langle |\delta_k^2| \rangle = D(z)^2 T^2(k) P_0(k) \tag{2.46}$$

Recall that this matter power spectrum is gauge dependent (Yoo, Fitzpatrick & Zaldarriaga 2009; Yoo 2010; Challinor & Lewis 2011). Actually, this is not a real observed quantity, as we know that observed quantities must be gauge independent, but it has been often used as a pseudo-observable. In current and past surveys this problem was not important because the gauge dependency is only detectable at the largest scales, above the equality turnover, k_{eq}.

If the primordial fluctuations followed a gaussian distribution, this power spectrum encodes all the cosmological information, in the linear regime.

The normalization of the power spectrum is related to the variance in a sphere of radius R of the power spetrum,

$$\sigma^2(R) = \int \frac{dk k^2}{2\pi^2} P(k) W^2(kr) \tag{2.47}$$

where $W(kr)$ is a spherical window in Fourier space,

$$W(kr) = \frac{3(\sin kr - kr\cos kr)}{(kr)^3} \tag{2.48}$$

and $P(k)$ is the linear matter power spectrum at redshift $z = 0$. This normalizations measure the amplitude of clustering at scale R. Usually, $R = 8\mathrm{h}^{-1}\mathrm{Mpc}$ and we define the parameter $\sigma_8 = \sigma(R = 8\mathrm{h}^{-1}\mathrm{Mpc})$

2.7 Galaxy clustering

We have shown that, besides geometrical measurements of the rate of expansion, cosmological information is encoded in the distribution of the inhomogeneities because they trace the primordial spectrum of cosmological perturbations and their evolution throughout the different phases of the Universe expansion. Mainly, the angular correlation of CMB temperature fluctuations show the imprint of the matter distribution at the time of recombinations on the energy distribution of photons at that redshift, $z = 1100$. Note that there are other secondary effects on CMB temperature anisotropies due to the interaction with the photons with the matter distribution in the Universe after recombination that changed the pattern of the anisotropies like Doppler effect and Sachs and Wolfe effect. At these distance, the linear model stands up to minimum scales of 0.2 angular degrees and therefore it is easier to test the model presented in previous chapter.

But the main disadvantage of CMB is that its information is constrained in the surface corresponding to a sphere with radius given by the comoving distance to redshift $z = 1100$. This induces degeneracies between cosmological parameters because the distance to this sphere and the distances in the surface of this sphere depend on the same parameters. If we can study the spectrum of inhomogeneities at different moments of the expansion using different probes it would improve the constrains on the model parameters.

In addition to that, the decoupling between baryons and photons happened in a matter-dominated Universe. The effect of dark energy then was small, although CMB radiation is affected by a late ISW effect in which dark energy plays an important role citar. Cosmological probes at late time expansion, such as the clustering of galaxies, in addition to CMB, would provide better constrains in dark energy equation of state w.

Historically, the most used technique to analyze large scale structure in galaxy surveys uses correlation functions, either in angular or three dimensional space.

Galaxy clustering studies measuring the full shape of the correlation of galaxies are similar to CMB studies of anisotropies. Either 3D correlations or angular correlations are fitted using the framework provided in this chapter and cosmological parameters are constrained. This should be done in combination with other probes like CMB or type Ia Supernovae because clustering can poorly fit the parameters of the initial power spectrum. But on the other hand, galaxy clustering is a powerful tool to understand Dark Energy because the galaxy maps traced by surveys live in the dark energy realm and the acceleration of the expansion is imprinted in clustering of galaxies, which is especially sensitive in Ω_m. The higher Ω_m, the higher the clustering and therefore, the clustering.

As we have seen in this chapter, theoretical cosmological information is contained in the power spectrum $P(k, z)$. Then, in order to relate this with the galaxy catalogue produced by a survey, we need to match it with the power spectrum of galaxies. One caveat is that this is not really the observable because galaxy coordinates in catalogues are the two angles that define the direction on the sky pointing to the galaxy and the redshift of each galaxy while the power spectrum lies in Fourier space. But for a given cosmological parameters, we can turn angles and redshift into cartesian comoving coordinates and then Fourier transform in order to build the power spectrum.

On the other hand, we have to take into account that we are assuming that galaxies are tracing the matter field of inhomogeneities. But galaxies are more clustered than matter and therefore we have to include the linear *galaxy bias*, b_g, (Kaiser 1984; Bardeen et al. 1986). The galaxy bias relates the local matter inhomogeneity, (Fry & Gaztañaga 1993) with the galaxy number density:

$$\delta_g(k, z) = b_g(k, z)\delta(k, z). \tag{2.49}$$

In this case, the galaxy power spectrum in real space would be given by

$$P_g(k, z) = b_g^2(k, z)P(k, z) \tag{2.50}$$

Different populations of galaxies have different bias. For example, Luminous Red Galaxies (LRG) are highly biased because they are brighter objects, living in the more massive halos. On the other hand, star-forming galaxies are nearly unbiased.

2.7.1 Redshift-space distortions (RSD)

Galaxies are tracers of the matter density contrast field but galaxies are observed in redshift space. In expression (2.49) we have assumed that each redshift corresponds to a comoving distance given by the general expansion flow of the Universe. Galaxies in clusters are falling to the densiest regions of its host cluster or local inhomogeneity peak. Then, the galaxy power spectrum should be corrected by this peculiar motion to turn into the galaxy power spectrum in redshift space. The relation between position of the galaxy in redshift space and real position is

$$\vec{s} = \vec{r} + \vec{v}_p \tag{2.51}$$

The displacements along the line of sight caused by this peculiar velocities are *redshift-space distortions* (RSD). Spherical overdensities appear squashed at linear scales in the radial direction while at non-linear scales we see filaments on the line of sight, the Fingers of God. This, a priori a systematic has turned on a cosmological probe because in the linear regime, redshift space distortions are due to the coherent infall of galaxies in the centre of the overdensity. The linear power spectrum of galaxies on linear scales was first derived by Kaiser, (Kaiser 1987). Here, we follow the derivation of the power spectrum in redshift space given in (Hamilton 1998). Conservation of galaxies gives

$$n^s(s)d^3s = n(\vec{r})d^3r \tag{2.52}$$

where s means redshift space. This can be expanded in terms of density contrasts

$$\bar{n}\left(1+\delta^s(\vec{s})\right)s^2ds = \bar{n}(\vec{r})\left(1+\delta(\vec{r})\right)r^2dr \tag{2.53}$$

From Eq. 2.51

$$1+\delta^s(\vec{s}) = \frac{r^2\bar{n}(\vec{r})}{(r+v_p)^2\bar{n}(\vec{r}+\vec{v_p})}\left(1+\frac{\partial v}{\partial r}\right)^{-1}(1+\delta(\vec{r})) \tag{2.54}$$

and at linear order,

$$\delta^s(\vec{r}) = \delta(\vec{r}) - \left(\frac{\partial v}{\partial r}+\frac{\partial \ln r^2\bar{n}(\vec{r})}{\partial \ln r}\frac{v}{r}\right). \tag{2.55}$$

Neglecting the second term in the parenthesis for scales covered by a survey, and using

$$\vec{v}(\vec{k}) = ifH\delta(\vec{k})\frac{\vec{k}}{k^2} \tag{2.56}$$

which is the vectorial expression of equation 2.44, then

$$\delta^s = \left(1+f\frac{k_{\parallel}^2}{k^2}\right)\delta = (1+f\mu^2)\delta \tag{2.57}$$

where μ is the cosine between the $\vec{k}$ and the line of sight.

Finally, assuming that velocities are not biased, the final expression for the power spectrum of galaxies in redshift space is:

$$P(k,z) = (b_g(k,z)+f(z)\mu^2)^2D(z)^2P(k,z=0) \tag{2.58}$$

In eq. (2.58) we see that using redshift-space distortions we can test the growth history of the Universe comparing the amplitude on the clustering of transverse modes (not affected by RSD) and the amplitude of clustering of parallel modes. Using this probe we can estimate $b\sigma_8$ and $f\sigma_8$.

Therefore, this probe in combination with independent measurements of bias and with weak lensing would improve the constraints on the those parameters. Weak lensing is the distortion on the background galaxy shapes and brightness by the foreground matter distribution. As all the matter lenses the light, the correlations of distortions on background galaxies does not depend on the bias but on σ_8^2. If we cross-correlate this distortions with the foreground galaxies we are measuring $b\sigma_8^2$. Combining RSD with this probes will break those degeneracies, improving the figures of merit of surveys, (Gaztañaga et al. 2012; Cai & Bernstein 2012). Therefore, we will be able to test GR and dark energy models (Reyes et al. 2010)

Thanks to RSD, we can discriminate between dark energy models and modify gravity because they predict different values for the linear growth rate $f(z)$.

2.8 Galaxy surveys: DES and PAU

Let us describe briefly the two surveys we have been involved within the cosmology group at the Institut de Ciènces de l'Espai. They are the photometric surveys, the Dark Energy Survey (DES) and the Physics of the Accelerating Universe Survey (PAU)

2.8.1 Dark Energy Survey (DES)

The Dark Energy Survey (Annis et al. 2005), `www.darkenergysurvey.org`, is a broad-band photometric survey planned to understand the nature of dark energy using type Ia Supernovae, Baryon Acoustic Oscillations, Weak Lensing and Galaxy cluster number counts probes of acceleration of the Universe. The Dark Energy Camera (DECam), (dePoy et al. 2008) is a 570 Megapixel camera, containing 74 CCDs, and it is located on the 4-m diameter Blanco Telescope, at Cerro Tololo, in Chile. The field of view is around 2.2 deg. Using a grizY filtering system, it will cover 5000 deg^2 during 525 nights in 5 years. It will record over 300 million galaxies reaching magnitude $i_{AB} < 24.5$. Operations began in September, 2012 and the survey is expected to start in the fall of 2013.

2.8.2 Physics of the Accelerating Universe (PAU)

The Physics of the Accelerating Universe Survey (Benitez et al. 2009), `www.pausurvey.org`, is a narrow-band photometric survey that will study the properties of dark energy combining redshift space distortions probe and weak lensing magnification using galaxy cross-correlations.

The PAUCam, (Casas et al. 2010), is designed to obtain accurate photometric redshifts, using a system of 40 filters and 5 broad-band ugriz filters. The magnitude depth of for the narrow-band filters is $i_{AB} < 25.7$ with a photometric accuracy of $\sigma_z/(1+z) = 0.0035$ which is about $10\,h^{-1}\,\mathrm{Mpc}$, translated to comoving coordinates. For the broad-band filters, the maginitude depth is $i_{AB} < 24$ with $\sigma_z/(1+z) = 0.05$. The camera will be a community instrument at the 4-m diameter WIlliam Herschel Telescope, at La Palma, Spain and it is expected to begin operations by the end of 2013. The camera would be able to cover 2 deg^2 per night. The expected area of the survey is 100/200 deg^2, recording 2 000 000 photometric spectra from the narrow filters and 10 000 000 galaxies with the broad-band filters.

Chapter 3

Recovering 3D clustering information with angular correlations

3.1 Motivation

The motivation for the study explained in this chapter is en-marked in the evaluation of the different approaches that we can consider when using extragalactic surveys to extract information on cosmological parameters. The final outcome of a extragalactic survey is a galaxy map with the positions of the galaxies in angular/redshift space. A priori, this is the proper coordinate system to evaluate the distribution of galaxies because we are not introducing any biased estimator of this distribution. But, as we have seen in chapter 2, cosmological information description is in cartesian space and in this sense, it would be easier to study the three-dimensional distribution of galaxies in cartesian space (3D). This would not produce any distortion in the analysis if conversion from redshift to distances were not parameter dependent. Therefore, if we want to evaluate directly the power spectrum of galaxies in Fourier space, or the 3D correlations function in configuration space, we have to assume a value for the cosmological parameters.

On the other hand, we can measure the angular correlation of galaxies (2D). But in this case we are loosing the radial information when we project the galaxies in the sphere. If we divide the catalogue in different radial shells and then the observables are composed by the angular correlations in redshift bins we are sampling more transverse modes, where transverse mean perpendicular to the line of sight, improving the performance. Finally we can carry out a full tomographic analysis including all the cross-correlations between redshift bins. This allows us to include radial modes given by the bin separation, in an analogy with 3D modes.

Another advantage of using angular correlations is that, usually, the correlations of weak lensing distortions are made in 2D, including weal lensing tomography. Therefore, the combination of clustering and weak lensing studies as proposed in (Gaztañaga et al. 2012; Cai & Bernstein 2012) would be easier in the 2D framework. Let us mention that there are 3D weak lensing analysis (Heavens 2003; Castro, Heavens & Kitching 2005; Kitching et al. 2011)

There have been works analyzing the nature of this 2D approach, (Bonvin C., Durrer R. 2011; Challinor & Lewis 2011; Montanari & Durrer 2012), including all the possible corrections due to GR effects, velocity and lensing terms. But we are interesting in the capacity of the tomographic 2D approach to challenge the constrains on parameters given by the most standard 3D approach. And therefore how to optimize the tomographic redshift bins in order to be as precise as when using the 3D power spectrum. We have provided forecast on different types of surveys in order to find the relation that will allow us to use the optimal bins in future galaxy surveys.

In this analysis, first of all, we have compared the constrains on Ω_m obtained from the 2D and 3D methods in a full sky spectroscopic survey. This comparison is performed for different redshift bin configurations. In the comparison we have to take into account that in the 3D analysis we usually cut at a minimum scale because we are assuming the linear model and at small scales the power spectrum in reality is non-linear because it is the range in which gravity has produced collapsed bodies and this kind of processes are non-linear. Therefore, we also the cut the 2D spectra at a minimum angular scale related to the 3D minimum scale in order to do a fair comparison.

Then, for the same spectroscopic survey, we compare the RSD constrains in a bias free case. This case is relevant because RSD affect the radial positions of the galaxies and therefore.

Finally, we forecast constrains on Ω_m for full sky narrow and broad-band photometric surveys.

3.2 Methodology

3.2.1 Fiducial surveys

Let us describe the fiducial surveys and the galaxy samples that we are considering in the comparison. They are characterized by the redshift range, the area of sky covered, the accuracy of the redshift measurements and the galaxy bias of the galaxy sample.

For the comparison made in this chapter, we considered full sky surveys, where the fraction of sky is the unity, $f_{sky} = 1$. In that case, the different ℓ modes of the angular power spectrum C_ℓ are independent. This simplifies the covariance matrix of the C_ℓ because it is diagonal with respect to ℓ.

Number of bins	Δz	Δr (h^{-1} Mpc)
1	0.20	468
4	0.05	113 - 122
8	0.025	56 - 61
16	0.0125	28 - 31
20	0.010	22 - 25

Table 3.1: Bin configurations used for the 2D tomography in the case of the spectroscopic and the narrow band photometric survey in a redshift range of $0.45 < z < 0.65$. We show the number of radial bins and their range of widths in redshift and comoving distance.

$$\frac{dN}{dzd\Omega} = N_{gal}\left(\frac{z}{0.55}\right)^2 e^{-\left(\frac{z}{0.55}\right)^{1.5}} \tag{3.1}$$

which is typical of a flux-limited sample with a magnitude cut at $i_{AB} < 24$. In Eq. (3.1) N_{gal} is a normalization related to the total number of galaxies per square degree under consideration.

Spectroscopic survey

For this survey we consider a redshift range $0.45 < z < 0.65$, which is similar to SDSS photometric sample, (Padmanabhan et al. 2005; Padmanabhan et al. 2007; Blake et al. 2007). For the spectroscopic sample of galaxies, we assumed that galaxy bias is constant because the total redshift range does not cover a large depth. The galaxy bias is $b_g = 2$, similar to highly biased populations like Luminous Red Galaxies (LRG) samples. The redshift bin configuration applied to the sample is especially relevant in the 2D tomography because the radial resolution is sensitive to the number of bins. We show in table 3.1 the different configurations used in the analysis. The table indicates the number of redshift bins in which we dice the redshift range mentioned above. In a spectroscopic survey, the redshift of each galaxy is the true redshift. The implications of this is that each bin is a top hat bin in the space of true redshifts[1] . In the notation we used here, this means that $\sigma_z = 0$, where σ_z is the dispersion on the redshift measurements.

We selected all the redshift bins with the same width in redshift space and therefore $\Delta_z = (z_{MaxSurvey} - z_{Min_Survey})/N_z$. This assumption is the same throughout this chapter, as explained below in section 3.2.1. In the third column of table 3.1 we show how the bin width in redshift space translates

---

[1] To satisfy differentiability requirements at the edges we use in practice $\phi(z) \propto \exp\left[-((z-\bar{z})/(\Delta z/2))^{20}\right]$, where $\bar{z}$ is the mean redshift of the bin and Δz the full width.

Case	$n(r)$ $(h^3\,\mathrm{Mpc}^{-3})$
Low Shot-Noise	$3.14 \cdot 10^{-3}$
High Shot-Noise	$6.89 \cdot 10^{-4}$

Table 3.2: Comoving galaxy number densities at $z = 0.55$ for the spectroscopic and narrow-band photometric surveys. Case 1 corresponds to a low shot noise level ($nP_{gal} \sim 2\%$, where P_{gal} is the monopole of the galaxy spectrum at $z = 0.55$ and $k = 0.1\,h\,\mathrm{Mpc}^{-1}$) while Case 2 corresponds to a high shot noise level ($nP_{gal} = 10\%$) .

to comoving distances, showing the range of comoving widths of the radial shells.

Regarding the galaxy number density of the spectroscopic sample, we have selected two different samples. Their number densities are shown in table 3.2

For the considered redshift range, the low shot-noise case, with higher number density, consists on a sample of 40 million galaxies while the the case with lower density consists on a sample with 9 million galaxies. Comparing the constrains on the parameters for the different cases allow us to study the effect of shot noise in the results.

Narrow band photometric survey

In the next years, there would be a generation of photometric surveys that, instead of using a small set of broad band filters as usually this kind of surveys are developed, will cover the sky using cameras with more than 40 narrow-band multi-filters. Surveys such as Physics of the Accelerating Universe Survey (PAU) (Benitez et al. 2009; Casas et al. 2010; Gaztañaga et al. 2012) or J-PAS (Taylor et al. 2013). Measuring the photometric redshift in those surveys will increase the precision of redshifts while the number density is as high as in a photometric survey.

Therefore, we would like to compare the performance of this surveys compared with the spectroscopic case explained above. We consider a narrow-band photometric survey, with $\sigma_z = 0.004$, with the same redshift range than in the spectroscopic case, i. e., $0.45 < z < 0.65$. As in the spectroscopic sample, the narrow-band photometric sample is highly biased, $b_g = 2$, assuming it is constant in the redshift range considered. Samples have the same number of galaxies than in the spectroscopic survey and number densities are listed in table 3.2. We use the bin configurations shown in table 3.1. In summary, we only change the accuracy of redshifts with respect to the spectroscopic survey. We assume that this accuracy is the same in all the redshift bins. This implies that we select bins with the same width. In

Number of bins	Δz	Δr (h^{-1} Mpc)
4	0.25	398 - 592
5	0.20	315 - 480
6	0.167	260 - 404
7	0.143	221 - 348
8	0.125	193 - 306
9	0.111	171 - 273
10	0.10	153 - 246

Table 3.3: Bin configurations considered for a broadband photometric survey within a redshift range $0.4 < z < 1.4$. We show the number of radial bins and their range of widths in redshift and comoving distance.

top panel of figure 3.1 we show the redshift bins used for this samples.

Broad band photometric survey

Finally, we consider a broad-band photometric survey like Dark Energy Survey, Pan-Starrs, LSST and the imaging component of EUCLID. In this case, we chose a deeper redshift survey with range $0.4 < z < 1.4$. In this case we assume a linear evolution with redshift for the bias, following (Fry 1996),

$$b(z) = 1 + (b_\star - 1)\frac{D(z_\star)}{D(z)} \tag{3.2}$$

where $b_\star = 2$ is bias at redshift $z_\star = 1$. For the bias evolution we assume the fiducial cosmology always. The photometric error is conservative, $\sigma_z = 0.1$. We do not consider evolution on this error and we select bins with constant width. As we have modify the redshift range, then the bin configurations for the broad-band survey is different. Broad-band survey bin configurations are shown in table 3.3.

The number of galaxies considered is of the order of $150 \cdot 10^6$. This number satisfies the number density of the low shot noise case of table 3.2.

3.2.2 Spatial (3D) power spectrum

The three-dimensional quantity that we use to forecast constrains on the parameters is the galaxy power spectrum in redshift space in quasi-linear scales.

$$P_g(k, \mu, z) = (b_g + f\mu^2)^2\, D^2(z)\, P(k) e^{-k^2\sigma_t^2(z)\mu^2}, \tag{3.3}$$

where $P(k)$ is the linear spectrum at $z = 0$ (properly normalized), $D(z)$ is the linear growth factor and the remaining amplitude depends on the bias $b(z)$ and the linear growth rate $f(z) \equiv d\ln D/d\ln a$. We compute P(k) using

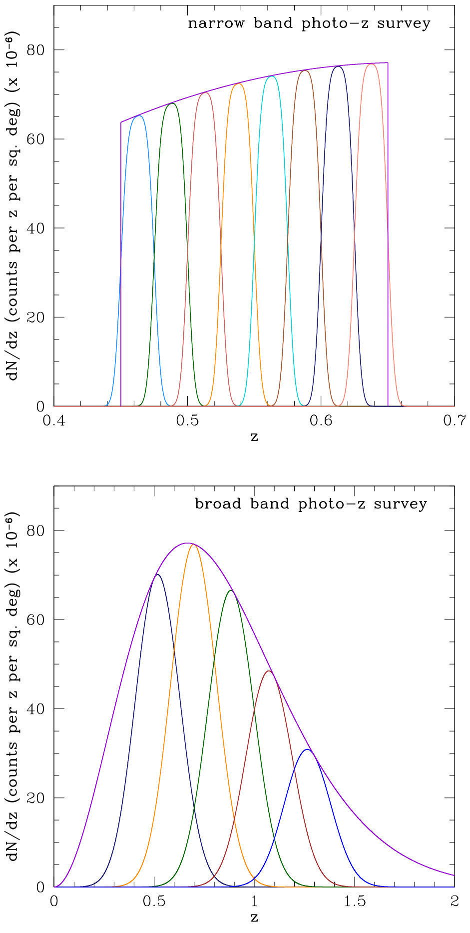

Figure 3.1: Top panel shows the redshift distribution in the spectroscopic and narrow band photo-z survey (violet). For the narrow band case we show how the true redshift distributions given by Eq. (3.1) look like if we divide the volume in eight consecutive redshift bins. Bottom panel shows the same but for a broadband photometric survey divided in five bins.

`CAMB` The Gaussian cut-off accounts for the fact that the radial information might be diluted due to photometric redshift errors σ_z. This expression is correct as long as the distribution of photometric errors is Gaussian, as we assume here. In Eq. (3.3) this redshift error propagates to scales through $\sigma_t(z) = c\,\sigma_z/H(z)$. Notice that σ_t depends also on the cosmic history. This should be taken into account when constraining relevant cosmological parameters (e.g. Ω_m).

Ideally, when we compare measurements with a theoretical power spectrum we have to perform a new measurement for each set of cosmological parameters that we are considering in the comparison. This is time expensive because we would have to recompute all the cartesian comoving coordinates and the Fourier transforms.

Then, to improve the performance of the analysis, we can choose a reference cosmological model, where we have chosen to perform the measurement of the power spectrum, and transform each model prediction frame to the reference frame when doing the comparison between the model and the measurements. This is the Alcock-Paczynski effect (Alcock C., Paczynski B. 1979).

Let us call $P^{obs}(k,\mu)$ the power spectrum measured in the *reference* cosmology and $P^{mod}(\widetilde{k},\widetilde{\mu})$ the model prediction at the point in cosmological parameter space being tested. The transformation of distances and angles from the cosmological model being tested $(\widetilde{k},\widetilde{\mu})$ to those in the reference model (k,μ) is done through the scaling factors

$$c_\parallel = \frac{H(z)}{H^{mod}(z)} \quad ; \quad c_\perp = \frac{d_A^{mod}(z)}{d_A(z)}, \tag{3.4}$$

as $\widetilde{k}_\parallel = k_\parallel/c_\parallel$ and $\widetilde{k}_\perp = k_\perp/c_\perp$, where $\parallel$ indicates modes parallel to line of sight and $\perp$ perpendicular. The Hubble parameter and the angular diameter distances are given by

$$\begin{aligned} H(z) &= 100h\sqrt{\Omega_m(1+z)^3 + \Omega_{DE}(1+z)^{-3(1+w)}} && (3.5) \\ d_A(z) &= \frac{\int_0^z \frac{dz'}{H(z')}}{1+z}. && (3.6) \end{aligned}$$

From the above one trivially finds,

$$\begin{aligned} \widetilde{k} &= k\,\sqrt{(1-\mu^2)c_\perp^{-2} + \mu^2 c_\parallel^{-2}} && (3.7) \\ \widetilde{\mu} &= \mu\, c_\parallel^{-1}/\sqrt{(1-\mu^2)c_\perp^{-2} + \mu^2 c_\parallel^{-2}}. && (3.8) \end{aligned}$$

In addition, the power spectrum is sensitive to the volume element. Thus we must re-scale P^{mod} by the differential volume element with respect to the reference cosmology : $c_\perp^2 c_\parallel$. For a similar approach, see (Hawken et al. 2012)

Lastly, following (Tegmark 1997) and (Seo et al. 2003) we construct the χ^2 for each radial bin i as,

$$\begin{aligned}\chi^2_{3D}(i) = &\int_{k_{min}}^{k_{max}} \frac{dk k^2}{8\pi^2} \int_{-1}^{1} d\mu \, \mathrm{Cov}^{-1}_{\mathrm{eff}}(k,\mu) \Big(P_g^{obs}(k,\mu,z_i) \\ &- \frac{1}{c_{\|} c_{\perp}^2} P_g^{mod}\left(\widetilde{k}, \widetilde{\mu}, z_i\right)\Big)^2 \end{aligned} \tag{3.9}$$

where $\mathrm{Cov}^{-1}_{\mathrm{eff}}$ is defined for every bin i according to,

$$\mathrm{Cov}^{-1}_{\mathrm{eff}}(k,\mu) = \int_{r_{min}(i)}^{r_{max}(i)} d^3r \left(\frac{\bar{n}(r)}{1+\bar{n}(r) P_g^{obs}(k,\mu,\bar{z}_i)} \right)^2 . \tag{3.10}$$

$$\chi^2_{3D} = \sum_i \chi^2_{3D}(i), \tag{3.11}$$

3.2.3 Angular (2D) power spectrum

The alternative approach to the 3D power spectrum consists on perform the analysis in the coordinates of the survey catalogues, i. e., using the redshift and angular position of galaxies. We divide the depth of the survey in a number N_z of radial shells. for the galaxies sample considered, we measure the angular power spectrum of the angular distribution of galaxies of each bin. Those are the auto-correlations.

The main problem of angular auto-correlations is that we are projecting all the radial information in the redshift bin because we are assuming that all the galaxies that satisfy the selection function criteria are in the same radial shell. This is a disadvantage compared with the spatial power spectrum because in the latter we include all the modes inside the survey volume. If we want to improve the level of radial information using angular correlations we have to include the cross-correlations between different redshift bins. A cross-correlation includes the information of scales given by separation between the two redshift bins. This is a tomographic analysis of the galaxy maps provided by surveys.

For this case, the analysis is done using the scape of spherical harmonics, in an isotropic Universe. The matter fluctuations, projected in the radial direction, angular field can be decompose in the spherical harmonic basis, (Peebles 1973)

$$\delta(\hat{\mathbf{n}}) = \sum_{\ell \geq 0} \sum_{m=-\ell}^{\ell} a_{\ell m} Y_{\ell m}(\hat{\mathbf{n}}), \tag{3.12}$$

where $\hat{\mathbf{n}}$ is the angular position in the sky and $Y_{\ell m}(\hat{\mathbf{n}})$ the spherical harmonics. The angular power spectrum is defined by the coefficients of the previous expansion, $a_{\ell m}$

$$\langle a_{\ell m} a_{\ell' m'} \rangle \equiv \delta_{\ell\ell'} \delta_{mm'} C_\ell \tag{3.13}$$

In the full sky, the $a_{\ell m}$ are gaussianly distributed and we can estimate each ℓ power adding to the $2\ell+1$ modes of each ℓ

$$\widetilde{C}_\ell \equiv \frac{1}{2\ell+1} \sum_{m=-\ell}^{\ell} a^2_{\ell m} \tag{3.14}$$

We have chosen to perform the spherical analysis using the C_ℓ, instead of working in configuration space because in theoretical terms the analysis is simpler in the case exposed here. The C_ℓ are related with $P(k)$ throughout the Fourier expansion of $\delta(\hat{\mathbf{n}})$. Using the expansion of the plane wave into spherical harmonics,

$$e^{ikr\hat{\mathbf{k}}\cdot\hat{\mathbf{n}}} = 4\pi \sum_{\ell\geq 0} \sum_{m=-\ell}^{\ell} i^\ell j_\ell(kr) Y_{\ell m}(\hat{\mathbf{k}}) Y^\star_{\ell m}(\hat{\mathbf{n}}) \tag{3.15}$$

, then, the this leads to

$$a_{\ell m} = 4\pi i^\ell \int dz\, \phi(z) \int \frac{d^3k}{(2\pi)^3} \delta(\mathbf{k}, z) j_\ell(k\, r(z)) Y^\star_{\ell m}(\hat{\mathbf{k}}), \tag{3.16}$$

Using the orthogonality of spherical harmonics, the exact computation of the angular power spectrum of projected overdensities in a radial shell i is.

$$C_\ell^{ii} = \frac{2}{\pi} \int dk\, k^2 P(k) \left(\Psi^i_l(k) + \Psi^{i,r}_l(k) \right)^2 \tag{3.17}$$

where

$$\Psi^i_\ell(k) = \int dz\, \phi_i(z) b(z) D(z) j_\ell(kr(z)) \tag{3.18}$$

is the kernel function in real space. When working in redshift space, we may add

$$\begin{aligned} \Psi^{i,r}_\ell(k) &= \int dz\, \phi_i(z) f(z) D(z) \left[\frac{2l^2+2l-1}{(2\ell+3)(2\ell-1)} j_\ell(kr) \right. \\ &- \frac{\ell(\ell-1)}{(2\ell-1)(2\ell+1)} j_{\ell-2}(kr) \\ &- \left. \frac{(\ell+1)(\ell+2)}{(2\ell+1)(2\ell+3)} j_{\ell+2}(kr) \right]. \end{aligned} \tag{3.19}$$

to Ψ^i_ℓ if we include the linear Kaiser effect (Padmanabhan et al. 2007). In turn, photo-z effects are included through the radial selection function $\phi(z)$, see below. This model then has the same assumptions as the 3D spectrum from Eq. (3.3).

It is easy to extend this result to the cross-correlations of different redshift bins. These are given by

$$C_\ell^{ij} = \frac{2}{\pi} \int dk\, k^2 P(k) \left(\Psi_\ell^i(k) + \Psi_\ell^{i,r}(k) \right) \left(\Psi_\ell^j(k) + \Psi_\ell^{j,r}(k) \right) \tag{3.20}$$

Cross-correlations given by Eq. (4.5) are symmetric,

$$C_\ell^{ij} = C_\ell^{ji}, \tag{3.21}$$

and hence we only use for the analysis the non-redundant terms.

Notice that in Eq. (3.17,4.5) we are only considering density and redshift space distortions terms. We are neglecting General Relativity (GR) effects as well as velocity and lensing terms, which are in our cases subdominant to the ones considered. Nonetheless the framework of angular auto and cross-correlations could easily include these effects when required (Bonvin C., Durrer R. 2011; Challinor & Lewis 2011; di Dio et al. 2013).

We use the public code `CAMB_sources` to perform the computation of the theoretical angular power spectra. Detailed information about the performance of the code can be found in (Challinor & Lewis 2011) and the code can be requested to the authors in **camb.info/sources**. We have modify the original code in order to include the radial selection functions considered in 3.2.3. We have only considered the newtonian gauge density term and the redshift space distortions term when running the code, as mentioned below. We use the exact calculation of C_ℓ rather than the well-known Limber approximation, (Limber 1954; Simon 2007; LoVerde & Afshordi 2008) because the latter approximation does not include the cross-correlation terms, which are precisely really important in our approach.

There is one angular power spectrum per radial shell, hence, there are N_z auto-correlations. But if we want to study all the clustering information we should add to our observables the $N_z(N_z - 1)/2$ cross-correlations between different redshift bins. Therefore, then number of observable power spectra that we consider in the tomographic analysis of galaxy distribution is $N_z(N_z + 1)/2$ This is the number of observables we have to use when reconstructing clustering information from tomography using N_z bins.

Radial selection functions

The information about the redshift bin in which we are projecting the three-dimensional maps of galaxies is included in the radial selection functions ϕ_i in Eqs. (3.17,4.5). Formally, they weight the probability to include a galaxy in the considered redshift bin. Hence, they are the product of the galaxy redshift distribution and a window function that depends on selection criteria (e.g binning strategy),

$$\phi_i(z) = \frac{dN_g}{dz} W(z) \tag{3.22}$$

where dN_g/dz is the redshift distribution of galaxies, given by Eq. (3.1). All the integrals are performed in the true redshift space. Therefore, depending on the redshift estimation used in the survey, $W(z)$ may change. Here, we consider two different types. For the spectroscopic redshift survey $W(z)$ is a top hat function with the dimensions of the redshift bin.

On the other hand, if galaxies belong to the catalogue of a photometric survey we select them from the catalogue using top hat functions in the space of photometric redshifts. We include the effect of photo-z in order to convert the those top hat bins in photometric space, $W_i(z_p)$ in the corresponding bins in the space of true redshifts,

$$W_i(z) = \int dz_p P(z|z_p) W_i(z_p), \tag{3.23}$$

where z_p is the photometric redshift and $P(z|z_p)$ is the probability of the true redshift to be z if the photometric estimate is z_p.

In addition to the assumption of a top-hat selection $W(z_p)$ in photometric redshift we consider that $P(z|z_p)$ is gaussian with standard deviation σ_z. This leads to,

$$\phi_i(z) \propto \frac{dN_g}{dz}\left(\mathrm{erf}\left[\frac{z_{p,max}-z}{\sqrt{2}\sigma_z}\right] - \mathrm{erf}\left[\frac{z_{p,min}-z}{\sqrt{2}\sigma_z}\right]\right) \tag{3.24}$$

where $z_{p,min}$ and $z_{p,max}$ are the (photometric) limits of each redshift bin considered. In the equation above and throughout this chapter we assume σ_z is constant in redshift.

Covariance matrix of angular power spectra

The covariance between angular spectra of redshift bins ij and redshift bins pq is given by

$$\mathrm{Cov}_{\ell,(ij)(pq)} = \frac{C_\ell^{obs,ip} C_\ell^{obs,jq} + C_\ell^{obs,iq} C_\ell^{obs,jp}}{N(l)} \tag{3.25}$$

where $N(\ell) = (2\ell + 1)\Delta\ell f_{sky}$ is the number of transverse modes at a given ℓ and $\Delta\ell$ is typically chosen to make Cov block-diagonal (Dodelson 2003; Cabré et al. 2007; Crocce, Cabré, & Gaztañaga 2011). For simplicity we consider an ideal full sky survey and use $\Delta\ell = 1$ and $f_{sky} = 1$. In this way we avoid correlations between different modes in the covariance matrix, which is diagonal with respect to ℓ (which is consistent with assuming the 3D covariance is also diagonal in k).

Therefore, for each ℓ we define a matrix with $N(N+1)/2$ elements, where $N = N_z(N_z + 1)/2$ is the number of observables discussed in Sec. 3.2.3, to account for the covariances and cross-covariances of auto and cross-correlations. In order to include observational noise we add to the auto-correlations in Eq. (3.25) a shot noise term

$$C_\ell^{obs,ij} = C_\ell^{ij} + \delta_{ij} \frac{1}{\frac{N_{gal}(j)}{\Delta\Omega}} \tag{3.26}$$

that depends on the number of galaxies per unit solid angle included in each radial bin. In our case we control this number with N_{gal} in Eq. (3.1.

Finally, we define the χ^2_{2D}. We assume that the observed power spectrum C_ℓ^{obs} correspond to our fiducial cosmological model discussed in Sec. (3.2.5), while we call C_ℓ^{mod} the one corresponding to the cosmology being tested,

$$\chi^2_{2D} = \sum_\ell \left(C_\ell^{obs} - C_\ell^{mod}\right)^\dagger \mathrm{Cov}_\ell^{-1} \left(C_\ell^{obs} - C_\ell^{mod}\right). \tag{3.27}$$

Each term in this sum is the product of $N_z(N_z+1)/2$-dimensional vectors C_ℓ^{ij} where (ij) label all possible non-redundant correlations of N_z redshift bins, and a $N_z(N_z+1)/2 \times N_z(N_z+1)/2$ matrix corresponding to their (inverse) covariance.

3.2.4 Nonlinear Scales

Both χ_{3D} and χ_{2D} depend sensibly on the maximum k_{max} (or minimum scale) allowed in the analysis. For our purposes, we have chosen to fix k_{max} for all the bins and relate it to angular scales through $\ell_{max} = k_{max}\, r(\bar{z})$, where $\bar{z}$ is the mean redshift of the survey. In our fiducial cosmology we find $r(\bar{z}) = 1471\, h^{-1}\,\mathrm{Mpc}$ in the redshift range $0.45 < z < 0.65$ and $r(\bar{z}) = 2219\, h^{-1}\,\mathrm{Mpc}$ when $0.4 < z < 1.4$. In addition, we do not consider a dependence of l_{max} with redshift (i.e. same ℓ_{max} for all redshift bins and their cross-correlation).

For the largest scale we use $k_{min} = 10^{-4}\, h\,\mathrm{Mpc}^{-1}$ in the 3D analysis and $\ell_{min} = 2$ in the angular case. Let us notice that we have not found any significant dependence on k_{min} or ℓ_{min}.

3.2.5 Cosmological model

We assume the underlying cosmological model to be a flat ΛCDM universe with cosmological parameters $w = -1$, $h = 0.73$, $n_s = 0.95$, $\Omega_m = 0.24$, $\Omega_b = 0.042$ and $\sigma_8 = 0.755$. These parameters specify the cosmic history as well as the linear spectrum of matter fluctuations today $P(k, z = 0)$. The parametrized linear growth rate is give by, Eq. (2.42) and the growth history by Eq. (2.43).

The parameter γ used in Eq. (2.42) is usually employed as an effective way of characterizing modified gravity models that share the same cosmic history as GR but different growth history (Wang & Steindhardt 1998; Linder 2005). In part of our analysis we focus in ΛCDM models and assume the GR value $\gamma = 0.545$. We deviate from this in Sec. 3.3.1 were we take γ as a free parameter independent of redshift.

3.2.6 Likelihood analysis

In order to find constraints on cosmological models we integrate over the space of parameters defining the model, finding the value of the likelihood given by

$$-2\log\mathcal{L} \propto \chi^2, \tag{3.28}$$

where we approximate the likelihood as Gaussian in the power spectra. Given the prior ϑ on the parameters one defines a probability for each sampled point i in parameter space given by

$$\mathcal{P}(i) \propto \mathcal{L}(i) \times \vartheta(i). \tag{3.29}$$

Finally, the mean and covariance matrix of the parameters is obtained from

$$\bar{p}_a = \sum_i \mathcal{P}(i) p_a(i) \tag{3.30}$$

$$\Sigma_{(p_a,p_b)} = \sum_i \mathcal{P}(i)(p_a(i) - \bar{p}_a)(p_b(i) - \bar{p}_b), \tag{3.31}$$

where $p_a(i)$ is the value of the parameter a in the grid point i, $\bar{p}_a$ is the mean value and $\Sigma_{(p_a,p_b)}$ is the covariance between parameter a and b. In Eqs. (3.30,3.31) $\mathcal{P}(i)$ is normalized to unity over the grid. In addition we assume flat priors.

By construction the likelihood peaks at the fiducial value considered in the analysis. In all our studies we have chosen wide prior limits and therefore have found no dependance with these limits, and find the mean agrees with the fiducial value and the posteriors are quite Gaussian. When there is only one free parameter p, like in bias fixed case, we found the standard deviation solving the equation $\chi^2(p) - 1 = 0$. This expression is valid in the context in which the best fit value corresponds exactly to the fiducial parameters and $\chi^2 = 0$ at this point.

3.2.7 Figures of merit

We consider two different analyses in order to compare 3D clustering with 2D tomography including all the auto and cross-correlations between redshift bins.

On the one hand, a *bias fixed case*, in which we only vary Ω_m (which affects both the shape and the amplitude of the power spectrum, and can be constrained as if we had a good knowledge of the bias prior to the analysis).

On the other hand we consider a *bias free case*, in which only b and γ (hence f through Eq. (2.42)) are allowed to vary. This changes the (anisotropic) amplitude of the power spectrum, but not the underlying shape. This case is virtually the same as the standard analysis of redshift space distortions (White, Song & Percival 2009; Ross et al. 2011). For this case we had to adapt `CAMB_sources` slightly, see the discussion in Appendix A.

To make the comparison quantitative we define a figure of merit (FoM) based on the covariance matrix Σ,

$$FoM_S = \sqrt{\frac{1}{\det[\Sigma]_S}}, \tag{3.32}$$

where S is the subspace of parameters we are interested in. If this subspace correspond to only one parameter, then the FoM is the inverse of the square root of the variance of the corresponding parameter. Thus we have the following cases,

- FoM$_{\Omega_m}$: Constraints on Ω_m, with other parameters fixed at fiducial values.
- FoM$_b$ and FoM$_\gamma$: bias and γ constraints when marginalized over γ and bias, respectively. Other parameters are fixed at their fiducial values.
- FoM$_{b\gamma}$: Joint constraint on bias and γ, with other parameters fixed at fiducial values.

3.3 Results

In this part, we show the results for the different cases considered. First of all, we show the forecasts on Ω_m for the spectroscopic survey defined in section 3.2.1. Then, for the same survey we present the forecasts in the bias free case, where b_g and γ are the free parameters.

For the photometric surveys, we only focused on the bias fixed case, although redshift space distortions are present in photometric surveys, using photometric redshift bins, see (Nock, Percival,& Ross 2010; Ross et al. 2011; Asorey et al. 2013) or (Padmanabhan et al. 2007; Blake et al. 2007; Thomas et al. 2010; Crocce et al. 2011) for actual measurements of redshift space distortions using LRG samples of SDSS. We forecast constrains in Ω_m in the narrow-band photometric survey described in 3.2.1.

In every case, we reproduce the forecasts for three different minimum scales, $k_{max} = \{0.05, 0.1, 0.2\}\, h\,\mathrm{Mpc}^{-1}$ and the corresponding ℓ_{max} in the 2D analysis. The predictions have been made for the bin configurations of tables 3.1 in the spectroscopic and narrow-band surveys and table 3.3 configuration for the broad-band survey.

3.3.1 Spectroscopic survey

Bias fixed case

Let us compare the constrains of 2D and 3D methods applied to the spectroscopic survey described in 3.2.1. In the top panels of figure 3.2 we show the evolution of the figure of merit of Ω_m in the 2D and 3D cases with respect the number of redshift bins N_z and for three different k_{max} and $\ell_{max} = k_{max} r(\bar{z})$.

Dashed lines correspond to 3D constrains, fitted using (3.9) and (3.11) while figures of merit corresponding to the full 2D case, including all the auto- and cross-correlations between redshift bins are shown in solid lines, where the fitting is done according to 3.27. Left panel corresponds to low show noise sample and right panel to the high shot noise case.

We see that all the figures of merit increase with a higher value of k_{max}. This is expected because we would be including more modes in the χ^2 computation. In other words, we are including more information in the fitting and therefore the constrains improve.

We do not see dependance on 3D FoM with respect the number of bins. In eq. (3.9) we see that the dependance of χ^2 in each bin is roughly proportional to the volume of each bin. When we divide the full survey in N_z redshift bins, the χ^2 per bin is reduced in the same amount that the number of bins. When we combine χ^2 from all the bins, we recover the full 3D χ^2 of the bin covering the whole survey. This pattern has been found in all the analysis we have made. Despite the fact, we have delivered the same treatment to the 3D case in all the different section, for the purposes of this work, we can consider that we are comparing 2D case using multiple bins with the 3D result of the whole survey, with no division in bins.

This picture changes for the 2D tomography. Here the transverse information is fixed once ℓ_{max} is set (there are $2\ell + 1$ modes per ℓ value, up to ℓ_{max}). As we increase the number of narrower bins N_z (with fixed total redshift range) we have several effects:

1. Decreasing the number of galaxies per bin increases the shot noise per bin

2. Increasing the number of bins so that they are thinner proportionally increases the signal auto power spectrum in each bin (there is less signal power suppression due to averaging along the radial direction).

3. When we split a wide redshift bin in two, we double the number of angular auto power spectra (transverse modes). This results in a larger FoM because the signal to noise in each bin remains nearly constant (the shot noise and signal in each bin both increase proportionately).

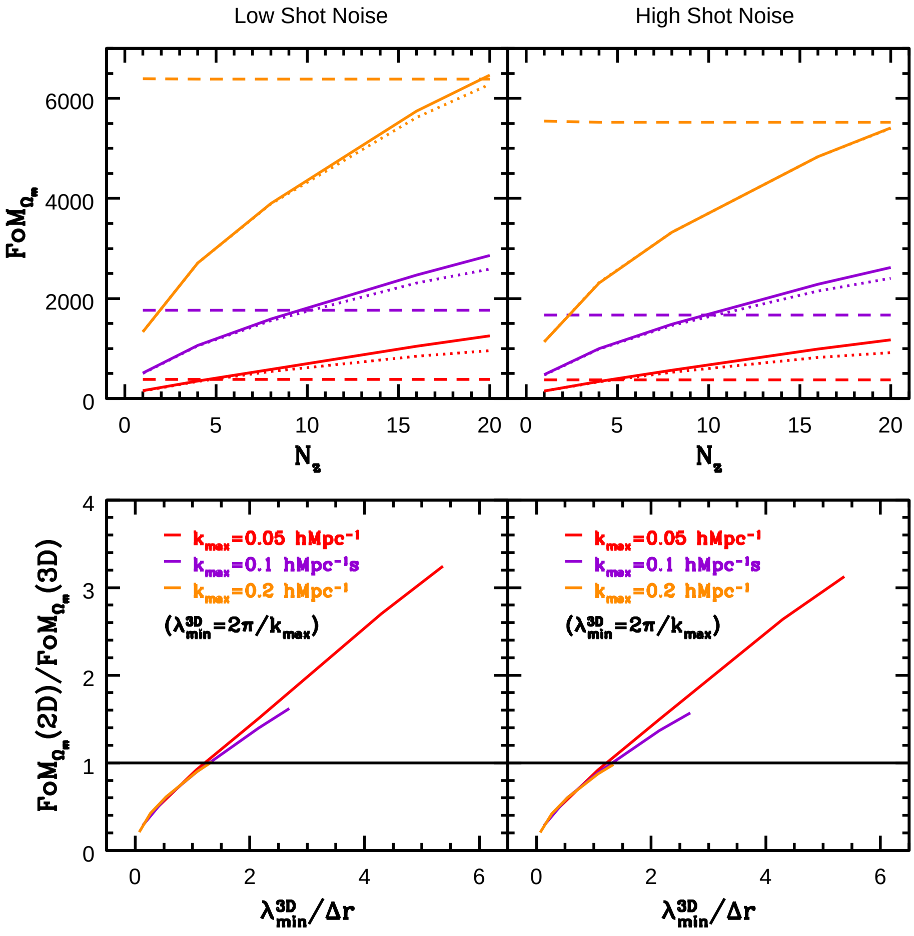

Figure 3.2: *Spectroscopic survey & bias fixed.* Top panels show FoM$_{\Omega_m}$(2D) and FoM$_{\Omega_m}$(3D) as a function of the number of bins in which we divide the survey for the analysis (left panel for a low shot-noise survey and right to a high shot noise). Dashed line corresponds to the 3D analysis, dotted to the 2D tomography using only auto-correlations and solid to auto plus cross- correlations. Different colors correspond to different minimum scales, as detailed in the bottom panel inset labels. Bottom panels show the ratio of FoM$_{\Omega_m}$(2D) (auto plus cross) and FoM$_{\Omega_m}$(3D) as a function of the bin width Δr normalized by the minimum scale assumed in the 3D analysis. Remarkably the recovered constraints from full tomography match the 3D ones for $\Delta r \sim \lambda^{3D}_{min}$ for all λ^{3D}_{min}. We note that different lines in the bottom panels are truncated differently merely because we have done the three k_{max} cases down to the same minimum Δr.

This gain is illustrated by the dotted line in Fig. 3.2, which corresponds to the FoM produced by just using auto-correlations. For even narrower redshift bins the bins will become correlated and the gain will saturate, but this is not yet the case in our results as the redshift bins are still large compared to the clustering correlation length. In the limit in which all modes of interest are very small compared to shell thickness and they are statistically equivalent, for a single power spectrum amplitude parameter one expects FoM$= 1/\sigma \propto \sqrt{N_z}$, as obtained in Fig. 3.2 for low N_z

4. When we increase the number of narrower bins, we also include information of radial modes by adding the cross-correlation between different redshift bins (illustrated by the solid line in Fig. 3.2 that corresponds to the total FoM from auto plus cross-correlations).

Note how adding the cross-correlations to the auto-correlations (solid lines in Fig. 3.2) only increases the FoM moderately as compared to the auto-correlation result (dotted line). This reflects the fact that there are fewer radial modes than transverse ones, while much of the Ω_m constraint comes from the shape of $P(k)$ that is isotropic.

The bottom panels of Fig. 3.2 show the ratio of the 2D and 3D FoM's against the bin width (instead of N_z), now normalized by the minimum scale used in the 3D analysis $\lambda^{3D}_{min} = \frac{2\pi}{k_{max}}$ (for three different k_{max} as before). We find FoM(2D) $\sim$ FoM(3D) when $\lambda^{3D}_{min} \sim \Delta r$ for all λ^{3D}_{min}. More precisely:

$$\Delta r = c\Delta z/H(z) \simeq 0.8 \ \lambda^{3D}_{min}. \tag{3.33}$$

Basically this means that the 3D clustering information is recovered once the binning is such that the radial bin width equals the minimum scale probed in the 3D analysis. In this case one is able to constrain the parameters without loss of information compared to a three dimensional analysis, though the actual range of scales around k_{max} that are used in the 2D analysis may be slightly different.

Lastly, note that including shot noise does degrade the FoM as shown in the right panel of Fig. 3.2 (comparing left column panels with right panels). However this does not change the conclusions above.

Bias free case

We now turn to the *bias free* case where we assume we know perfectly the shape of the power spectrum so that all the cosmological parameters are fixed at their fiducial values listed in section 3.2.5 except the bias b and the growth index γ, which, in this case, are free parameters.

In Fig. 3.3 we plot the combined FoM obtained for bias b and growth index γ, and the FoM of each of these 2 parameters marginalized over the other, as a function of the number of redshift bins considered in the analysis (for a fixed survey redshift range $0.45 < z < 0.65$). As in Fig. 3.2, dashed line corresponds to the 3D analysis, dotted line to the 2D tomography using only the N_z auto-correlations and solid line to the full 2D case where we add auto and cross angular correlations. Note that when we refer to using only auto- correlations this only applies to observables. The covariance of the auto- correlations does include cross-correlations of redshift bins, see Eq. (3.25).

We find a similar trend for the evolution of the different FoM of the γ and b parameters (either combined or marginalized) than when varying Ω_m, in the bias fixed case. Constraints given by spatial power spectrum are stable, while constraints from projected power spectrum in the bins increases with the number of bins in which we divide the survey. However there is a substantial difference in regards to the contribution of radial modes in the different observables. Now the contribution of cross-correlations is very large (compare solid to dotted lines in the left panel of Fig. 3.3). In fact, without cross-correlations we do not recover all the 3D information. This is because redshift space distortion information (i.e. our *bias free case*) is based in the relative clustering amplitude of modes parallel and transverse to the line of sight. The contribution from radial modes is much more evident for the γ constraint (FoM$_\gamma$ and then FoM$_{b\gamma}$) than for the bias FoM$_b$ because γ is basically what quantifies this relative clustering amplitude (in addition $f \equiv \Omega(z)^\gamma$ depends on redshift while we assume bias does not).

As we have done with FoM$_{\Omega_m}$ we show in Fig. 3.4 the dependence of the ratios between 2D and 3D FoM with respect to $\lambda^{3D}_{min}/\Delta r$. We find that both analyses produce the same constraints when the mean redshift bin width is slightly smaller than λ^{3D}_{min} (and we use auto and cross 2D correlations in the full 2D tomography). Comparing these results with the *bias fixed* case, it seems that for the RSD probe we need to extract more radial information. In this case:

$$\Delta r = c\Delta z/H(z) \simeq 0.6\ \lambda^{3D}_{min} \tag{3.34}$$

as compared to 0.8 in Eq. (3.33). This means that we have to include more radial bins when developing the fit to angular correlations than when only fitting Ω_m if we want to match the constraints from 3D clustering. This in practice corresponds to using slightly narrower redshift bins. This may also result in more information being included from radial modes with $k > k_{max}$ but it is within the assumptions and scope of this chapter

3.3.2 Photometric redshifts

In this section we show how the results found in the previous section extend to the photometric surveys detailed in Sec. 3.2.1. For concreteness we will only consider the *bias fixed* study where all cosmological parameters are fixed at their fiducial values except for Ω_m.

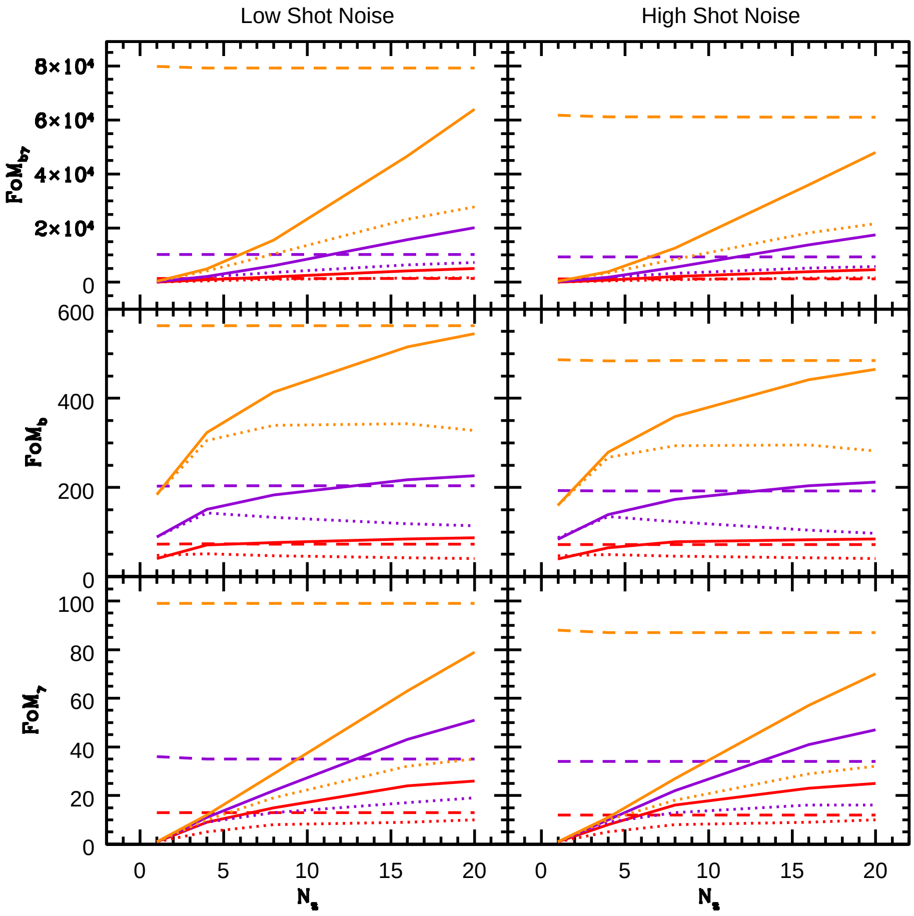

Figure 3.3: *Spectroscopic survey* & *bias free*. Top panels show the combined $b-\gamma$ constraint resulting from 3D clustering (dashed lines) or 2D tomography considering as observables only auto correlations in redshift bins (dotted lines), or adding to this the cross-correlations (solid lines). The x-axis corresponds to the number of radial bins considered in the analysis. Different colors label different minimum scales assumed (same values and labels as in Fig. 3.2). Middle and bottom correspond to individual b or γ constraints after marginalization over γ or b respectively. As for the *bias fixed* we find that 3D information can be recovered but now the role of radial modes is much for important because RSD (our *bias free* case) relies on the relative clustering amplitude of radial and transverse mode.

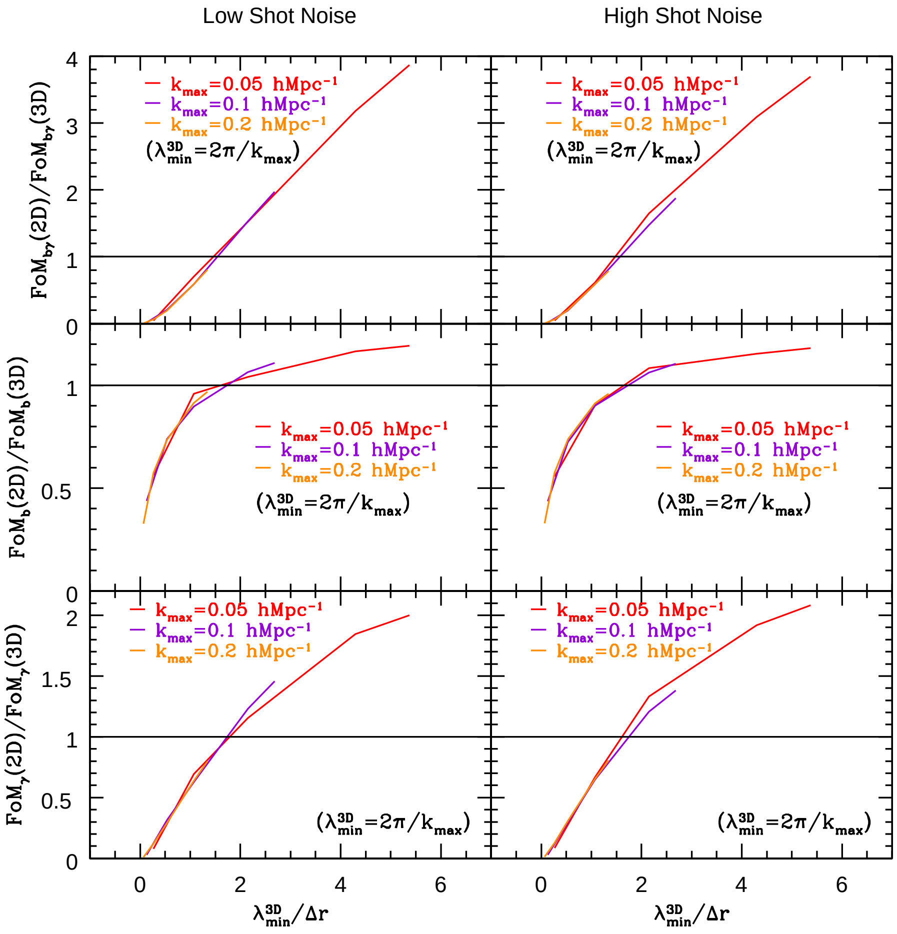

Figure 3.4: *Spectroscopic survey & bias free.* Top panels show the ratio between combined FoM$_{b\gamma}$ (2D) (auto plus cross correlations) and FoM$_{b\gamma}$ (3D) with respect to $\lambda^{3D}_{min} = 2\pi/k_{max}$, normalized by the mean width of the redshift bins Δr in the analysis. Middle and bottom panels show the same but for ratios of FoM$_b$ and FoM$_\gamma$, respectively. We show results for Low Shot Noise and High Shot Noise in left and right panels, respectively. To reconstruct RSD information in practice, one need bins slightly smaller than λ^{3D}_{min}.

Narrow-band photometric survey (PAU-like)

In top panels of Fig. 3.5 we show the Ω_m constraints (*bias fixed* case) from 3D and 2D analysis (dashed and solid lines respectively) in a narrow band photometric survey with $\sigma_z = 0.004$. In bottom panels we show how the ratio between 2D and 3D FoM depends on the ratio between the minimum scale of the 3D analysis and the mean comoving width of radial shells.

We find basically the same result as in the spectroscopic survey. Constraints from a projected or unprojected analysis are equivalent when the mean width of the radial shells (set by our binning strategy) is equal to the minimum scale considered in 3D analysis λ_{min}^{3D}. The absolute value of each FoM is degraded with respect the FoM reached with an spectroscopic survey because photo-z errors dilute clustering in the radial direction. This broadens the selection functions in the 2D analysis and introduces a cut off already at quasilinear scales in the 3D $P(k)$. In both cases the consequence is that signal to noise reduces and thus errors of observables degrade. But if we compare Fig. 3.2 and Fig. 3.5 we see that the spectroscopic survey and a photometric one with very accurate redshifts are almost indistinguishable in terms of bin width optimization.

Broad-band photometric survey (DES-like)

We now consider a deep survey ($i_{AB} < 24$) with redshifts estimated by photometry with broadband filters ($\sigma_z = 0.1$), and use the full catalogue with $0.4 < z < 1.4$. We obtain the FoM for Ω_m shown in the top left panel of Fig. 3.6.

Now the large photo-z error removes most of the radial information, thus all FoM_{Ω_m} are degraded with respect to spectroscopic and narrow-band photometric surveys. In addition, we find that FoM_{Ω_m} saturates with the number of redshift bins included in the survey for every k_{max}. This effect is produced by the overlapping between true galaxy distributions at different bins induced by photo-z transitions.

We also find that the configuration in which spatial and projected analysis constrain Ω_m equally corresponds to the same number of bins for all the k_{max} considered. Therefore, as we can see in bottom left panel of Fig. 3.6, the scale given by λ_{min}^{3D} is not ruling the dependencies. Instead it is the scale of the photometric redshifts which is affecting both clustering analyses. This is shown in the right panel of Fig. 3.6 where we plot the ratio of figures of merit (2D vs. 3D) against a new scaling : $\sigma_r/\Delta r$. We find that for a DES-like case, with the assumption of $\sigma_z = 0.1$, one needs roughly 5 bins for the 2D tomography to optimally recover the 3D clustering information. This corresponds to:

$$\Delta z \simeq 2\sigma_z. \tag{3.35}$$

With a lower σ_z the number of bins will increase.

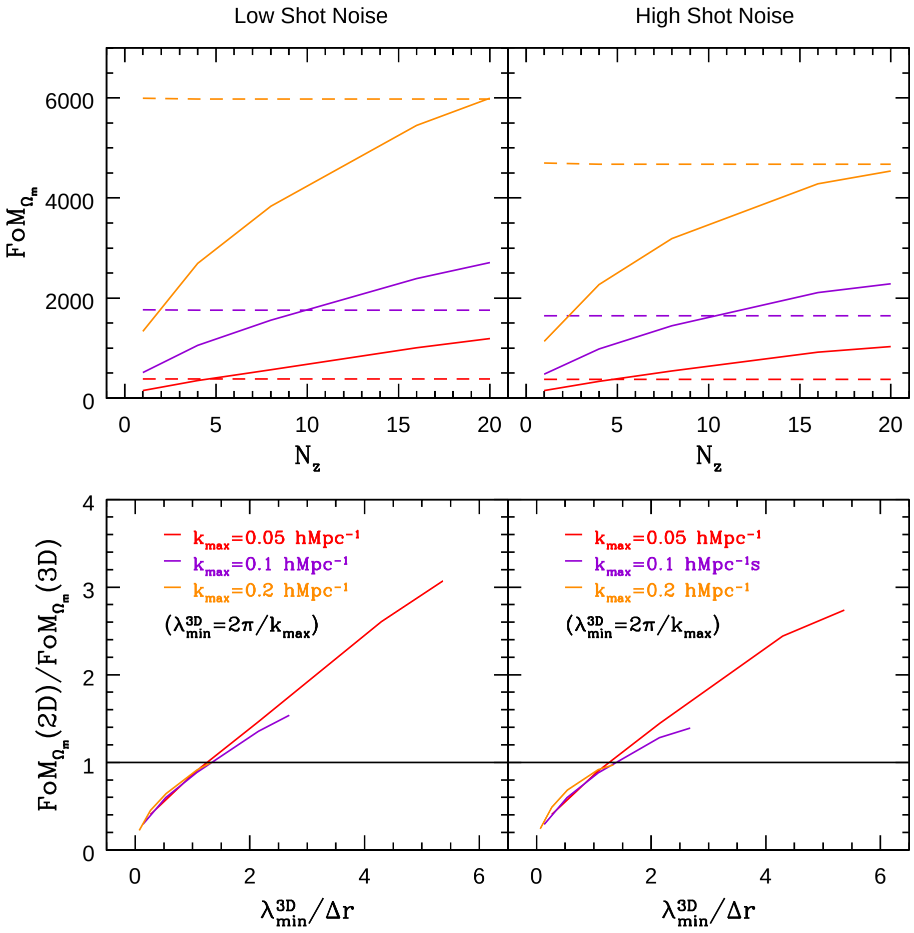

Figure 3.5: *Narrow band photometric survey (PAU-like) & bias fixed.* Top panels show figures of merit FoM$_{\Omega_m}$ (2D) (auto plus cross correlations) and FoM$_{\Omega_m}$ (3D) with respect to the number of bins for $k_{max} = \{0.05, 0.1, 0.2\}$ hMpc^{-1} (red, violet and orange colours). We plot 2D figures of merit with solid lines and 3D figures of merit using dashed lines. Bottom panels show the ratio between both figures of merit with respect to minimum scale used in 3D analysis, $\lambda^{3D}_{min} = 2\pi/k_{max}$, divided by the mean width Δr of the redshift bin. We conclude that we get similar constraints from 2D and 3D analysis when Δr is close to λ^{3D}_{min} and that in terms of bind width optimization an spectroscopic and photometric analysis are almost identical.

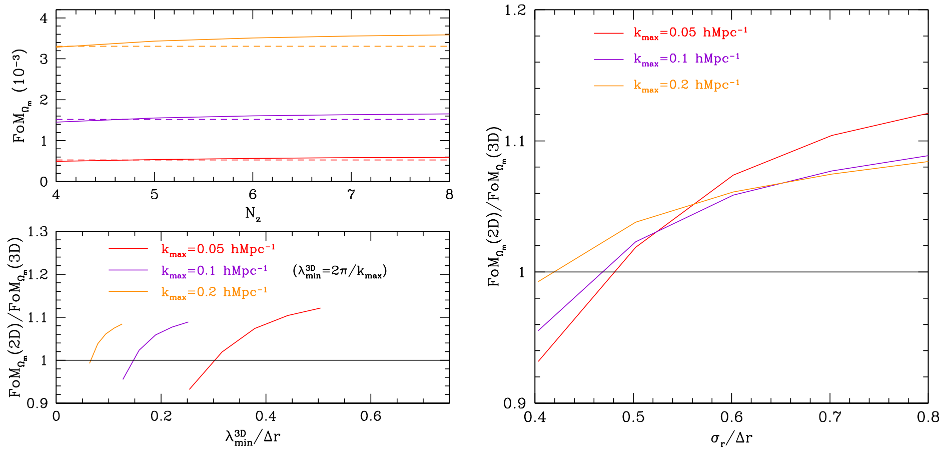

Figure 3.6: *Broad band photometric survey (DES-like) & bias fixed.* Top right panel shows the figures of merit FoM$_{\Omega_m}$ (2D) and FoM$_{\Omega_m}$ (3D) with respect to the number of bins N_z used in the analysis, for $k_{max} = \{0.05, 0.1, 0.2\}\, h\,\mathrm{Mpc}^{-1}$ (red, violet and orange colours, respectively). 2D FoM are plotted with solid lines and 3D with dashed lines, and we only consider low shot noise. Bottom left panel show the ratio of both figures of merit with respect to $\lambda^{3D}_{min} = 2\pi/k_{max}$ divided by Δr. The equivalence of the recovered FoM now changes for different k_{max}. However when this ratio is plotted with respect to the comoving scale of photo-z, σ_r (normalized by Δr) the different λ_{min} lines cross each other for $\Delta r \sim 2\sigma_r$. This implies that is the relative values of Δr and σ_r what sets the equivalence of 3D and 2D tomography. In particular, for a DES-like survey one recovers the 3D constraints from 2D analysis using 5 redshift bins.

3.4 Discussion

In this chapter, we have studied the redshift bin width that allows us to recover the full 3D clustering constraints from tomography of angular clustering (i.e. the combination of all the auto and cross correlations of redshift bins). We explore three surveys with different properties: a spectroscopic and a narrow band photometric survey in a redshift range $0.45 < z < 0.65$, and a deeper broadband photometric survey that covers redshifts in the range $0.4 < z < 1.4$. We have considered how well we can recover the shape of the power spectrum by allowing Ω_m to be free and fixing the amplitude of clustering, including bias. We call this the *bias fixed* case. We have also explored how to recover the information from redshift space distortions (RSD), by measuring the *anisotropic* amplitude of the power spectrum allowing for both a free bias and a free growth index. This is the *bias free* case. We restrict our study to quasi-linear scales and we only consider scales above some minimum scale $\lambda_{min}^{3D} = 2\pi/k_{max}$, where $k < k_{max}$ and k_{max} is either 0.05, 0.1 or 0.2 $h\,\mathrm{Mpc}^{-1}$. In angular space this corresponds to $l < l_{max} \simeq k_{max} r(z)$, where $r(z)$ is the radial distance to the mean redshift bin.

The 3D analysis has almost no dependance on the number of redshift bins because radial modes are already included in each bin. In contrast the 2D tomographic analysis depends strongly on the number of bins (or equivalently on redshift bin widths), since broad bins average down transverse power on scales smaller than the bin width, and it is only by using multiple thin shells that radial modes are included.

For the *bias fixed* case in the spectroscopic survey we have found that we recover all the information with 2D tomography when the width of the redshift bins that we use to do the tomography is similar to the minimum scale used in the 3D observables, λ_{min}^{3D}. More precisely we find that the optimal bin width is (see Fig. 3.2 and Eq. (3.33)): $\Delta r = c\Delta z/H(z) \simeq 0.8\,\lambda_{min}^{3D}$. In addition most of the 2D constraints come from autocorrelations.

When studying RSD, i.e. in the *bias free* case, we see that if we want to recover the 3D constraints we need radial shells which are slightly smaller, i.e. $\Delta r \simeq 0.6\lambda_{min}^{3D}$ (see Fig. 3.4), which means that we would need more bins than in the case in which we just want to measure the shape of $P(k)$. In addition we find necessary to include in the observables the cross correlation between redshift bins. This is expected because in the RSD case we are comparing the clustering in radial and transverse direction to the light of sight: information from radial modes should be more important than in the case in which we just study information in the isotropic shape of the power spectrum. Also note how we can not recover the 3D information from RSD when we just use autocorrelations (see dotted line in Fig. 3.3).

We found that in the *bias fixed* case, the narrow-band photometric survey is almost equivalent to an spectroscopic survey, and we therefore reach the same conclusions with respect to the optimal bin width for the tomography of galaxy counts. In the case of a deeper broadband photometric survey we find that the typical uncertainty in photometric redshifts σ_z severely limits the accuracy of the radial information for both 3D and 2D cases. In this case the information recovery does not depend strongly on λ_{min}^{3D}, because this is smaller than the scale corresponding to the photometric redshift accuracy, i.e. $c\,\sigma_z/H(z) > \lambda_{min}^{3D}$. The optimal redshift bin width in this case is simply given by $\Delta z \simeq 2\sigma_z$.

For a redshift range $0.4 < z < 1.4$ and $\sigma_z = 0.1$ (DES-like survey) we find that we will need only 5 redshift bins to constrain Ω_m using tomography with the similar precision than a full 3D analysis of the survey. In comparison, for a PAU-like survey with $\sigma_z \simeq 0.004$ and $k_{max} = 0.1$ we need about 44 redshift bins of width $\Delta z \simeq 0.023$ each.

We conclude from our analysis that it seems possible to recover the full 3D clustering information, including RSD information, from 2D tomography. This has the disadvantage of needing a potentially large number of redshift bins, and correspondingly large covariance matrices between observables. But it has the great advantage of simplifying the combination with WL and of just using observed quantities, i.e. angles and redshifts, avoiding the use of a fiducial cosmology to convert angles and redshifts into 3D comoving coordinates. In practice, probably both types of analysis should be used to seek for consistency.

Chapter 4

Redshift-space distortions from the cross-correlation of two photometric populations

4.1 Motivation

The late-time expansion of the Universe is being tested by a wide range of ongoing or planned photometric surveys like Dark Energy Survey (DES), (Annis et al. 2005), the Panoramic Survey Telescope and Rapid Response System (PanStarrs), (Hodapp et al. 2004), the Physics of the Accelerating Universe survey (PAU), (Benitez et al. 2009). In the future, wider field photometric surveys like Large Synoptic Survey Telescope (LSST), (LSST Collaboration 2012) and the imaging component of EUCLID, (Laureijs et al. 2011), will go deeper and larger. This surveys would help to understand dark energy nature throughout clustering and weak lensing, potentially, testing the possible time dependance of dark energy equation of state w.

As we mentioned in section 2.7.1, redshift space distortions can provide information about the linear growth of structures, given by eq. (2.41). RSD raise an anisotropic power spectrum, as seen in section 2.7.1 and measuring the 3D clustering and comparing parallel and transverse to the line-of-sight clustering is usually the method to use them for testing how structures grow. For example, see (Okumura et al. 2008; Guzzo et al. 2008; Cabré & Gaztañaga 2009; Blake et al. 2011; Reid et al. 2012). This, in principle, requires good radial resolution from spectroscopy or narrow-band photometry.

But, it exists the possibility to detect the effect of redshift-space distortions selecting galaxy samples in redshift bins and then projecting the radial information, measuring the angular clustering of galaxy samples, see (Nock, Percival,& Ross 2010; Crocce, Cabré, & Gaztañaga 2011; Ross et al. 2011). This has been already applied to a sample of photometric Luminous Red

Galaxies (LRG) in (Padmanabhan et al. 2007; Blake et al. 2007; Thomas et al. 2010; Crocce et al. 2011). Photometric surveys have the potentiality of observing a high number density of galaxies at high redshifts. This would allow us to prove the growth of structures at this high redshifts.

Those analysis in photometric surveys only considered auto-correlations in redshift bins. Here, we add to this analysis the cross-correlations between bins, motivated by the previous chapter and (Asorey et al. 2012), in which it is shown that full spatial (3D) constrains are recovered with tomographic (2D) analysis.

On the other hand, we investigate how the fitting to growth rate improves if two different populations are considered, and the cross-correlations between both correlations. Previous studies, (McDonald & Seljak 2009; White, Song & Percival 2009; Gil-Marín et al. 2010) have shown that, for spectroscopic surveys, if different tracers of the same field are combined, then sampling variance decrease and constrains in the growth of structure improve.

4.2 Methodology

Fiducial survey and galaxy samples

We characterize our fiducial survey by a the redshift range and the survey area. Within survey standards, we characterize the different galaxy samples that we consider by the galaxy bias of each one, b_g, the redshift distribution of galaxies in each sample and the photometric accuracy of the redshift estimates, σ_z.

The fiducial survey is similar to the expected full DES. The redshift range is $0.4 < 1.4$ and the area is one octant of the sky, i. e., $f_{sky} = 1/8$. The redshift distribution of sample α is

$$\frac{dN_\alpha}{dzd\Omega} = N^\alpha_{gal}\left(\frac{z}{0.5}\right)^2 e^{-\left(\frac{z}{0.5}\right)^{1.5}} \tag{4.1}$$

where N^α_{gal} is given by the total number of galaxies in α population sample. In many cases, we will consider two populations, one with bias $b = 1$ and $\sigma_z = 0.05(1+z)$ (Pop 1), similar to a main sample of the survey, and another with $b = 2$ and $\sigma_z = 0.03(1+z)$ (Pop 2), that can be an LRG sample. Notice that we omit the galaxy subscript in bias notation.

We consider the same redshift distribution of galaxies for all the samples, unless otherwise stated. The fiducial comoving number density is $n(z = 0.9) = 0.023h^3\text{Mpc}^{-3}$. This corresponds to a number of $\sim 3 \times 10^8$ galaxies within the survey redshift and area range. This matches the expected number of galaxies that will be targeted above the magnitude limit of DES, $i < 24$.

Number of bins N_z	$\Delta z/(1+z)$
4	0.15
6	0.1
8	0.08
12	0.05
19	0.03

Table 4.1: The different redshift bin configurations considered, within a photometric redshift range of $0.4 < z < 1.4$. We show the total number of bins and their redshift width Δz (which evolves with redshift in the same manner as the photo-z).

In this case, the photometric accuracy evolves linearly with redshift. Hence, the bin widths of the radial shells in which we divide the redshift range do evolve, accordingly, with redshift. The different bin configurations used in this chapter are shown in table 4.1

4.2.1 Angular power spectrum

As in the previous chapter, we study angular clustering using the angular power spectrum of the projected overdensities in the space of spherical harmonics. In section 3.2.3 we showed that the auto-correlation power spectrum at redshift bin i, for a single population, is given by:

$$C_\ell^{ii} = \frac{2}{\pi} \int dk\, k^2 P(k) \left(\Psi_l^i(k) + \Psi_l^{i,r}(k) \right)^2 \tag{4.2}$$

where the projection in the bin is encoded in the kernel function

$$\Psi_\ell^i(k) = \int dz\, \phi_i(z) b(z) D(z) j_\ell(kr(z)) \tag{4.3}$$

In redshift space, the kernel has another term that should be added to Ψ_ℓ^i,

$$\begin{aligned} \Psi_\ell^{i,r}(k) &= \int dz\, \phi_i(z) f(z) D(z) \left[\frac{2l^2+2l-1}{(2\ell+3)(2\ell-1)} j_\ell(kr) \right. \\ &- \frac{\ell(\ell-1)}{(2\ell-1)(2\ell+1)} j_{\ell-2}(kr) \\ &- \left. \frac{(\ell+1)(\ell+2)}{2\ell+1)(2\ell+3)} j_{\ell+2}(kr) \right] . \end{aligned} \tag{4.4}$$

that includes the linear Kaiser effect (Fisher, Scharf & Lahav 1994; Padmanabhan et al. 2007). . In Eqs. (4.3,4.4) $b(z)$ is the bias (assumed linear and deterministic), $D(z)$ is the linear growth factor and $f(z)$ is the linear growth rate. Photo-z effects are included through the radial selection function $\phi(z)$, see below.

For the case of 1 population, there are N_z auto-correlation spectra, one per radial bin. Then, we add to our observables the $N_z(N_z-1)/2$ cross-correlations between different redshift bins. These are given by

$$C_\ell^{ij} = \frac{2}{\pi}\int dk\; k^2 P(k)\left(\Psi_\ell^i(k) + \Psi_\ell^{i,r}(k)\right)\left(\Psi_\ell^j(k) + \Psi_\ell^{j,r}(k)\right) \tag{4.5}$$

Therefore, we are considering $N_z(N_z+1)/2$ observable angular power spectra when reconstructing clustering information from tomography using N_z bins, for a single tracer.

If we combine the analysis of two tracers, α and β, the angular power spectrum is given by

$$\begin{aligned} C_\ell^{i_\alpha j_\beta} &= \frac{2}{\pi}\int dk\; k^2 P(k)\left(\Psi_\ell^{i_\alpha}(k)\right. \\ &+ \left.\Psi_\ell^{i_\alpha,r}(k)\right)\left(\Psi_\ell^{j_\beta}(k) + \Psi_\ell^{j_\beta,r}(k)\right), \end{aligned} \tag{4.6}$$

where Ψ_ℓ^i and $\Psi_\ell^{i,r}$ characterize each galaxy sample through the radial selection function $\phi_i(z)$ and the bias $b(z)$ in expressions (4.3) and (4.4) . We use the general notation where $C_\ell^{i_\alpha j_\beta}$ is the correlation between redshift bin i of population α with redshift bin j of population β. By definition,

$$C_\ell^{i_\alpha j_\beta} = C_\ell^{j_\beta i_\alpha} \tag{4.7}$$

$$C_\ell^{i_\alpha j_\beta} \neq C_\ell^{j_\alpha i_\beta} \quad \text{for} \quad \alpha \neq \beta; i \neq j \tag{4.8}$$

Then the total number of observables is $2N_z(2N_z+1)/2$ if we consider the same redshift bins configuration for both populations, in the case in which both are correlated.

Radial selection functions

The radial selection functions ϕ_i in Eqs. (4.3,4.4) encode the probability to include a galaxy in the given redshift bin. Therefore, they are the product of the corresponding galaxy redshift distribution and a window function that depends on selection characteristics (e.g binning strategy),

$$\phi_i^\alpha(z) = \frac{dN_\alpha}{dz}\, W_i(z) \tag{4.9}$$

where dN_α/dz is given by Eq. (4.1). We include the fact that we are working with photo-z by using the following window function:

$$W_i(z) = \int dz_p P(z|z_p) W_i^{ph}(z_p), \tag{4.10}$$

where z_p is the photometric redshift and $P(z|z_p)$ is the probability of the true redshift to be z if the photometric estimate is z_p. For our work we assume a top-hat selection $W_i^{ph}(z_p)$ in photometric redshift and that $P(z|z_p)$ is Gaussian with standard deviation σ_z. This leads to,

$$\phi_i^\alpha(z) \propto \frac{dN_\alpha}{dz}\left(\mathrm{erf}\left[\frac{z_{p,max}-z}{\sqrt{2}\sigma_z^\alpha}\right] - \mathrm{erf}\left[\frac{z_{p,min}-z}{\sqrt{2}\sigma_z^\alpha}\right]\right) \tag{4.11}$$

where $z_{p,min}$ and $z_{p,max}$ are the (photometric) limits of each redshift bin considered and σ_z^α is the photometric redshift error of the given population α at the corresponding redshift.

Covariance matrix of angular power spectra

We assume that the overdensity field is given by a Gaussian distribution and therefore, the covariance between correlation $C_\ell^{i_\alpha j_\beta}$ and correlation $C_\ell^{p_\alpha q_\beta}$ is given by

$$\mathrm{Cov}_{\ell,(i_\alpha j_\beta)(p_\mu q_\nu)} = \frac{C_\ell^{obs,i_\alpha p_\mu} C_\ell^{obs,j_\beta q_\nu} + C_\ell^{obs,i_\alpha q_\nu} C_\ell^{obs,j_\beta p_\mu}}{N(l)} \tag{4.12}$$

where $N(\ell) = (2\ell+1)\Delta\ell f_{sky}$ is the number of transverse modes at a given ℓ provided with a bin width $\Delta\ell$. We set $\Delta\ell = 2/f_{sky}$, the typically chosen value to make Cov block-diagonal (Cabré et al. 2007; Crocce, Cabré, & Gaztañaga 2011). In this case, bins in ℓ are not correlated between them.

Therefore, for each ℓ bin, we define a matrix with $2N_z(2N_z+1)/2$ rows, where N_z is the number of redshift bins, taking into account the covariances and cross-covariances of auto and cross-correlations between each population and among them. In order to include observational noise we add to the auto-correlations of each population in Eq. (4.12) a shot noise term

$$C_\ell^{obs,i_\alpha j_\beta} = C_\ell^{i_\alpha j_\beta} + \delta_{i_\alpha j_\beta}\frac{1}{\frac{N_{gal}(j_\beta)}{\Delta\Omega}} \tag{4.13}$$

that depends on the number of galaxies per unit solid angle included in each radial bin. We define the χ assuming the observed power spectrum C_ℓ^{obs} corresponds to our fiducial cosmological model discussed in Sec. (4.2.2), while we call C_ℓ^{mod} the one corresponding to the cosmology being tested,

$$\chi^2 = \sum_\ell \left(C_\ell^{obs} - C_\ell^{mod}\right)^\dagger \mathrm{Cov}_\ell^{-1}\left(C_\ell^{obs} - C_\ell^{mod}\right). \tag{4.14}$$

4.2.2 Cosmological model and growth history

We assume a flat ΛCDM with cosmological parameters $w=-1$, $h=0.7$, $n_s=0.95$, $\Omega_m=0.25$, $\Omega_b=0.045$ and $\sigma_8=0.8$. These parameters specify the cosmic history as well as the linear matter power spectrum of fluctuations $P(k)$ at redshift $z = 0$. As usual, the growth rate is

$$f(z) \equiv \Omega_m(z)^\gamma$$

and $\gamma = 0.545$ for ΛCDM. Consistently with this the growth history is given by Eq. (2.43). In order to forecast the constrains on γ we consider it as a free parameter independent of redshift.

With these ingredients, we do a mock likelihood sampling in which we assume that the theoretical values for the correlations at the fiducial value of the parameters corresponds to the best fit position. The likelihood is based on the χ^2 given in (3.27). In our case, we keep fixed all the parameters and only allow γ to vary, and then we estimate 68% confidence limits of it. In the case in which we show constrains on $f\sigma_8$, we vary this quantity (that now depends on redshift, thus the number of fitting parameters is a function of the bin configuration), fixing the rest of parameters. The maximum ℓ considered in the analysis is $\ell_{max} = r(\bar{z}_{Survey})k_{max} \sim 220$ for $k_{max} = 0.1\,h\text{Mpc}^{-1}$, while for the largest scales we set $l_{min} = 2$. We had to adapt `CAMB_sources` in order to constrain γ or $f\sigma_8$ using the technique described in the Appendix A.

4.3 Results

In this section we discuss the constrains on the growth index, γ defined in Eq. (2.42) as obtained for the different redshift bin configurations of Table 4.1. First of all, we study how well we can determine γ using different single galaxy populations but including as observables also the cross- correlation between bins (for a given single population). We also study how the constrains depend on the bias and in the photometric redshift accuracy of the different galaxy samples. Then, we study the precision achievable when one combines different tracers in the analysis and how this depends on bias, photo-z and in particular, the shot-noise level of the sample.

Lastly we discuss the constrains that we obtain when looking into the more standard $f(z)\sigma_8(z)$ as a function of redshift, and consider auto and cross-correlations of one or two galaxy samples.

4.3.1 Redshift-space distortions with a single photometric population

Let us first consider the constrains on the growth index using single photometric populations. Figure 4.1 shows the 1-σ errors expected on γ from a combined analysis of all the consecutive photometric redshift bins in the redshift range $0.4 < z < 1.4$ as a function of the bin width (i.e. each of the configurations detailed in Table 1)[1].

In red we show the constrains on γ corresponding to an LRG-type sample, with bias $b = 2$ and a photometric redshift $\sigma_z/(1+z) = 0.03$ (Pop2). Blue lines correspond to an unbiased population with $\sigma_z/(1+z) = 0.05$ (Pop1).

Dashed lines correspond to the case in which we only use the auto-correlations in each redshift bin while solid lines corresponds to the full 2D analysis that includes all the cross-correlations in our vector of observables. Recall than in the first case the cross-correlations are included in the covariance matrix of the auto-correlations (but not as observables). We see that constrains from a full 2D analysis, including auto and cross-correlations are a factor ~ 2 or more better than those from using only auto-correlations.

From Fig 1 it is clear that in all cases the bin configuration can be optimized, with the best results obtained when $\Delta z \sim \sigma_z$. In addition, there is a competing effect between σ_z and bias. For broad bins ($\Delta z \gg \sigma_z$) the photo-z of the populations is masked in the projection and the bias dominates the γ constrains. Smaller bias gives more relevance to RSD and better γ constrains. As one decreases the bin width the population with better photo-z (typically the brighter, with higher bias), denoted Pop2, allows a more detailed account of radial modes improving the derived errors on γ more rapidly than Pop1 until they become slightly better. This optimization is possible until one eventually reaches bin sizes comparable to the corresponding photo-z (what sets an "effective" width) and the constrains flatten out.

In Fig. 4.2 we study in more detail the dependence of constrains with respect to galaxy bias b and photo-z accuracy. In the top panel of Fig. 4.2 we show standard deviation of the growth index, $\Delta\gamma$, fixing the sample bias to $b = 1$ and allowing two values for photo-z accuracy. Red line represents a sample in which $\sigma_z/(1+z) = 0.05$ while blue line has an error of $\sigma_z/(1+z) = 0.03$. In both cases the constrain flattens once $\Delta z \sim \sigma_z$ and the optimal error improves roughly linearly with σ_z. The dependence on the linear galaxy bias, b, is shown in the bottom panel of Fig. 4.2 (for fixed σ_z). We see that the constrains degrade almost linearly with increasing bias (see also (Ross et al. 2011)). As discussed before, this is because the lower the bias the larger the relative impact of RSD, which results in better constraints on γ.

In summary we have shown that using the whole 2D tomography (auto +cross correlations) allows considerable more precise measurements of γ, a factor of 2 or better once the bin width is optimal for the given sample. Hence in what follows we concentrate in full tomographic analysis.

---

[1] Note that different redshift bins can be strongly correlated depending on bin width and photo-z. We do include this covariance.

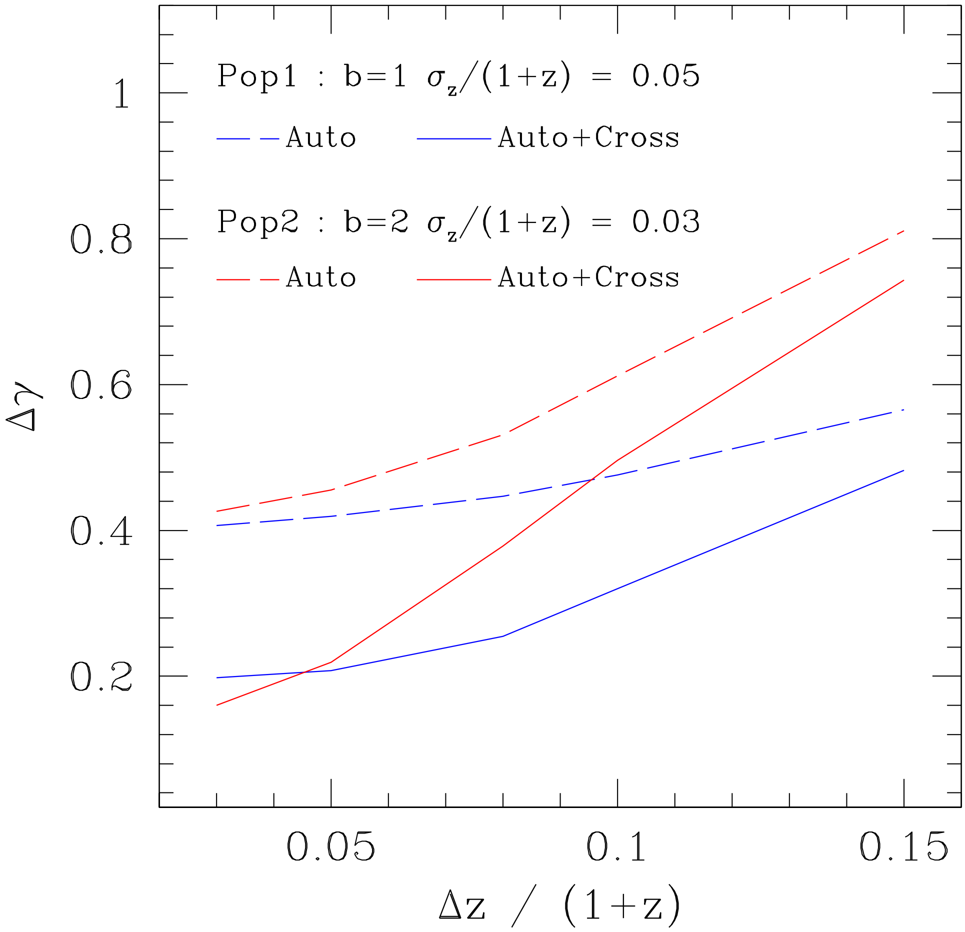

Figure 4.1: *The gain from adding redshift-bins cross-correlations.* Dashed lines show the expected 1-σ constrains in γ from the combined analysis of angular auto-correlation in photo-z bins spanning $0.4 < z < 1.4$, as a function of the bin width $\Delta z/(1+z)$ (see Table 3.3 for the corresponding total number of bins). Different colors correspond to different populations with bias and σ_z as labeled. Solid lines show, for each population, the same study but also including all the cross-correlations between bins (and their complete covariance). For optimal bin widths $\Delta z \lesssim \sigma_z$ the gain from including cross-correlations is ~ 2 or better.

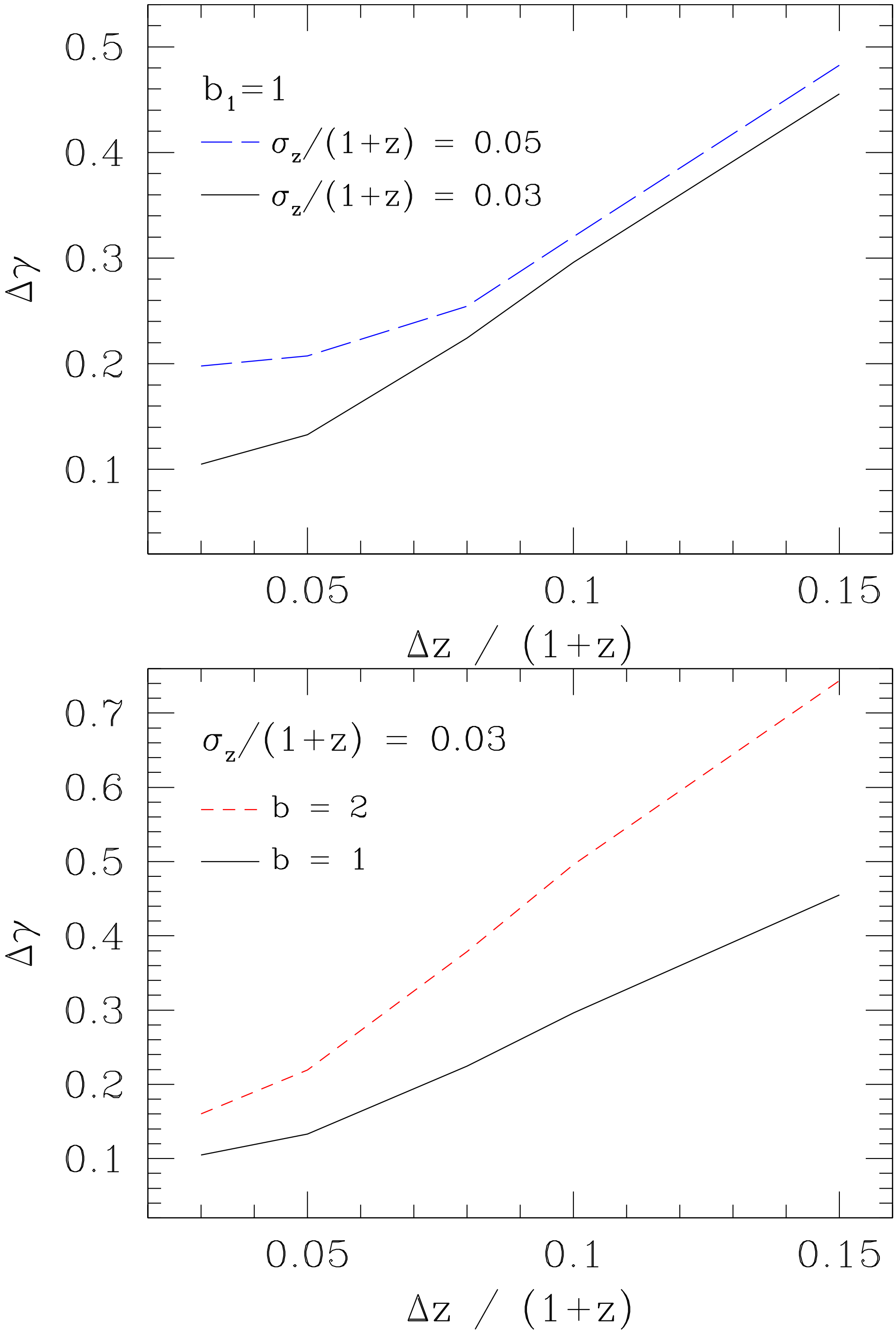

Figure 4.2: Dependence on photo-z (top panel) and bias (bottom panel) for a one-population constrains in γ, as a function of bin width (same as in Fig. 4.1). The panels show that lower b and/or lower σ_z yields better constrains in γ. This is hence a competing interplay because lower b would correspond to a fainter sample with typically worse photometric errors. The dependence on bias seems however slightly stronger.

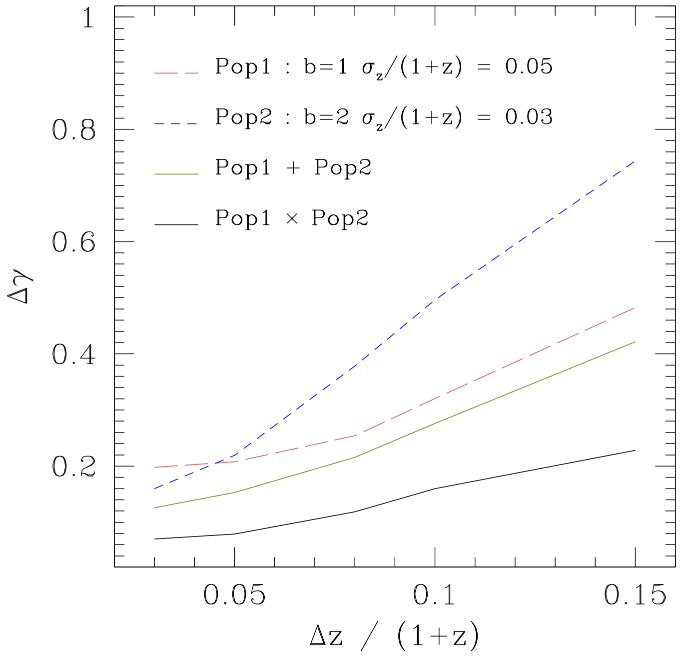

Figure 4.3: *The gain from combining galaxy populations*: Comparison of the 68% standard deviations in the growth index from single population analysis (dashed lines) with respect to the combined analysis of these two populations over the same field (black solid), using all the angular auto and cross-correlations. Remarkably the combination yields errors at least 2 times better than any of the single population cases. The solid green line corresponds to the combination of the two samples assuming they are independent (i.e. from different parts of the sky). As shown, the combination of correlated populations (same sky) yield stronger constrains than any other case.

4.3.2 Redshift-space distortions with 2 photometric populations

We now turn to an analysis combining two galaxy populations as two different tracers of matter. In Figure 4.3 we compare the constrains from single tracers with respect to the combination of both. As before the populations used in the comparison correspond to $b = 1$ and $\sigma_z/(1 + z) = 0.05$ (Pop 1) and a population with $b = 2$ and $\sigma_z/(1 + z) = 0.03$ (Pop 2). Their respective constrains in γ are the dashed red and blue lines (same as solid lines in Fig. 4.1).

If we combine both tracers and their cross-correlation in the same analysis we obtain the constrains given by black solid line, notably a factor of $2 - 3$ better compared to the optimal single population configuration.

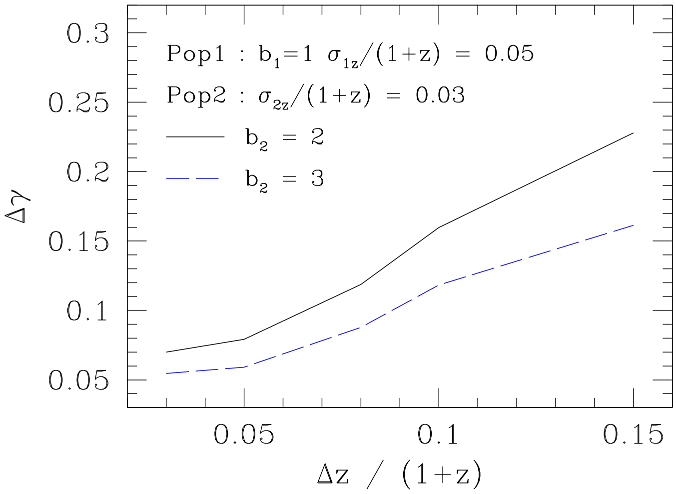

Figure 4.4: *Dependence on bias.* Increasing the bias difference between the samples improves the constrains on γ. The solid black line corresponds to the combination Pop1 × Pop2 of a highly biased sample such as LRGs (Pop2) with an unbiased one (Pop1), while the blue dashed to cluster-like bias tracer as Population 2.

In order to understand how much of this gain is due to "sample variance cancellation", in analogy to the idea put forward in (McDonald & Seljak 2009), we also considered combining the two samples assuming they are located in different parts of the sky (and hence un-correlated). We call this case Pop1+Pop2 in Fig. 4.3 (solid green line). In such scenario the total volume sampled is the sum of the volumes sampled by each population (in our case, two times the full volume of DES). This explains the gain with respect to the single population analysis. Nonetheless, the "same sky" case Pop1 × Pop2 (where cosmic variance is sampled twice) still yields better constrains, a factor of $\sim 1.5-2$, even though the area has not increased w.r.t. Pop1 or Pop2 alone.

In all, the total gain of a full 2D study with two populations (including all auto and cross-correlations in the range $0.4 < z < 1.4$) w.r.t. the more standard analysis with a single population and only the auto-correlations in redshift bins (dashed lines of Fig. 4.1) can reach a factor of ~ 5.

As a next step we show how the combined analysis of two tracers depends on the relative difference on the bias and photo-z errors of the populations. In Fig. 4.4 we keep Pop1 fix (with $b = 1$ and $\sigma_z/(1+z) = 0.05$) and we vary the bias of Pop2 from $b = 2$ (LRG type bias) to $b = 3$ (galaxy clustering like). We keep $\sigma_z/(1+z) = 0.03$ fixed for Pop2. As expected, increasing the bias difference between the samples improves the constrains on γ in a roughly linear way.

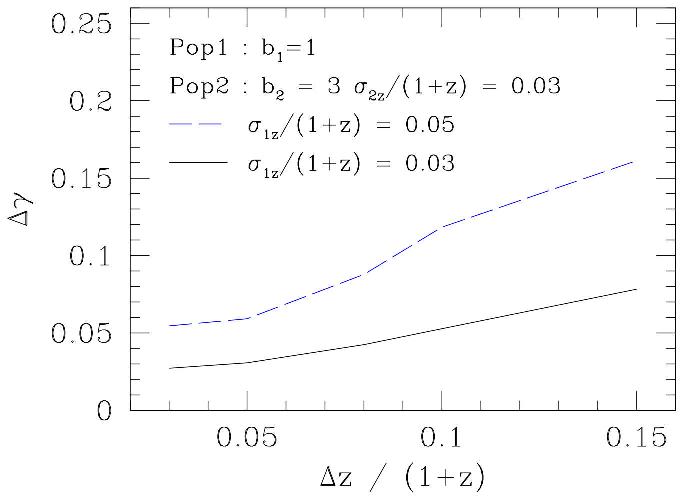

Figure 4.5: *Dependence on photometric redshift error.* Similar to Fig. 4.4 but now changing the photo-z of the unbiased sample (Pop1) for a fixed 2nd population. The error on γ depend roughly linear with $\sigma_z/(1+z)$ for optimal bin widths.

If we now have an unbiased tracer and a highly biased one with $b = 3$, while both tracers have the same $\sigma_z/(1+z) = 0.03$ we obtain constrains given by the black line in Fig. 4.5. Those constrains are better than the case in which the unbiased galaxies photo-z is worse, $\sigma_z/(1+z) = 0.05$ (given by the dashed blue line). Therefore, if we determine photometric redshifts of the unbiased galaxies with higher accuracy we will be able to measure the growth rate with higher precision.

One caveat so far is that we have always assumed that biases are perfectly known (bias fixed). Hence, in the top panel of Fig. 4.6 we show how the constrains on γ change if we instead consider them as free parameters and marginalize over. We see that the difference is very small, in particular once the bin configuration is optimal. The reason for this is clear from the bottom panel that shows the relative error obtained for the bias of each sample in the bias free case. Because the bias is so well determined (sub-percent) the marginalization over them does not impact the error on γ.

One further concern in our results is that we have assumed a perfect knowledge of the galaxy redshift distributions for both samples. In a more realistic scenario the distribution of photometric errors will be known with some uncertainty. In order to study the impact of this potential unknown we repeated the Pop1×Pop2 case (for a bin configuration $\Delta z/(1+z) = 0.1$) this time marginalizing over the value of σ_{1z} and σ_{2z} when determininig the constrain in γ (instead of fixing their values to $0.05(1+z)$ and $0.03(1+z)$). We find that the resulting $\Delta\gamma$ only increases by $\sim 10\%$ or less with respect

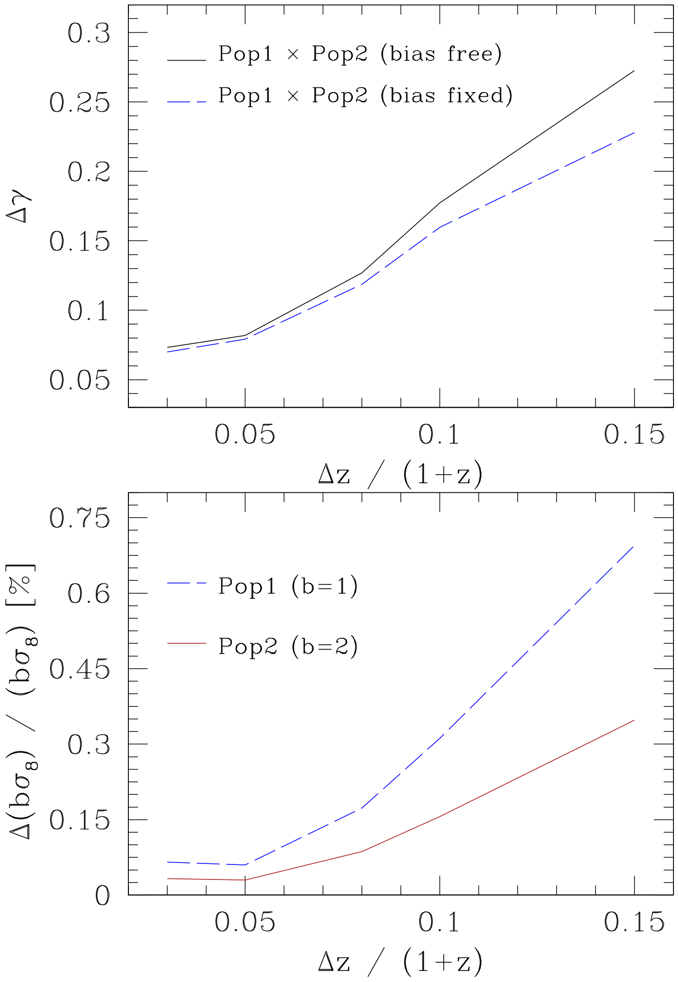

Figure 4.6: *Bias free case*: If the biases of the samples are free parameters to marginalize over we find that constrains on γ degrade only slightly compared with the bias fixed case. In particular for the thinner redshift bins configurations. This is because biases are determined with relative errors smaller than 1% (bottom panel).

to the error shown by the black solid line in Fig. 4.3. Such a small change is because the values of σ_{1z} and σ_{2z} are very well constrained after the marginalization, similar to what happens with the bias free case above.

An even more realistic analysis of this issue would allow for independent errors in the redshift distributions at each redshift bin (with some priors) rather than a global change of the mean photometric error. And possibly also a marginalization over cosmological parameter space. However our results above indicate that this should not have a major impact in our conclusions.

The impact of shot-noise

One strong limitation when it comes to implementing the "multiple tracers" technique in real spectroscopic data is the need to have all the galaxy samples well above the shot-noise limit (at the same time as having the largest possible bias difference), see for instance (Gil-Marín et al. 2010). This is cumbersome because spectroscopic data is typically sampled at a rate only slightly above the shot-noise (to maximize the area) and for pre-determined galaxy samples (e.g LRGs, CMASS). In a photometric survey these aspects change radically because there is no pre-selection (beyond some flux limits) and the number of sampled galaxies is typically very large (at the expense of course of poor redshift resolution). Therefore is interesting to investigate if the overall density of the samples have any impact in our results.

Figure 4.7 shows the constrain in γ for the combination of two samples, one unbiased population with $\sigma_z/(1+z) = 0.05$ and a population with $b = 2$ and $\sigma_z/(1+z) = 0.03$. We keep the number density for the unbiased population as $n(z = 0.9) = 1.8 \times 10^{-2}\, h^3\mathrm{Mpc}^3$ while we vary the number density of the second (typically brighter) sample. Note that we assume the same shape for $N(z)$ as given in Eq. (4.1) but we vary the overall normalization, which we characterize by the comoving number density at $z = 0.9$. The solid black line corresponds to the case in which both populations are correlated (same sky) and the dashed blue line to different areas. In both scenarios we see that decreasing the number density of the second population does not impact the error on γ unless one degrades it by an order of magnitude or more (below $n(z = 0.9) \sim 3.0 \cdot 10^{-3}$). Above this value, the error is mostly controlled by the tracer with lower bias.

4.3.3 Constraining the redshift evolution of the Growth Rate of Structure

So far we have used the combined analysis of all the redshift bins to constrain one global parameter, namely the growth rate index γ in Eq. (2.42). We now turn into constraining $f(z)\sigma_8(z)$ itself, as a function of redshift. We use a redshift bin configuration given by $\Delta z/(1 + z) = 0.1$, in the photometric range $0.4 < z < 1.4$. This configuration consist of 6 bins, and hence we fit

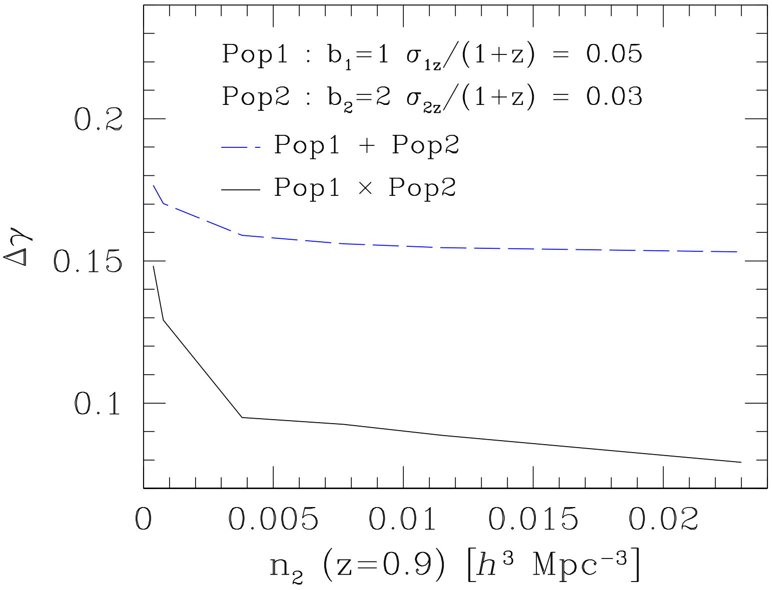

Figure 4.7: *The impact of shot noise*: We consider the combined analysis of two populations in a redshift bin configuration of $\Delta_z/(1+z) = 0.05$ and show how constrains on γ depend on the (shot) noise level of the more biased population (typically the brighter, less abundant sample). Constrains are almost un-affected unless the density drops by an order of magnitude or more compared to the one of Pop1 ($n_2 = 0.023\, h^3\,\mathrm{Mpc}^{-3}$).

$f(z)\sigma_8(z)$ evaluated at the mean of these bins. These $f\sigma_8$ values are of course correlated, and we include the proper covariance among the measurements (i.e. we do a global fit to the 6 values simultaneously).

In the left panel of Fig. 4.8 we focus on the gain from adding cross-correlations among the bins, and show the constrain on $f\sigma_8$ for a single unbiased population with photometric redshift of $\sigma_z = 0.05$ (Pop 1, in blue) and also for a single tracer with bias $b = 2$ and $\sigma_z = 0.03$ (Pop 2, in red). Dashed lines corresponds to using only auto-correlations and solid to including also all the redshift bins cross-correlations to the observables. The trend for the errors when we only use auto-correlations is similar to the one observed in Fig. 8 of (Ross et al. 2011) although in detail we are using different widths for our redshift bins and we are using C_ℓ while they used angular correlation functions, $w(\theta)$.

As in Sec. 4.3.1 there is a gain from the addition of cross-correlations, which is now split across the bins (i.e. $20 - 30\%$ for Pop1 in each of the 6 bins, and a bit less for Pop2).

In turn, the bottom panel of Fig. 4.8 focuses in the gain from combining the two tracers (and using both auto and cross-correlations among redshift bins, as in Sec. 4.3.2). Here the solid lines correspond to the single population cases discussed above, while the black short-dashed line to the combined analysis assuming these populations are correlated (same sky). For completeness the dashed green line is the result when these two samples are assumed independent. Again, there is a factor of ~ 2.5 to be gained by combining galaxy samples as opposed to only the unbiased sample.

If we compare our predictions to measurements from spectroscopic surveys like VIPERS (de la Torre et al. 2013) with constrains $f\sigma_8(z = 0.8) = 0.47 \pm 0.08$ or WiggleZ (Blake et al. 2011) where $f\sigma_8(z = 0.76) = 0.38 \pm 0.04$ we find that DES can achieve the same level of errors (10%) in determining the growth of structure but extending the constrains beyond redshift of unity. This is quite unique and interesting as there is, to our knowledge, no other spectroscopic survey expected to provide such measurements in the medium term future (before ESA/Euclid or BigBOSS).

As we did for γ, we checked that when we marginalize over photometric errors we find differences smaller than 1% in the recovered constrains in $f(z)\sigma_8(z)$ with respect to the case in which we assume perfect knowledge of the redshift distributions. For concreteness we did this cross-check for the case Pop1×Pop2 in last two redshift bins shown in Fig. 4.8.

That case of 6 bins corresponded to bin widths larger than the photometric errors of the samples, which may not be optimal but yield constrains almost uncorrelated between bins. If we define the cross-correlation coefficient for bins (i, j) ρ_{ij} as $\rho_{ij} = \mathrm{Cov}_{ij}/\sqrt{\mathrm{Cov}_{ii}\mathrm{Cov}_{jj}}$ with $\mathrm{Cov}_{ij} = \langle (x - \langle x \rangle)_i (x - \langle x \rangle)_j \rangle$ and where x stands for $f \times \sigma_8$. for the 6 bins we have the small cross-correlation of order. ($\rho_{ij} \sim -0.05$). In figure 4.3 we realized that for narrower binning the forecast were better. Then we may

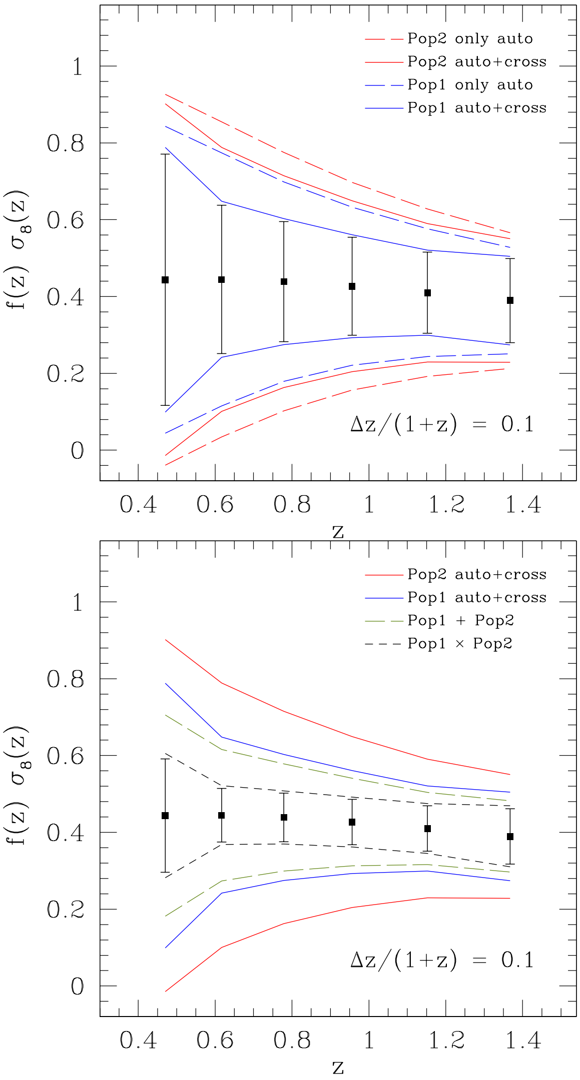

Figure 4.8: *Constrains on* $f\sigma_8$: derived at different redshift bins, for a bin configuration of $\Delta z/(1+z) = 0.1$. The top panel focuses on one population only fits, and the gain from using auto+cross correlations among all redshift bins as observables instead of just the auto-correlations. The bottom panel stresses instead the gain from combining two populations (through their auto and cross-correlations) either in different patches of the sky (Pop1+Pop2) or the same (Pop1×Pop2). In all cases Pop1 refers to a galaxy population with $b = 1$ and $\sigma_z/(1+z) = 0.05$ and Pop2 to $b = 2$ and $\sigma_z/(1+z) = 0.03$. The covariance among the derived errors on $f(z) \times \sigma_8(z)$ is taken into account in the fit. Our results show that by using RSD with two tracers a DES-like photometric survey can place 10% constrains in the evolution of $f\sigma_8$ for $z \gtrsim 0.8$.

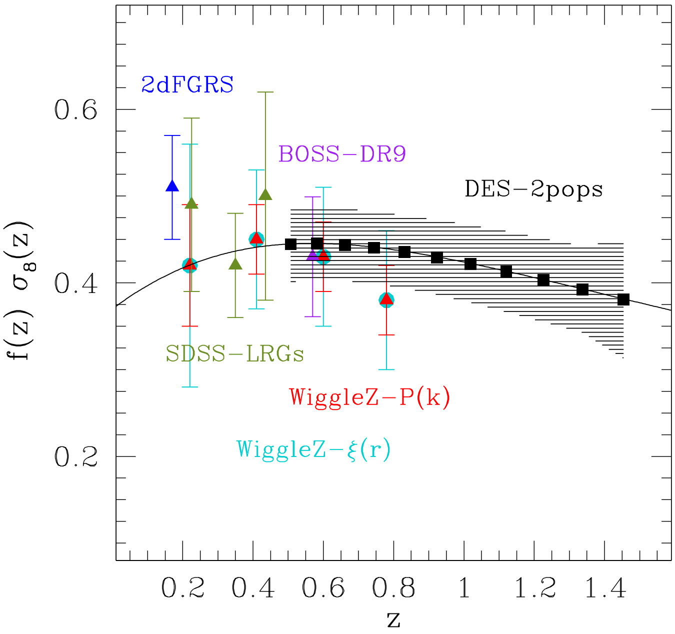

Figure 4.9: Combined constrains in the evolution of the growth rate of structure from spectroscopic data, 2dFGRS, SDSS-LRGs, Wiggle-Z and BOSS (see text for details), and forecasted for DES using two photometric populations (same as in Fig. 8). The addition of DES (shaded area) allows to trace the growth rate of structure all the way to $z \sim 1.4$.

consider the results using a binning $\Delta z/(1+z) = 0.05$. We obtained better constraints, of order $\Delta(f\sigma_8) \sim 10\%$, but the correlation between bins was higher $0.2 < \rho_{ij} < 0.65$.

Using this narrower bin configuration, we compare the DES forecast (shadowed region) in Fig. 4.9 with constraints from spectroscopic surveys, 2dFGRS (Percival et al. 2004), LRG's from SDSS (Tegmark 2006 and Cabré & Gaztañaga 2009), WiggleZ either from power spectrum (Blake et al. 2011) or correlation function (Contreras et al. 2013) and the recent BOSS results (Reid et al. 2012). This implies that DES will be able to add quite competitive constrains at high redshifts (i.e. $z \gtrsim 1$).

4.3.4 The case of high-photometric accuracy

In the previous sections we have focused in galaxy surveys with broad-band photometry for which the typical photometric error achieved is of the order 0.1 depending on galaxy sample and redshift (we assumed 0.03−0.05 (1+z)). We now turn to narrow-band photometric surveys such as the ongoing PAU or J-PAS Surveys (Benitez et al. 2009; Gaztañaga et al. 2012; Taylor et al. 2013) for which the typical radial accuracy is a factor of 10 times better:

Population	b	$\sigma_z/(1+z)$	Auto	Auto + Cross
Broad Band (BB)				
Pop1	1	0.05	0.809	0.564
Pop2	2	0.03	0.826	0.447
Pop1 × Pop2	-	-	-	0.35
Pop1 + Pop2	-	-	-	0.36
Narrow Band (NB)				
Pop1	1	0.003	0.047	0.027
Pop2	2	0.003	0.088	0.040
Pop1 × Pop2	-	-	-	0.016
Pop1 + Pop2	-	-	-	0.023

Table 4.2: Error in the growth rate γ from a combination of 21 narrow bins in the range $0.94 < z < 1.06$. The 4 top entries correspond to a Survey with Broad-Band (BB) filters: Pop1-BB assumes $b = 1$ and $\sigma_z/(1+z) = 0.05$ ("main sample") while Pop2-BB has $b = 2$ and $\sigma_z/(1+z) = 0.03$ ("LRG sample"). The 4 bottom entries correspond to a Survey with Narrow-Band (NB) filters. Here Pop1 and Pop2 have the same bias as the BB case but much precise photo-z, both with $\sigma_z/(1+z) = 0.003$.

$\simeq 0.003(1+z)$ (or $10h^{-1}$ Mpc). This scenario then resembles quite closely a purely spectroscopic survey (Asorey et al. 2012).

We again study two populations, one corresponding to the main sample with bias $b = 1$ and another to the LRG sample with $b = 2$, both with a very good photometric accuracy of $\sigma_z/(1+z) = 0.003$. We consider a set of 21 narrow redshift bins of width $\Delta z = 0.003(1+z)$ concentrated in $0.94 < z < 1.06$ (hence we are only looking at a portion of the survey redshift range).

The error on γ are given in Table 4.2, for both the new narrow-band and the broad-band samples discussed previously. For a single population, this table shows that a factor of ~ 10 better σ_z yields a factor of ~ 10 gain in constraining power. The improvent in γ seems to increase linear with the improvement in σ_z. After combining the two populations we see that the errors in γ for the broad-band case is similar if samples cover the same region of sky (Pop1 × Pop2) or different regions (Pop1 + Pop2). This is because the redshift range considered ($0.94 < z < 1.06$) is too narrow compared to σ_z and the cosmic variance cancelation can not take place. Instead, for the narrow band surveys we find a 43% improvement for the case Pop1 × Pop2 with respect to Pop1 + Pop2. For the same sky case, the final error is $\Delta\gamma \simeq 0.0163 \times \sqrt{(}5000deg^2/\text{Area})$, in such a way that even a moderate survey of $250\,\text{deg}^2$ could achieve $\Delta\gamma \sim 0.07$. In that same narrow redshift range, DES yields an error 5 times worse with 20 times better area (but note that in the case of small areas we could be limited by the ℓ_{min}, the largest scales available).

4.4 Discussion

We have studied how measurement of redshift-space distortions (RSD) in wide field photometric surveys produce constrains on the growth of structure, in the linear regime. We focused in survey specifications similar to those of the ongoing DES or PanSTARRS, that is, covering about 1/8 of sky up to $z \sim 1.4$, and targeting galaxy samples with photometric redshift accuracies of $0.03 - 0.05(1 + z)$ (and hundred of million galaxies prior to sample selection). We also show results for ongoing photometric surveys, such as PAU and J-PAS, that have a much better photometric accuracy.

First, we have found that for a single population we can reduce the errors in half by including all the cross-correlations between radial shells in the analysis. This is because one includes large scale radial information that was missed when only considering the auto-correlations of each bin. The final constraining power depends on the details of the population under consideration, in particular the bias and the photometric accuracy. Less bias gives more relative importance to RSD in the clustering amplitudes. In turn, better photo-z allows for narrower binning in the analysis and more radial information. We find that the γ constrains depend roughly linearly in both bias or σ_z. This means that for 10 times better photo-z errors, such as in PAU, we can improve by 10 the cosmological constrains.

Typically less bias implies a fainter sample, with worse photo-z, therefore these quantities compite in determining the optimal sample. Furthermore we find that optimal constrains are achieved for bin configurations such that $\Delta z \sim \sigma_z$. Although the optimal errors depend on the details of the galaxy sample and binning strategy, the gains from adding cross-correlations are very robust in front of these variations.

In order to avoid sample variance, we have also considered what happens if we combine the measurement of RSD using two different tracers. This is motivated by the idea put forward in (McDonald & Seljak 2009) for the case of spectroscopic (hence 3D) redshift surveys, where the over-sampling of (radial + transverse) modes allows a much better precision in growth rate constrains, as long as samples are in the low shot-noise limit. Combining auto and cross angular correlations in redshift bins, we find that if we assume that both tracers are independent, which corresponds to samples from different regions on the sky, the constrains on the growth of structure parameters improve a 30-50% (due to the fact that one has doubled the area). Remarkably if we consider that the populations are not independent, i.e., they trace the same field region, we find an overall improvement of $\sim 2 - 3$ with respect to single populations when constraining γ. This means that there is a large potential gain when sampling the same modes more than once.

Translating into actual constrains this implies that a DES-like photometric survey should be able to measure the growth rate of structure γ to an accuracy of $5 - 10\%$ from the combination of two populations and all the auto+cross correlations in the range $0.4 < z < 1.4$ (see Fig. 4.1). Even though these values correspond to a survey of 5000deg^2 ($f_{sky} = 0.125$) they should scale as $f_{sky}^{-1/2}$ for a different area, given our assumptions for the covariance in Eq. (4.12).

In Fig. 4.7 we have shown that constrains weaken once one of the populations enter a shot-noise dominated regime, as is typical of spectroscopic samples. However one needs to dilute over 10 times the number densities for a photometric survey, such as DES, for this to happen. Thus, as shown in Section 3.4, by improving on photo-z accuracy without much lost of completeness, a photometric sample can in fact outperform a diluted spectroscopic version with similar depth and area (see also (Gaztañaga et al. 2012)).

We focused on large angular scales where the approximation of linear and deterministic bias and linear RSD should hold (see for instance (Crocce, Cabré, & Gaztañaga 2011)). Although we set $\ell_{max} \sim 200$, much of the constraining power in our results, given the typical size of our redshift bins, comes from larger scales, $\ell \lesssim 40$. Yet, a more realistic assessment of these aspects will need to resort to numerical simulations.

Lastly, we also investigated what constrains can be placed with this method in the evolution of the growth rate of structure, $f(z) \times \sigma_8(z)$. We found that binning two DES populations into 6 bins in the range $0.4 < z < 1.4$ yields constrains on $f(z) \times \sigma_8(z)$ of $\sim 15\%$ for each bin above $z \sim 0.6$. That case corresponded to bin widths larger than the photometric errors of the samples, which may not be optimal but yield constrains almost uncorrelated between bins ($\rho_{ij} \sim -0.05$). Figure 4.9 shows instead the results from a narrower binning, $\Delta z/(1 + z) = 0.05$. This leads to better constrains, $\Delta(f\sigma_8) \sim 10\%$, at the expense of more correlation between bins, $0.2 < \rho_{ij} < 0.65$.

In addition to the DES forecast (shadowed region) we over-plot in Fig. 4.9 current constrain from spectroscopic surveys, such as 2dFGRS (Percival et al. 2004), LRG's from SDSS ((Tegmark 2006) and (Cabré & Gaztañaga 2009)), WiggleZ either from power spectrum (Blake et al. 2011) or correlation function (Contreras et al. 2013) and the recent BOSS results (Reid et al. 2012). Note that these values are not expected to improve radically in the near future. This implies that DES will be able to add quite competitive constrains in a redshift regime unexplored otherwise with spectroscopic surveys (i.e. $z \gtrsim 1$), yielding a valuable redshift leverage for understanding the nature of dark energy and cosmic acceleration through the growth of structure.

Chapter 5

Comparison with galaxy survey simulations

5.1 Motivation

In the previous chapters, we have been forecasting constraints on cosmological parameters using angular correlations. The first step consisted on figure out the optimal binning in order to recover the same constraints than when using correlations in 3D space.

Then we investigate the idea of using photometric redshifts to test growth history of structure at high redshifts, $z > 1$. We showed that if we use two tracers of dark matter, in the same field with high number density, as expected with photo-z surveys, we can reach similar constraints to low-z results from spectroscopic surveys. For that, we used all the angular and cross-correlations between redshift bins and between the two tracers.

Now, we concentrate on testing the model used in previous chapters with N-body simulations. N-body simulations include more accurate description of growth of structure, including non-linear evolution because of gravitational collapse. The additional effects that we include in the modeling are photometric redshifts and redshift space distortions. The combination of all of them is close to a real photometric survey.

From a dark matter lightcone of MICE simulations, diluted to follow a determined redshift distribution, we obtain a real space, redshift space, and photo-z space catalogues of an unbiased population. In addition, we use a halo catalogue to produce the same catalogues but for a biased tracer.

In the previous chapter, we have been working on the spherical harmonics space. In the linear regime, the galaxy fluctuations are gaussian and therefore, defining a covariance matrix was easier because all the non-negligible high-order momenta of the distribution of fluctuation are expressed in terms of the second-order momentum, i.e, the angular power spectra. But working on this spherical harmonic space when the survey covers a fraction of the sky is more difficult than if we work in configuration space. Therefore, in this chapter we use angular correlation functions in configuration space, $w(\theta)$, instead of the power spectra C_ℓ.

This work contained in this chapter is mainly focused on a full wide field broad-photometric surveys like DES, Pan-Starrs, LSST and the imaging component of EUCLID but also thinking on narrow-band photometric surveys like PAU-survey.

We begin describing the theoretical modeling used to estimate the angular auto- and cross-correlations. Then, we describe how the process of generating the mock catalogues in real, redshift and photo-z spaces and how we made 2D maps in redshift bins from this catalogues. In section 5.4, we describe the estimator used to measure the angular correlations, including a description of the covariance matrix. We finally show in section 5.5 the comparison between linear model and correlation measurements from the mock survey catalogues.

5.2 Theoretical modeling

We describe angular correlations at linear scales as a function of redshift and angle. The effects that we include in this description are the intrinsic clustering, redshift space distortions, galaxy bias and photometric redshift distortions.

The approach consists on projecting the (3D) spatial fluctuations (either of galaxies, dark matter particles or halos), $\delta_g(\mathbf{x}, z)$ along a given direction in the sky $\hat{\mathbf{n}}$

$$\delta(\hat{\mathbf{n}}) = \int dz\, \phi(z)\, \delta_g(\hat{\mathbf{n}}, z), \tag{5.1}$$

where ϕ is the radial selection function that contains the description of the redshift bin in which we are projecting the fluctuations.

The angular two-point correlation function $w(\theta)$ is related to the probability of finding an object at distance θ from any object of the sample, in area $d\Omega$

$$dP = \bar{n}(1 + w(\theta))d\Omega \tag{5.2}$$

The angular correlation function is obtained projecting projection the (3D) spatial correlation function $\xi(r_{12})$, (Peebles 1973; Peebles 1980), weighed by the radial selection function of each redshift bin. The angular correlation of bins i, j is

$$\begin{aligned} w_{ij}(\theta) &\equiv \langle \delta_g(\hat{\mathbf{n}})\delta_g(\hat{\mathbf{n}} + \hat{\theta})\rangle = \\ &= \int dz_1\, \phi_i(z_1) \int dz_2\, \phi_j(z_2)\, \xi_{gg}(r(z_1), r(z_2), \theta) \end{aligned} \tag{5.3}$$

where θ is the angle between directions $\hat{\mathbf{n}}$ and $\hat{\mathbf{n}}+\hat{\theta}$. This angle is related with the co-moving distances within the bin $r(z_1)$ and $r(z_2)$ and the co-moving distance between tem r_{12} by

$$r_{12}(\theta) = \left\{ r(z_1)^2 + r(z_2)^2 - 2r(z_1)r(z_2)\cos(\theta) \right\}^{1/2} \tag{5.4}$$

and $r(z)$ is the co-moving distance to redshift z given by

$$r(z) = \int_0^z \frac{1}{H(z')} dz', \tag{5.5}$$

where $H(z) = H_0\sqrt{\Omega_m(1+z)^3 + \Omega_{\rm DE}(1+z)^{3(1+w)}}$ is the Hubble parameter, following description of chapter 2. This expressions correspond to the flat ΛCDM universe, with $w = -1$.

Auto-correlations correspond to the case $i = j$, otherwise they are cross-correlations. For the same population, in the cases that we consider

$$w_{ij}(\theta) = w_{ji}(\theta) \tag{5.6}$$

Since we are interested in redshift bins and not in extended selections we can neglect the growth evolution within the bin and simply evaluate the 3-d correlation in some fiducial redshift $\bar{z}$ (e.g. the mean redshift of the bin, weighted by ϕ). We assume a *local and linear bias* relation between fluctuations in the tracer (e.g. galaxies) and matter density field, $\delta_g = b(z)\delta$. Under these assumptions Eq. (5.3) is converted to

$$w_{ij}(\theta) = \int dz_1\, g_i(z_1) \int dz_2\, g_j(z_2)\, \xi(r(z_1), r(z_2), \theta, \bar{z}) \tag{5.7}$$

where $g_i(z) \equiv b_i(z)\,\phi_i(z)$ and ξ is the matter 3-d correlation function.

Hence, in order to predict $w(\theta)$ we need a model for the spatial clustering accurate in a sufficiently large range of scales to allow the projection in Eq. (5.7), in particular when photo-z errors broadens the extent of the radial distribution

In what follows we discuss how to include photo-z effects and the model for spatial clustering in real and redshift space that we will use throughout this paper.

5.2.1 Photo-z and radial selection functions

As in previous chapters, the characteristics of the redshift binning are included in radial selection functions $\phi(z)$.

The radial selection function $\phi(z)$ is the probability to include a galaxy or a particle in the redshift bin considered. In an spectroscopic survey, when the selection of objects is done according to their true redshifts, then ϕ is equal galaxy redshift distribution dN_g/dz times a window function $W(z)$ that encodes the selection characteristics like redshift cuts or the narrower redshift bins in which may divide the sample,

$$\phi(z) = \frac{dN_g}{dz} W(z). \tag{5.8}$$

When the survey is photometric, the uncertainties in the true redshift positions from the photometric redshift estimates affects the radial functions. In this case, we must incorporate in the analysis the probability $P(z|z_p)$ for the true redshift to be z when the photometric one is z_p. The selection function is described by (Budavari et al. 2003),

$$\phi(z) = \frac{dN_g}{dz} \int dz_p P(z|z_p) W(z_p), \tag{5.9}$$

where $W(z_p)$ is the photometric redshift window function.

We consider always in this chapter top hat window functions in the samples that we are considering. In the case in which we considered true redshifts, we use equation (5.8) with a top-hat window in true redshifts.

For photometric redshifts, we use a top-hat in photo-z space and therefore we used the radial selections given by eq. (5.9). We assume that the photometric estimates are gaussianly distributed around the true redshift (e.g. (Ma 2006)) because it is the same assumption that was used to create the catalogues when including photometric distortions in the redshift. In this case

$$\phi_i(z) \propto \frac{dN_g}{dz} \left(\mathrm{erf}\left[\frac{z_{p,max} - z}{\sqrt{2}\sigma_z} \right] - \mathrm{erf}\left[\frac{z_{p,min} - z}{\sqrt{2}\sigma_z} \right] \right) \tag{5.10}$$

Finally, ϕ should be normalized to unity within the redshift range of interest, like each redshift bin.

5.2.2 Spatial clustering and redshift evolution

Here, we describe the modeling used for the (3D) spatial clustering and that is projected in redshift bins. We also account for the effect of linear space distortions, including the Kaiser effect in the modeling, and the evolution of clustering with redshift, due to the growth of structure.

First of all, the two point spatial correlation function is given by

$$\xi(r) = \int dk \frac{k^2}{2\pi^2} P(k) \frac{\sin kr}{kr} \tag{5.11}$$

where $P(k)$ is the linear matter power spectrum at redshift $z = 0$. We use `CAMB`. (Lewis, Challinor & Lasenby 2000) to compute $P(k)$.

The redshift evolution of the spatial correlation function is given by the growth factor $D(z)$, defined in equation (2.43). Then,

$$\xi(r, z) = D^2(z)\xi(r) \tag{5.12}$$

In the case in which we do not include redshift-space distortions then

$$w_{ij}(\theta) = \int dz_1\, \phi_i(z_1) \int dz_2\, \phi_j(z_2)\, \xi(r_{12}, \bar{z}) \tag{5.13}$$

where r_{12} is given by eq. (5.4).

The last effect that is included corresponds to redshift space distortions. As shown in 2.7.1, the positions of galaxies in redshift space differ from the positions in real space, given by the Hubble law, because of the radial peculiar velocity of the galaxies. (Kaiser 1987). At large scales, the coherent infall of galaxies into large overdensities, such as clusters, make their observed radial separation smaller, squashing the structure along the line-of-sight and boosting the amplitude of the 3-d two point correlation. In this way for separations along the line of sight $\pi \lesssim 40\,h^{-1}$ Mpc the correlation (or number of pairs) increases dramatically, while for larger separations the correlation becomes negative in such a way that the total number of pairs along the l.o.s is preserved. This implies that, by dividing the data in redshift bins, one is discarding the leverage of large radial separations effectively increasing the (angular) correlation within the bin, see (Nock, Percival,& Ross 2010; Crocce, Cabré, & Gaztañaga 2011; Ross et al. 2011)

The linear redshift distortions discussed in chapter 2, namely the Kaiser effect, can be described in an alternative way in 3D configuration space, (Hamilton 1992), assuming the plane-parallel approximation. We incorporate it into our modeling of the angular correlation function where we express the 3D two point correlation function with respect to the separations along the line-of-sight, π and separations transverse to l.o.s, σ where we change the variables doing $\xi(r_1, r_2) = \xi(\sigma, \pi)$ in Eq. (5.3). It is given by

$$\xi(\sigma,\pi) = \xi_0(s)P_0(\mu) + \xi_2(s)P_2(\mu) + \xi_4(s)P_4(\mu), \tag{5.14}$$

where ξ_ℓ are the multi-poles of the correlation function in terms of Legendre polynomials P_ℓ,

$$\xi_\ell(s) = \frac{2\ell+1}{2}\int_{-1}^{+1} \xi(\pi,\sigma)P_\ell(\mu)d\mu, \tag{5.15}$$

with $s = \sqrt{\sigma^2+\pi^2}$ being the separation between galaxies and μ is the cosine angle with the l.o.s. For the Kaiser model one has,

$$\begin{aligned}
\xi_0(s) &= b^2\left(1+\frac{2\beta}{3}+\frac{\beta^2}{5}\right)\xi(s) && (5.16)\\
\xi_2(s) &= b^2\left(\frac{4\beta}{3}+\frac{4\beta^2}{7}\right)\left[\xi(s)-\bar{\xi(s)}\right] && (5.17)\\
\xi_4(s) &= b^2\frac{8\beta^2}{35}\left[\xi(s)+\frac{5}{2}\bar{\xi}(s)-\frac{7}{2}\bar{\bar{\xi}}(s)\right] && (5.18)
\end{aligned}$$

where b is the bias of the sample (here we assumed a linear and local bias), and $\beta = f/b$ is a different way of writing the linear growth rate factor and

$$\begin{aligned}
\bar{\xi(r)} &= \frac{3}{r^3}\int_0^r \xi(r')r'^2dr', && (5.19)\\
\bar{\bar{\xi(r)}} &= \frac{5}{r^5}\int_0^r \xi(r')r'^4dr'. && (5.20)
\end{aligned}$$

where $\pi = r_2 - r_1$ and $\sigma^2 = 2r_1r_2(1 - \cos\theta)$ (to yield $s = r_{12}$) are the pair-separation along and transverse to the line-of-sight, $\mu = \pi/s$ and P_ℓ are the Legendre polynomials. The double integrals in Eq. (5.3) are still performed in the r_1, r_2, variables leaving the evaluation of the radial selection functions unchanged. We evaluate β at the mean of the mean redshift of used bins ij.

5.3 N-body simulations and mock catalogues

Our goal is to check the theoretical modeling described in section 5.2 with mock galaxy samples created from the output of N-body simulations.

The mock samples that we consider here are an unbiased population and a biased tracer of density field. This samples are studied in real and redshift space and also in photo-z space, in order to test the theoretical description of the model that we are using throughout the chapter.

In this case, the survey mock catalogues have been produced using a large N-body simulation, provided by the MareNostrum Institut de Ciències de l'Espai (MICE) collaboration `http://www.ice.cat/mice` in order to produce mock catalogues. In this case, the catalogues correspond to a dark matter particles catalogue in the lightcone and a catalogue of halos with masses greater than $10^{12}\,h^{-1}\,\mathrm{M}_\odot$. The dark matter catalogue mimics an unbiased population with $b_g = 1$ while the halos would correspond to a catalogue of bright galaxies, such as Luminous Red Galaxies, with high galaxy bias.

The parent simulation, `MICE7680`, is a very large simulation that contains 2048^3 dark matter particles in comoving volume of $L_{\mathrm{box}} = 7680\,h^{-1}\,\mathrm{Mpc}$. The cosmological model of the simulations is a flat ΛCDM with parameters $\Omega_m = 0.25$, $\Omega_\Lambda = 0.75$, $\Omega_b = 0.044$ and $h = 0.7$, $n_s = 0.95$ and $\sigma_8(z = 0) = 0.8$. The simulation was performed using the `Gadget-2` code (Springel 2005), setting initial conditions at $z = 150$, following Zeldovich dynamics. Particle mass was $3.65 \times 10^{12}\,h^{-1}\,\mathrm{M}_\odot$. For more detailed aspects, review (Fosalba et al. 2008; Crocce et al. 2009).

The dark matter catalogue is based on a lightcone output of the simulation. The distribution of particles with comoving distance is diluted in order to match the galaxy distribution of galaxies.

Without loss of generality we next assumed a survey covering a continuous $5000\,\mathrm{deg}^2$ of sky (i.e. a sky fraction $f_{\mathrm{sky}} = 1/8$), and redshift coverage in the range $0.2 < z < 1.4$. In broad terms, this matches the specifications for DES.

The initial lightcone input contains the right ascension and declination of each galaxies and then the radial information. The radial information given by the comoving position of the galaxy in the lightcone, the displacement due by the peculiar velocity of each galaxy and the radial displacement due to a photometric redshift of $\sigma_z = 0.0035(1 + z)$. This displacement can be re-scaled to consider different gaussian distributed photometric errors

In order to have a clearer understanding of the different components of the model we built ensembles of mocks in increasing "layers of reality". We first selected dark-matter particles directly from real space assuming a radial distribution as expected in DES. We also repeated this exercise with halo catalogues, that we use as biased tracers. Next we moved particles to redshift space before doing the selection. Alternatively, we imposed a random radial uncertainty in the position of each particle before selection to mimic photometric error. Finally we imposed the radial distribution in addition to redshift distortions and photometric error to build mocks which are closest to a real survey.

In what follows we give a more detailed discussion of the different cases considered, giving a descriptive summary of mock sample used in this chapter.

5.3.1 Real Space catalogues

This catalogues are made from the lightcone, considering only the distances corresponding to the sli distance of the galaxy to the observer. We select impose a redshift cut in real (or configuration) space that corresponds to the range $0.2 < z < 1.4$. All the galaxies are restricted to have right ascension and declination in $0^\circ - 90^\circ$, therefore covering 1/8 of sky, similar to the expected full DES area. The dark matter lightcone contains ~ 51797427 unbiased mock galaxies in this range while the number of massive halos considered within our selection thresholds is ~ 46125386.

Then, from this catalogues, we extract all the particles within spherical coronas, each one corresponding to a redshift bin width of $\Delta z = 0.15$. In table 5.1 we show the characterization of the bin configuration. This includes the mean redshift of the bin, the width of the bin in redshift and comoving space and the angular number density of galaxies in each redshift bin.

Then, we divide the survey range in 8 radial shells, corresponding to redshift bins of $\Delta z = 0.15$ and we stack the angular positions of all the galaxies that are inside each bin. The bin configuration is described in table 5.1. The comoving widths of the radial shells range from $228\,h^{-1}$ Mpc to $400\,h^{-1}$ Mpc. Despite the fact that we assume that we know perfectly the redshift, we are using a binning that is usually considered in a broad-band photometric survey. This does not mean that this is the optimal bind width, as was shown in previous chapters.

The radial distribution of the sample was diluted with respect to the comoving output density evolution, that scales with r^2, using a redshift distribution given by a power-law and an exponential term

$$dN/dz \propto (z/0.702)^{1.083} \exp\left[-(z/0.702)^{2.628}\right], \tag{5.21}$$

The actual measurement of the distribution of galaxies in the dark matter lightcone with redshift in real space is shown in figure 5.1 The selection

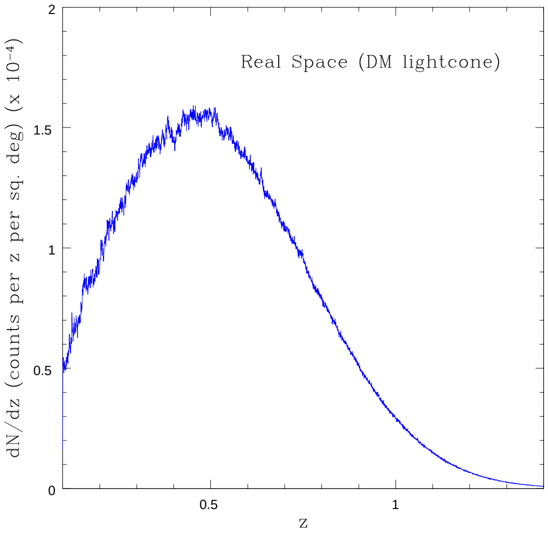

Figure 5.1: This figure shows the redshift distribution of galaxies in real space for the dark matter lightcone. The binning configuration that we use to distribute galaxies according with the redshift corresponds to eight top-hat bins from in the range $0.2 < z < 1.4$. There are no galaxies below $z = 0.1$. for galaxy selection

$\bar{z}$	Δz	$\bar{r}(h^{-1}\,\mathrm{Mpc})$	$\Delta r(h^{-1}\,\mathrm{Mpc})$	$\bar{n}$
0.275	0.15	779.8	399.58	0.48
0.425	0.15	1164.9	370.75	0.63
0.575	0.15	1521.4	342.51	0.64
0.725	0.15	1850.3	315.67	0.50
0.875	0.15	2153.2	290.69	0.31
1.025	0.15	2432.2	267.68	0.15
1.175	0.15	2689.3	246.97	0.055
1.325	0.15	2926.6	228.18	0.015

Table 5.1: *Bin configuration of unbiased sample in real space* Each bin subtends 1/8 of sky at a radial comoving distance and width as listed in the top panel. All mocks corresponds to dark-matter particles (except real space halo mocks) with a radial distribution given in Eq. (5.21). The mean distance $\bar{r}$ and width Δr are in h^{-1} Mpc. The surface density $\bar{n}$ in particles per square arc-min (and for a given bin is similar for real, redshift and photo-z space).

functions shown in fig. (5.1) were measured from the lightcone, stacking particles in narrow redshift shells of $dz = 0.003$

5.3.2 Real Space Mocks for biased tracers

We also consider the angular clustering of biased tracers as a complementary sample to the unbiased sample, in order to study the effect of biasing in the angular clustering.

Biased tracers catalogue is built starting from halo catalogues from the MICE simulation. This halos catalogues, (Crocce et al. 2009) were created according to a friends of friends (FoF), (Davis et al. 1985) algorithm. This algorithm identifies all the neighborhoods of a particle within a linking length b_{FoF}, which units of the mean interparticle distance in each simulation. For the MICE snapshots, the linking length was set to $b_{FoF} = 0.2$. We are using a $3072\,h^{-1}$ Mpc box with 2048^3 particles. Therefore, the linking lenght is $0.2 \cdot 2048/3072 \sim 0.13\,h^{-1}$ Mpc.

From one halo catalogue created using the lightcone output, with 5 or more particles per halo the catalogue is created selecting halos with masses greater than $10^12\,h^{-1}\,\mathrm{M}_{\odot}$ in a volume limited sample. The redshift range is $0 < z < 1.4$ We consider this bright halos as halos hosting LRG galaxies and therefore as biased tracers because they have the same clustering amplitude and abundance of real LRG galaxies (Cabré & Gaztañaga 2009).

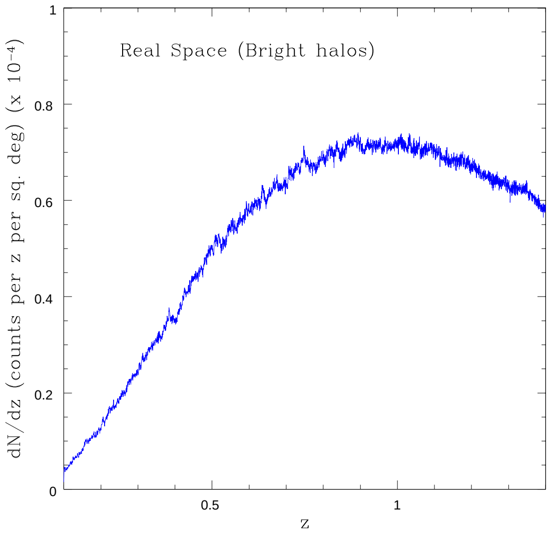

Figure 5.2: Redshift evolution of the number density of halos in the catalogue. There are not halos for redshifts greater than $z = 1.4$. This redshift distribution is given by the combination of radial evolution of comoving density and the jacobean, $H(z)/c_{light}$, of the change of variable r to z.

The volume limited sample of halos redshift distribution is shown in fig. 5.2, weighted by the jacobean that accounts from the transformation from comoving distances to redshifts

The bin configuration that we consider for the analysis of the biased tracer is shown in table 5.2

In order to be able to compare with theory, we have to estimate the galaxy bias. The approach followed consists on fitting a value of a linear and constant bias to each bin to each auto-correlation function in real space, using the theoretical prediction for $b = 1$ in real space $w_{ii}(b = 1)$. Then

$$w_{ii}^{Halos} = b_i^2 w_{ii}(b = 1) \tag{5.22}$$

We perform a sampling of b_i distribution using Markov Chain Monte Carlo method, in particular Metropolis-Hastings sampler tools from `CosmoMC`, (Lewis & Bridle 2002). We obtain the best fit and the standard deviation using `CosmoMC` getdist. Then we do a standard regression fit to

$$b(z) = az^2 + bz + c \tag{5.23}$$

using the previous 8 fits. We find the coefficients $a = 0.35 \pm 0.055$, $b = 0.26 \pm 0.089$, $c = 1.2 \pm 0.032$. In figure 5.3 we show the best fit values in each bin and the corresponding fit to the quadratic eq. (5.23).

$\bar{z}$	Δz	$\bar{r}(h^{-1}\,\mathrm{Mpc})$	$\Delta r(h^{-1}\,\mathrm{Mpc})$	$\sigma_r(h^{-1}\,\mathrm{Mpc})$	$\bar{n}$
0.275	0.15	779.8	399.58	170	0.038
0.425	0.15	1164.9	370.75	176	0.0036
0.575	0.15	1521.4	342.51	180	0.0035
0.725	0.15	1850.3	315.67	181	0.0032
0.875	0.15	2153.2	290.69	182	0.0031
1.025	0.15	2432.2	267.68	181	0.0028
1.175	0.15	2689.3	246.97	179	0.0026
1.325	0.15	2926.6	228.18	177	0.0023

Table 5.2: Bin configuration for the biased sample. Mean distances and bin widths in comoving space correspond to the simulation cosmology. The number density is given in number of galaxies per square arc-min.

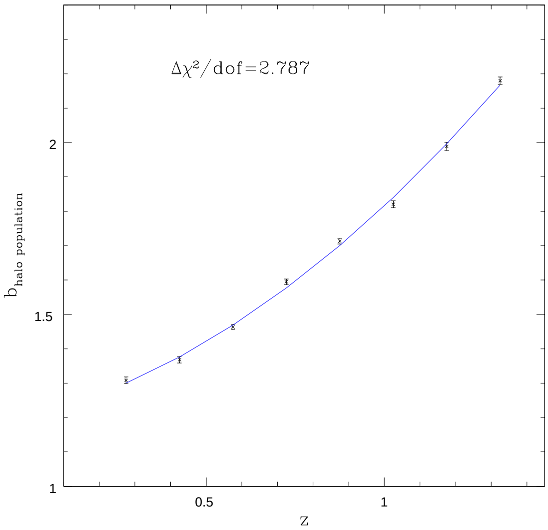

Figure 5.3: Best fit values for bias in each bin, using only auto-correlations independently. The blue line is the best fit curve $b(z) = az^2 + bz + c$ to that points

5.3.3 Redshift space catalogue

To test the accuracy of the modeling, we have included redshift distortions in a different catalogue. When doing the selection of particles from the lightcone, we add to the comoving distance the displacement caused by the peculiar velocities of the galaxies.

To understand the importance of redshift distortions, and the accuracy of the modeling, we built mocks where we impose the radial distribution in Eq. (5.21) but displace the particles to redshift space prior to the top-hat selection.

The mapping from real $\mathbf{r}$ to *Redshift Space* positions $\mathbf{s}$ is given by the transformation

$$\mathbf{s} = \mathbf{r} + v_r(1+z)/H(z)\,\hat{\mathbf{r}} \tag{5.24}$$

where H is the Hubble parameter and v_r the peculiar velocity of the object along the line of sight from the observer. Therefore given the observer at position $\mathbf{r}_0$ (the center of the spherical redshift shell) we first find the particle's projected velocity along the l.o.s. to the observer,

$$v_r = \frac{\mathbf{v}\cdot(\mathbf{r}-\mathbf{r}_0)}{|\mathbf{r}-\mathbf{r}_0|}, \tag{5.25}$$

then displace it by $\delta r = v_r(1+z)/H(z)$ along the l.o.s.,

$$\delta\mathbf{r} = \delta r\frac{(\mathbf{r}-\mathbf{r}_0)}{|\mathbf{r}-\mathbf{r}_0|} \tag{5.26}$$

5.3.4 Photo-z Space Mocks

Photo-z errors were produced setting the displacement along the line-of-sight using randoms with a gaussian probability

$$f(\delta r) = \frac{1}{\sqrt{2\pi}\sigma_r}\exp\left[-\frac{\delta r^2}{2\sigma_r^2}\right] \tag{5.27}$$

where $\sigma_r = \sigma_z c/H(z)$, and σ_z is the survey photometric uncertainty at the given z. This randoms were created using a $\sigma_z/(1+z) = 0.0035$, which is the target of narrow-band photometric surveys like PAU, (Benitez et al. 2009), but it is easy to scale them if we keep the linear evolution with redshift z. In the catalogues that we considered, the photometric redshift was set to $\sigma_z/(1+z) = 0.03$ and $\sigma_z/(1+z) = 0.05$ which correspond to an LRG and unbiased sample of a broad-band survey such as DES ((Banerji et al. 2008)). It is also the approximately photo-z precision obtained for the optical sample of LRGs selected from the SDSS imaging data (Padmanabhan et al. 2005; Padmanabhan et al. 2007; Blake et al. 2007). This is thus a very representative value for σ_z.

For the cosmology used for the running of MICE simulations, the radial distance is $\sim 140\,h^{-1}$ Mpc $\sim 180\,h^{-1}$ Mpc for $\sigma_z/(1+z) = 0.05$ while it is of the order of $\sim 108\,h^{-1}$ Mpc for the biased population ($\sigma_z/(1+z) = 0.03$)

5.3.5 Galaxy Survey Mocks

Finally we built mocks that include all the aforementioned effects: a realistic radial distribution Eq. 5.21, in the case of unbiased tracers, redshift distortions and photometric redshift with uncertainty $\sigma_z/(1+z) = 0.05$ in the case of DM catalogues and $\sigma_z/(1+z) = 0.03$ for the biased tracer given by the bright halos. The redshift range is $0.2 < z < 1.4$ and the bin configurations for DM and halos are shown in table 5.1 and 5.2, respectively. Therefore, these are the closest to an actual photo-z survey such as DES or PanStarrs and expected LSST.

Before moving on we want to stress that our mocks are obtained from a *lightcone output* of an N-body simulation, then all correlations induced by non-linear gravitational evolution as well as projection effects, partial sky coverage and realistic radial selection function. We have added the linear RSD effects and gaussian photo-z distortions . Because we are using a *light-cone outputs* they include evolutionary effects of the sample within the redshift bin. Therefore, despite the fact that light-cone effects are negligible in front of photo-z and RSD for the narrow bins under consideration we include the growth evolution within the bin. To leading order, light-cone effects will introduce a *linear* evolution, which can be estimated from Eq. (5.3) by weighting the selection by the corresponding linear growth (i.e. defined with respect to the mean redshfit), given by the combination of $D(z, \bar{z})\, b(z)\phi(z)$.

5.3.6 Creating pixel maps

In order to measure the correlations we adopt the pixel based method. We use the standard widely used `Healpix`, (Górski et al. 1999; Górski et al. 2005) in order to pixelize the galaxy catalogue in each bin. Therefore, the number of healpix maps that we create is given by the number of bins N_z. Then when computing angular auto-correlations, we look for the correlations between galaxies in pixels of one maps with the rest of the pixels of the same redshift bin. In the case of cross-correlations, then we use the two pixel maps corresponding to each of the bins that we are cross-correlating.

The resolution of the pixels that we consider, is given by the healpix N_{side}. In our case, we use $N_{side} = 1024$, which corresponds to a pixel resolution of $\theta_{pix} = 3.44'$. For the full sky, the number of pixels is given by $n_{pix} = 12N_{side}^2 = 12582912$. This is a huge amount of pixels that need a huge amount of memory.

Hence, we only store the pixels corresponding to the area of the sky that we are considering, in this case, $f_{sky} = 1/8$. Selecting the pixels with central angle within $0 - 90$ declination and right ascension, we include in each map $n_{pix}^{map} = 1571840$. The maps include the ra and dec of each map pixel, the healpix pixel id and the number of galaxies in the pixel.

In section 5.4 we explain how we use this reduced maps in order to estimate the angular auto and cross-correlations.

5.4 Measuring angular correlations from simulations

We have described the theoretical linear model that is used to predict the angular correlations of galaxies in redshift bins. We also described survey-like catalogues that can include the intrinsic clustering, the redshift distortions due to peculiar velocities of galaxies and the effect of determining the radial position of galaxies using imaging-surveys.

Angular auto and cross-correlations are estimated using the maps explained in section 5.3. Catalogues include the number of particles (either dark matter particles or massive halos) in each pixel, for one octant of the sky. This is done for each redshift bin. Then, we convert them to density contrast maps. The density contrast in pixel α, for the redshift bin z_i is given by

$$\delta_\alpha(z_i) = (n_\alpha(z_i) - \bar{n}(z_i))/\bar{n}(z_i) \tag{5.28}$$

where $n_\alpha(z_i)$ is the number of particles or halos in that pixel and redshift bin, while $\bar{n}(z_i)$ is the mean number of particles in the radial shell.

Angular correlations are a function of the angle subtended in the sphere between two points. We define a linear angular binning scheme in which the width of the bin is $\Delta\theta = 0.2$ degrees.

As density contrast maps are pixelized we use the standard estimator for pixel maps, (Barriga & Gaztañaga 2002; Eriksen et al. 2004), where

$$\hat{w}_{ij}(\theta) = \frac{1}{N_{\rm pairs}} \sum_{\alpha\beta} \delta_\alpha(z_i)\delta_\beta(z_j), \tag{5.29}$$

where N_{pair} is the number of pixel pairs at the corresponding θ-bin. The angular bin that corresponds to the angular separation between pixels α and β is given by the integer part of the ratio of with respect to the bin width.

We can trace the angle between two pixels using the dot product $\cos_{\alpha\beta} = \hat{x} \cdot \hat{y}$ of the unit vectors $\hat{x}$ and $\hat{y}$ that correspond to the positions of pixels α and β, respectively

Covariance matrix

We use the delete-one-jackknife (JK) technique, (Shao 1986; Norberg et al. 2009), to estimate the errors on the auto and cross angular correlations, (Cabré et al. 2007). It consists on dividing the density contrast map in N_{JK} equal area sub-areas and then estimating the variance between the correlations computed dropping out one of this sub-regions each time.

Therefore, we have N_{JK} estimates of the angular correlation for each of the $N_z(N_z+1)/2$ observables. We use this estimates to estimate the covariance matrix.

We have chosen to divide the octant in N_{JK} 63 regions of almost equal area. We divide the declination δ in 11 parts from 0 to 90 and then for each of this angles, we take

$$N(\delta) = \frac{\pi}{2\sqrt{A}} \cos\delta = \frac{\sqrt{\pi}\sqrt{2N_{JK}}}{2} \cos\delta \tag{5.30}$$

regions in right ascension for a given δ-row, where $A = 4\pi/8N_{JK}$ is the are of the jackknife regions in the octant. This is called igloo pixelation, (Crittenden & Turok 1998; Cabré et al. 2007)

Then, with the $\hat{w}_{ij}^{JK}(\theta)$, computed using eq. where we consider all the pixels except the ones corresponding to the dropped out term Jackknife method

$$C_{\theta_s i, \theta_l j} = \frac{N_{JK-1}}{N_{JK}} \sum_{k=1}^{N_{JK}} \Delta w_i(\theta_s) \Delta w_j(\theta_l) \tag{5.31}$$

where $\Delta w_i(\theta_s) = \hat{w}_{ij}^{JK}(\theta_s) - \hat{w}_{ij}(\theta_s)$We added in the numerator N_{JK-1}, (Tukey 1958; Miller 1974) to take into account the fact that $N_{JK}-2$ sub-regions are the same between two jackknife realizations.

5.5 Comparing theory with simulations

Here, we compare the angular auto- and cross- correlations measured from the MICE lightcone with the theoretical predictions from the modeling described in section 5.2. We have two different populations, the dark matter unbiased catalogue and the halo catalogue. For each of them, we can compare the case with redshifts, a case with redshift distortions and a case that includes all the effects we consider, redshift-space distortions and photometric redshifts.

5.5.1 Unbiased sample

First of all we show the results using the catalogue in real space, without considering either redshift distortions or photometric redshifts effects. The binning adopted in this case is disclosed in 5.1. We divided the sample eight bins with the same width in redshift space. In figure 5.1 we showed the redshift distribution of the sample of galaxies in real space.

Real Space

Here, we present the measurements of the auto-correlations and cross-correlations of the galaxies in the eight redshift bins for a sample in real space, where the

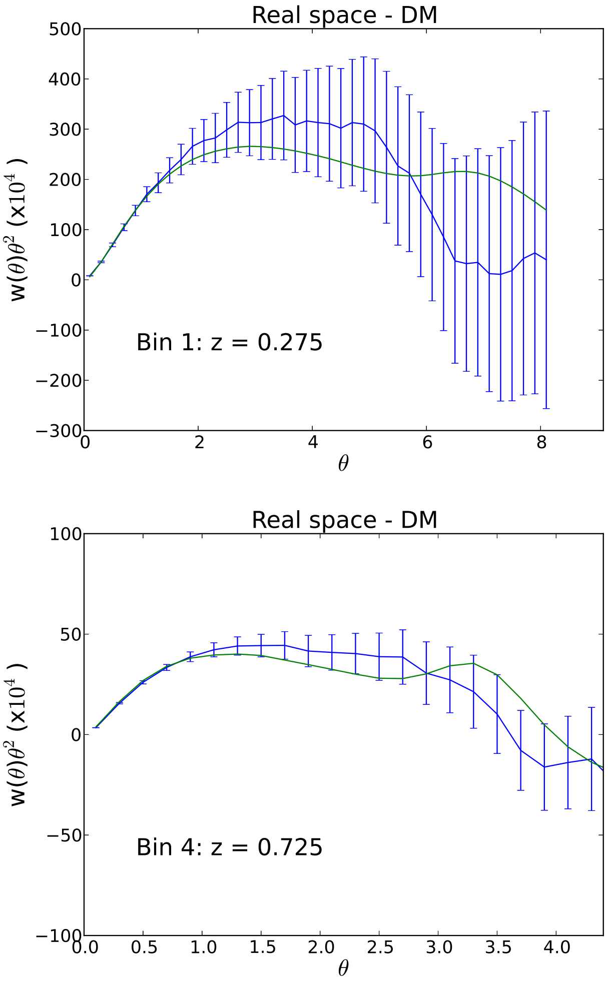

Figure 5.4: Real space auto- correlation functions of bins 1 and 4. In each plot, we show the measurement with the JK errorbars (blue) and the theoretical prediction (green) give by equation 5.13

3D-dimensional positions of the galaxies, correspond to the real positions of the galaxies, according to the Hubble flow. In this we do not consider neither redshift space distortions nor photometric redshifts effect. We set the bias to $b_g = 1$ in this case. Just notice that this section is a benchmark to look for the self-consistency of gravitational clustering cosmological model because we never observe galaxies in this space. It also help us to see in a cleaner way the effects of redshift distortions and photo-z that we will add in next sections.

First of all, we present the results for the auto-correlations in figures 5.4 and 5.5. In the top panel of figure 5.4 we present the auto-correlations of bin 1, while in the bottom panel we show the corresponding correlation of bin 4. In figure 5.5, we show the auto-correlations of the sixth (top panel) and fourth bins (bottom panel) of the configuration listed in 5.1. We observe that the prediction in real space agrees well with the measurement. We can also see how due to the growth of structure, the bin with lower-z has an angular correlation with more amplitude, which in the modeling the scaling in real space is given by the growth factor $D(z)$. Let us consider the cross- correlations between redshift bins. For separated bins, they should be compatible with zero because the 3D two point correlation function is almost zero above $150\, h^{-1}$ Mpc. Then for adjacent bins there could be a small cross-signal because of the intrinsic clustering between galaxies in both bins. In top panel of figure 5.6 we present the cross-correlations of bin 1 with bin 2 while in the bottom panel bin 3 with bin 4. In addition, top panel of fig. 5.7 shows the cross-correlations of 5-6 bins while in the bottom panel the cross-correlation is between the deepest shells. We see that the cross-correlations are consistent with the predicted cross-correlations in real space, which are close to 0.

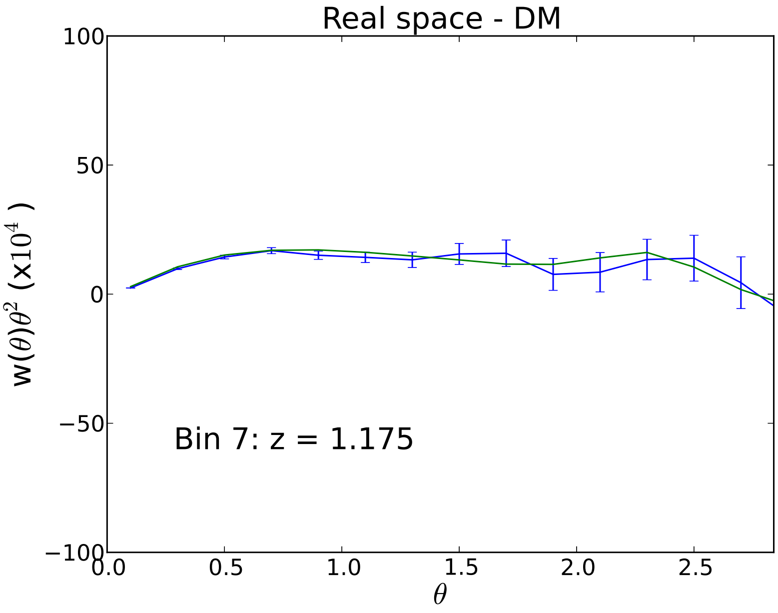

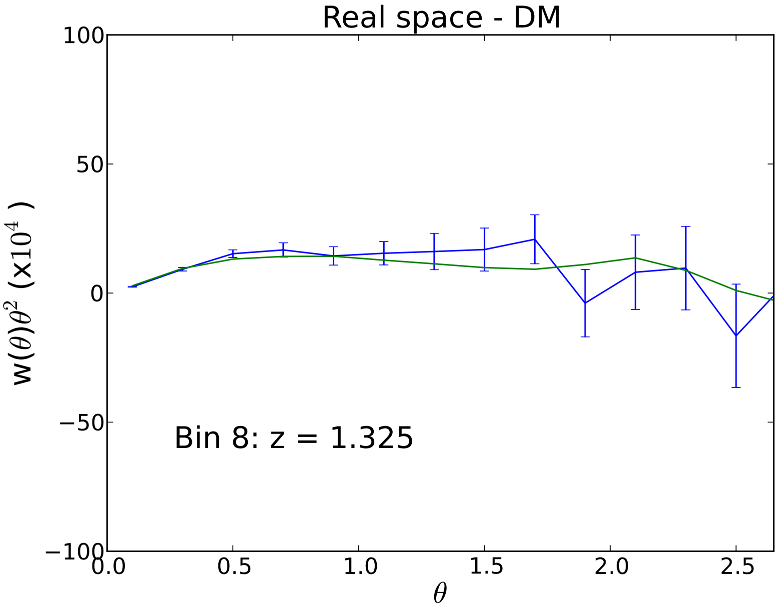

Figure 5.5: Top panel shows the dark matter auto-correlation of bin 7, while the bottom panel corresponds to the auto-correlation of bin 8

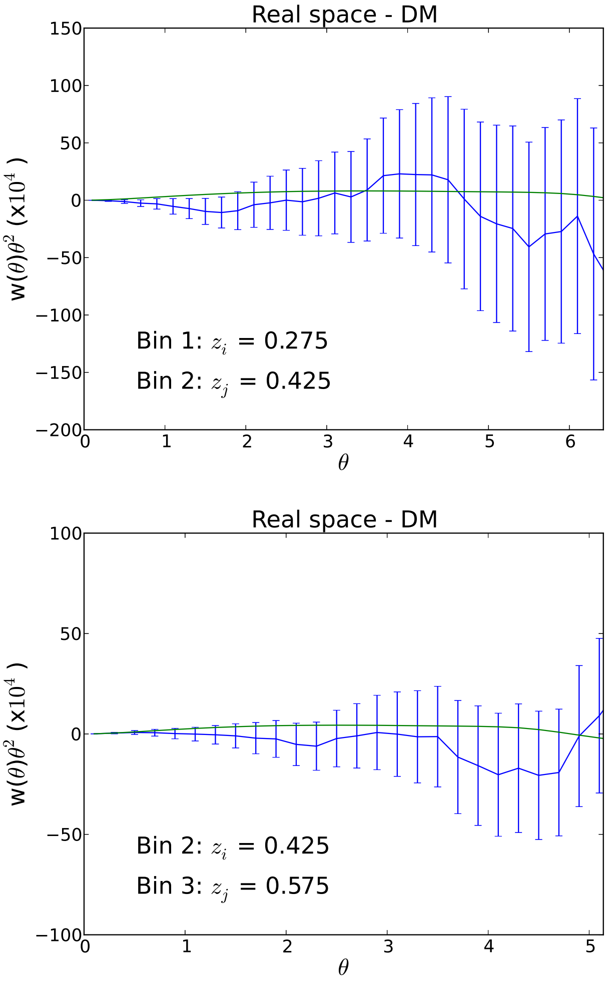

Figure 5.6: Real space cross-correaltions for the first two bins (top panel) and second and third bins (bottom panel)

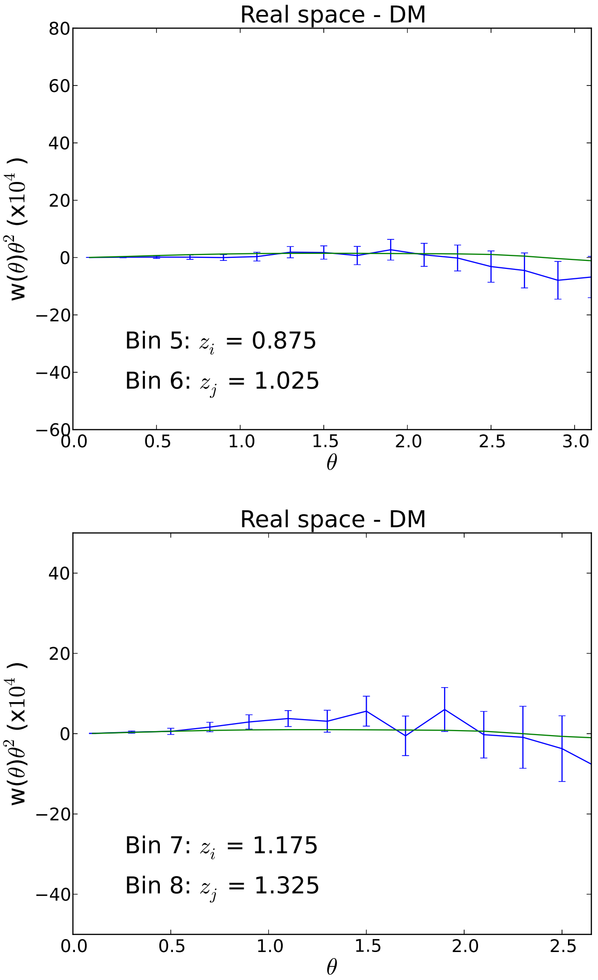

Figure 5.7: Here, we show the cross-correlation of deepest bins. Top panel corresponds to 5-6 bin correlation and bottom panel to the cross-correlation of the last two bins.

Redshift space

Now, we focus on the redshift space. This is the configuration space in spectroscopic surveys because the positions of the galaxies are distorted by the peculiar velocities. In this space, the 3D two point correlation function becomes anisotropic. The redshift distortions in 3D are usually studied using $\xi(\sigma, \pi)$, defined in eq. (5.14). In this case, we are studying the projection in top-hat bins of this 3D anisotropic correlations, as seen in eq. 5.13.

When computing angular correlations in redshift bins, the effect of redshift distortions is present because when we divide the sample in different bins we assume the same projection distance for all the bin while the real space picture on the edge of the bin differs from this redshift space projection. This makes the clusters more clustered and the voids emptier. Then, there is an overall increment in clustering when working on redshift space.

This increment is observed in the auto-correlations of figures 5.8 and 5.9 and we see that in further bins 7 and 8

We can see that the predictions agree with the measurements. Then, we show the cross- correlations of the adjacent bin to the previous results.

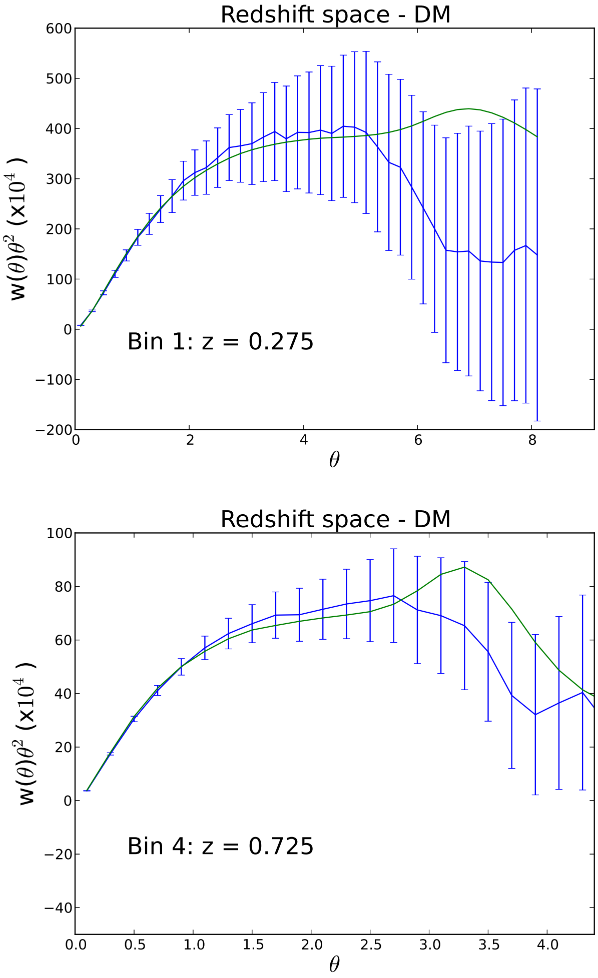

Figure 5.8: This figure corresponds to the auto-correlations of unbiased matter in redshift space. Top panel corresponds to bin 1 and bottom panel to bin 4.

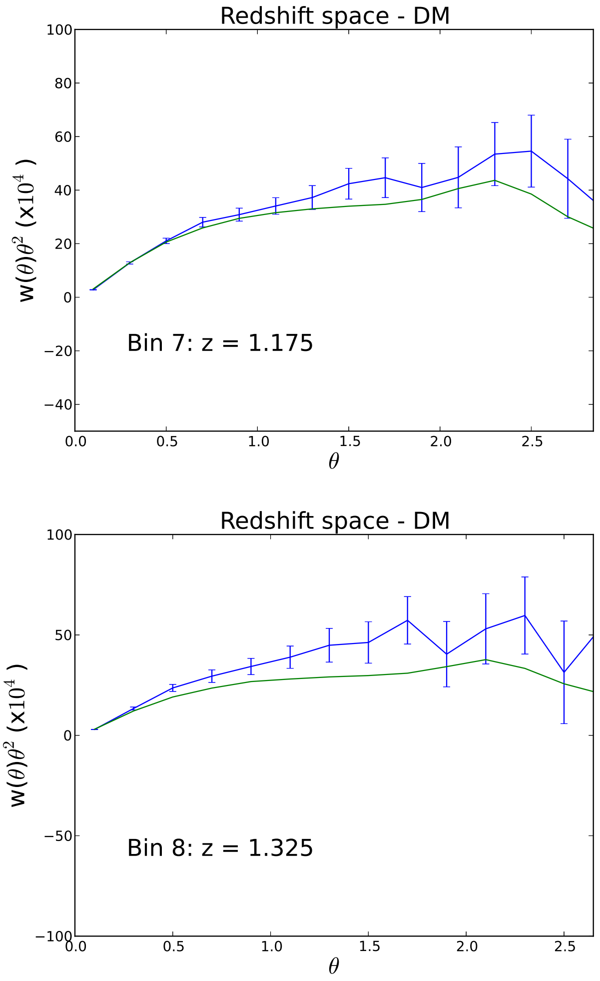

Figure 5.9: Redshift space auto-correlations of 2 deepest bins

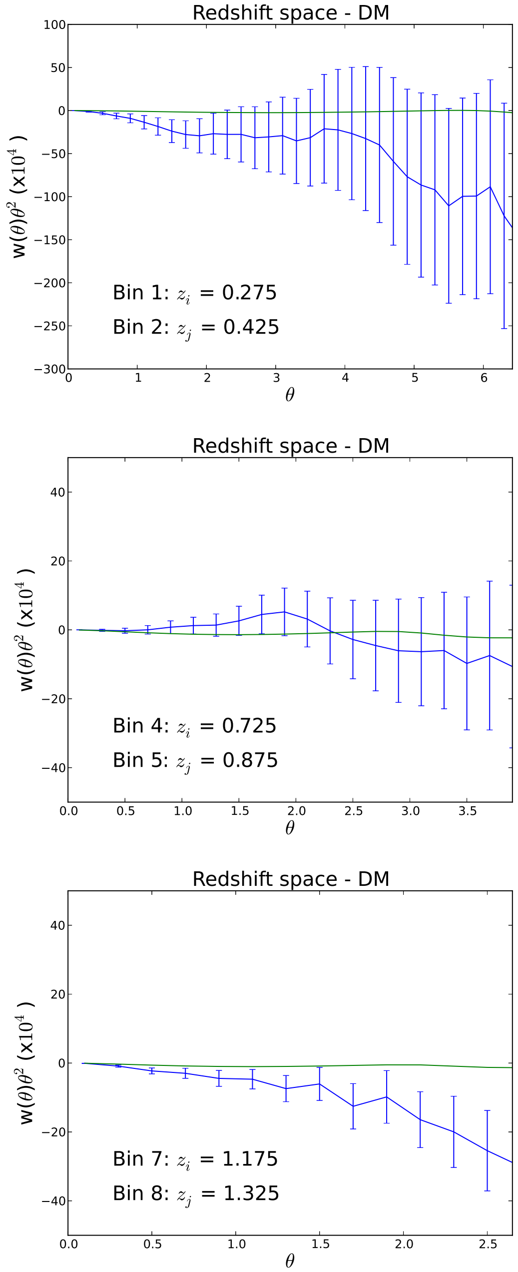

Figure 5.10: *Cross-correlations in redshift space.* Top panel shows the cross-correlations of bin 1 and 2. Medium panel presents the cross-correlation of bins 4-5 and bottom panel describes 7-8 bins cross-correlations.

Photo-z space

By photo-z space we mean the redshift space with degraded radial resolution given by photometric surveys. Photo-z randomly move galaxies in the radial direction. In this case, we have assume that this randoms follow a gaussian distribution. The effect of this distortion is a diluted clustering that when measured by angular correlations, produces a reduction in the amplitude of the auto- correlations while it magnifies the amplitude of the cross- correlations due to the overlap between the radial selections of different bins.

As redshift distortions is a radial effect, we may think that they are erased by photo-z. But, as we have mentioned in the redshift space section, the radial top-hat binning in photo-z space, differ from the true boundaries on real space. Therefore, we still have a boost on the amplitude due to redshift space distortions. Therefore, the angular correlations will show a smaller amplitude due to photometric redshifts while redshift space distortions increase the amplitude of the signal at large scales.

We can see that, compared with the redshift space results, the overall amplitude has decreased, as expected. But we can see that the redshift space distortions modeling with the gaussian modeling of the photometric redshifts works fine. We show in figure 5.11 the auto- correlations of bins 1 and 4 in the photo-z redshift space

We can see that the predictions agree with the measurements. Then, we show the cross-correlations of the adjacent bin to the previous results.

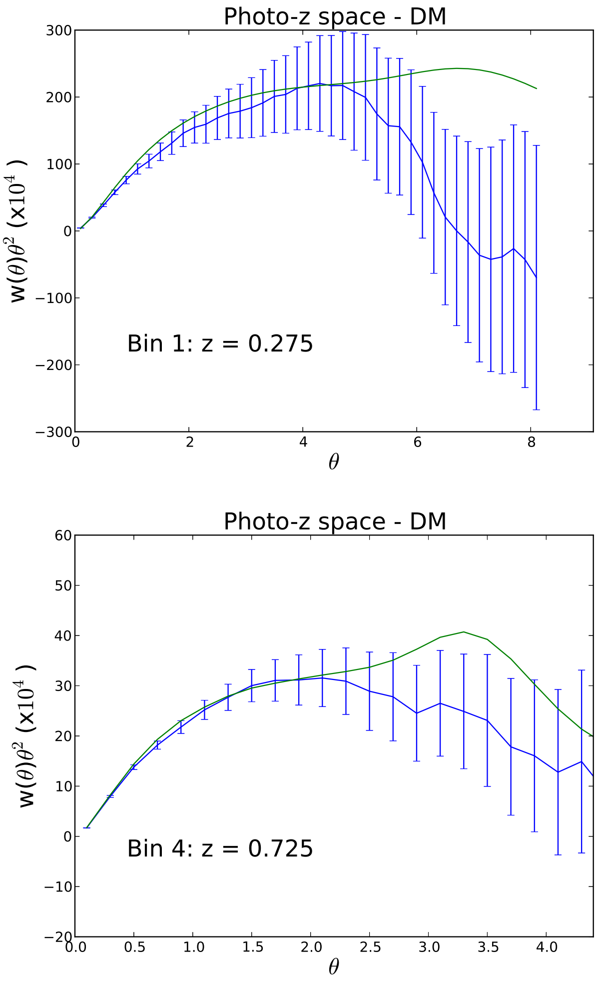

Figure 5.11: Auto-correlations in photo-z space of bin 1 (top panel) and bin 4 (bottom panel)

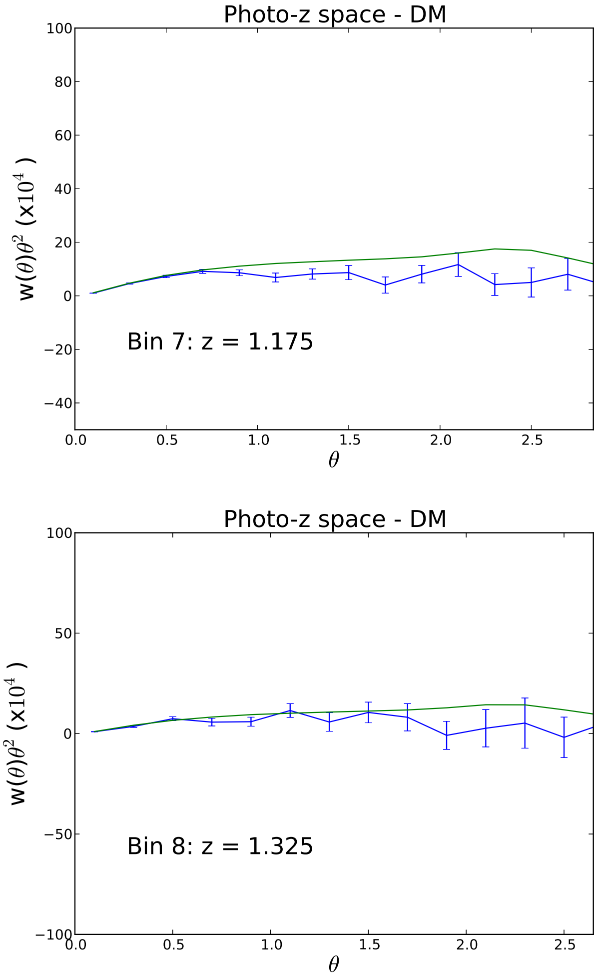

Figure 5.12: Auto- correlations of the last two bins, 7 and 8, in photo-z space.

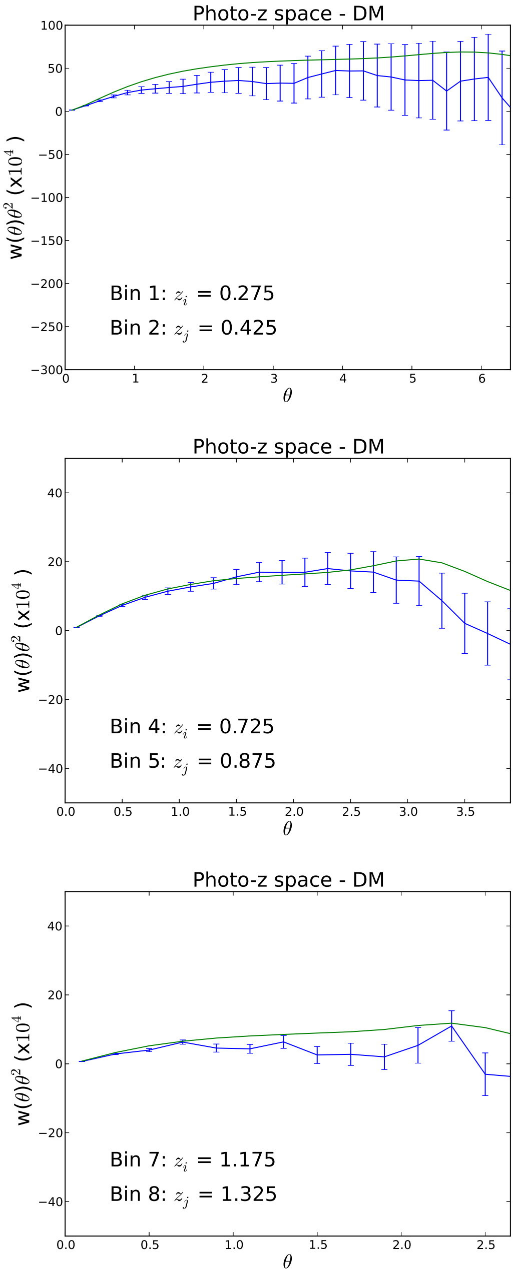

Figure 5.13: Cross-correlations in photo-z redshift space between bins 1-2 (top panel), 4-5 (medium panel) and for the last two bins (bottom panel).

5.5.2 Biased sample

Now, we compare the measurements done using the halo catalogue sample as biased tracers of matter. In general, we expect to find higher clustering because of the biasing in real space. We also expect to find a smaller effect of redshift space distortions due to the fact that the bias term is relatively higher than the anisotropic term due to the peculiar velocity gradient.

Real space

First of all, as we did for dark matter, we show the measured correlations, together with the theoretical prediction for auto-correlations of bin 1 and 3, 5.14 and we see that in further bins 4 and 8, fig. 5.15

We see that the overall amplitude is greater than the amplitude of the correlations of the unbiased sample. This is produced by the biasing. We show correlations between bin 1 and 2 in the top panel of figure 5.16 and in the bottom panel the cross-correlation between bins 2 and 3. We also show the cross-correlations of bins 5-6 and 7-8 in 5.16. In general, thanks to the fit we did for the bias, the agreement between theory and simulations is good.

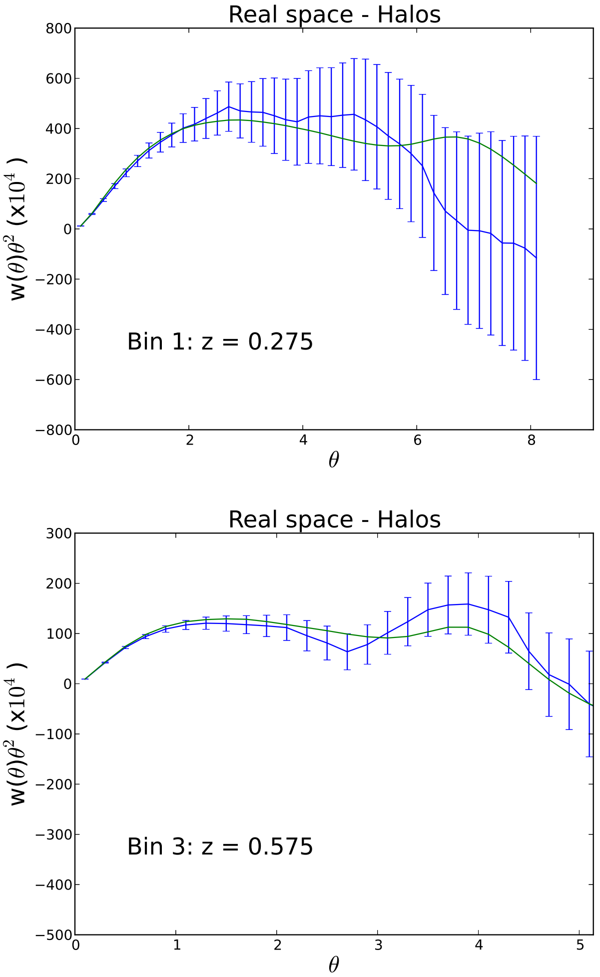

Figure 5.14: We show the auto-correlations of bins 1 (top panel) and 3 (bottom panel) for biased tracer.

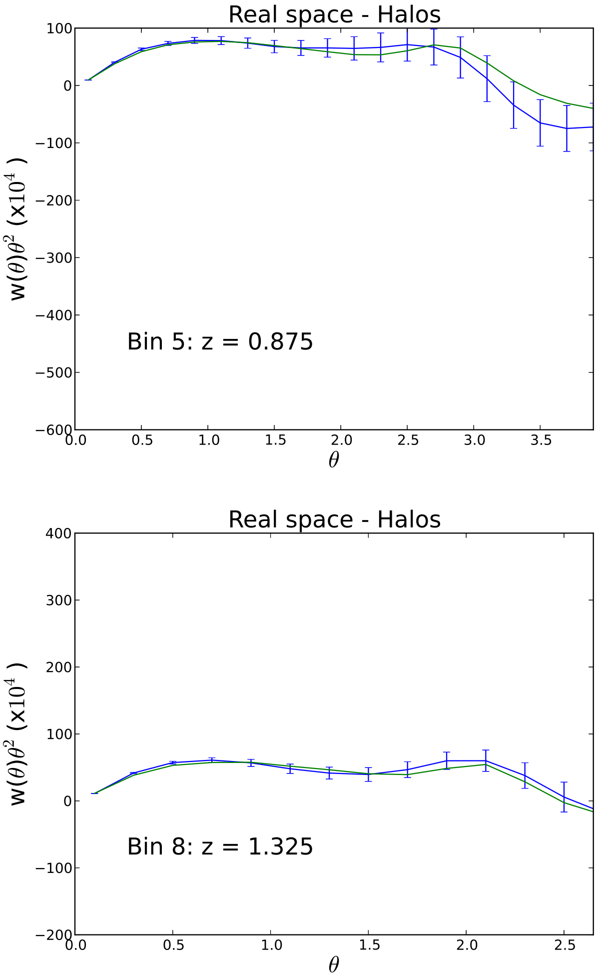

Figure 5.15: Auto-correlation of halos in real space for the fifth (top panel) and seventh bin (bottom panel).

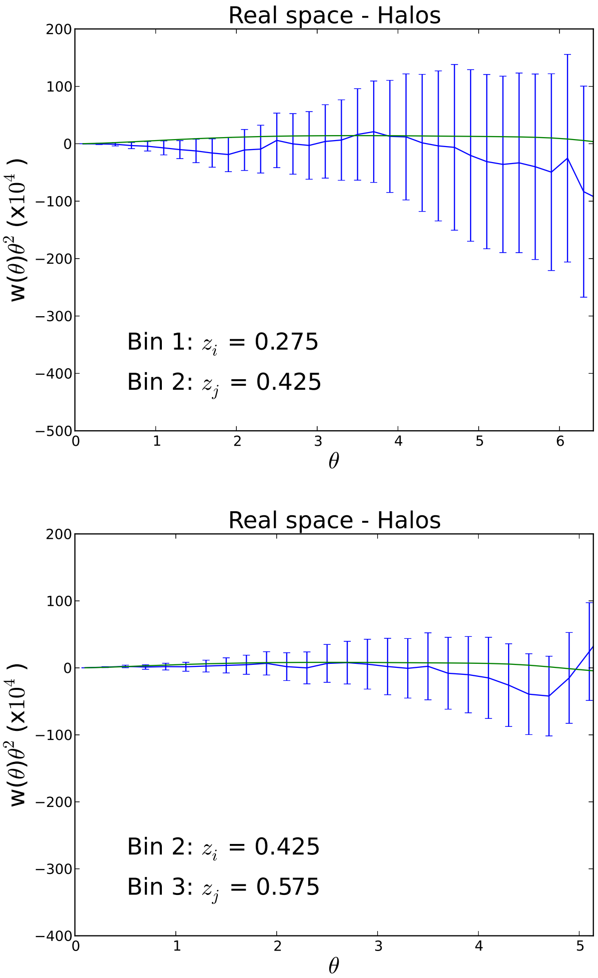

Figure 5.16: Cross-correlations of bins 1-2 and 2-3 in real space for the biased tracer.

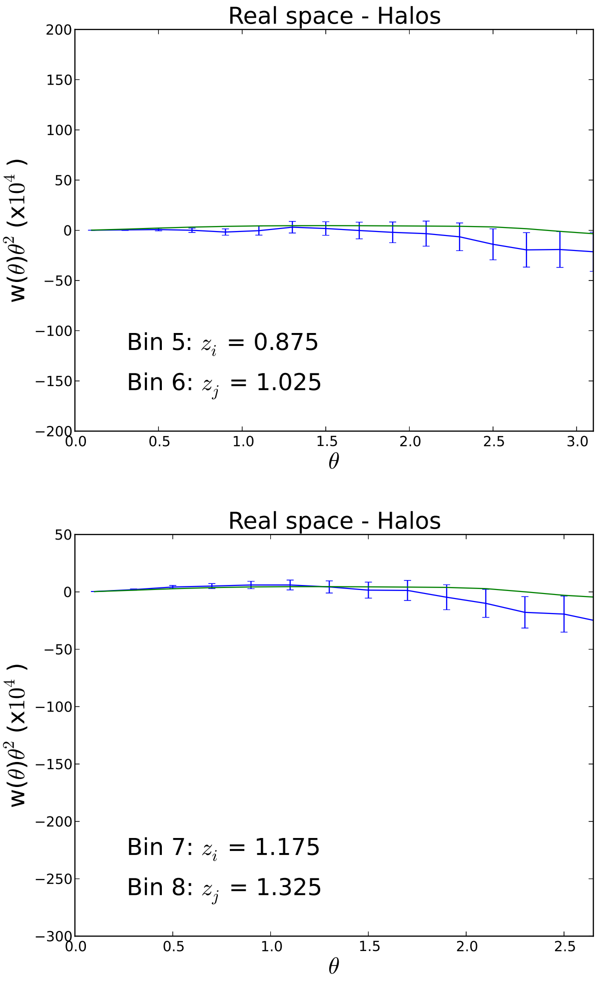

Figure 5.17: Cross-correlations of bins 5-6 and 7-8 for the biased tracers.

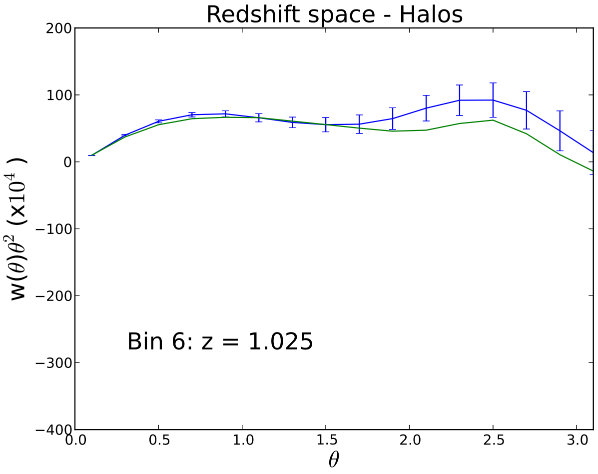

Figure 5.18: Redshift space correlation at redshift bin 5 for the biased sample

Redshift space

Now, we compare the case of a biased sample in redshift space, like an LRG sample from an spectroscopic survey. We show the auto- correlations of bins 1,2 and 6 in figures 5.19 and 5.18.

We see that the overall amplitude is greater than the amplitude of the correlations of the unbiased sample. This is produced by the biasing. The comparison of the model with the data for the auto-correlations shows that the model is a fair description of clustering. This is the same case for cross-correlations. In fig. 5.20 we show the cross-correlations of bins 1-2 and 2-3 as sample of the cross-correlations of biased galaxies in adjacent redshift bins. The clustering also agrees, within the error-bars, with theoretical prediction.

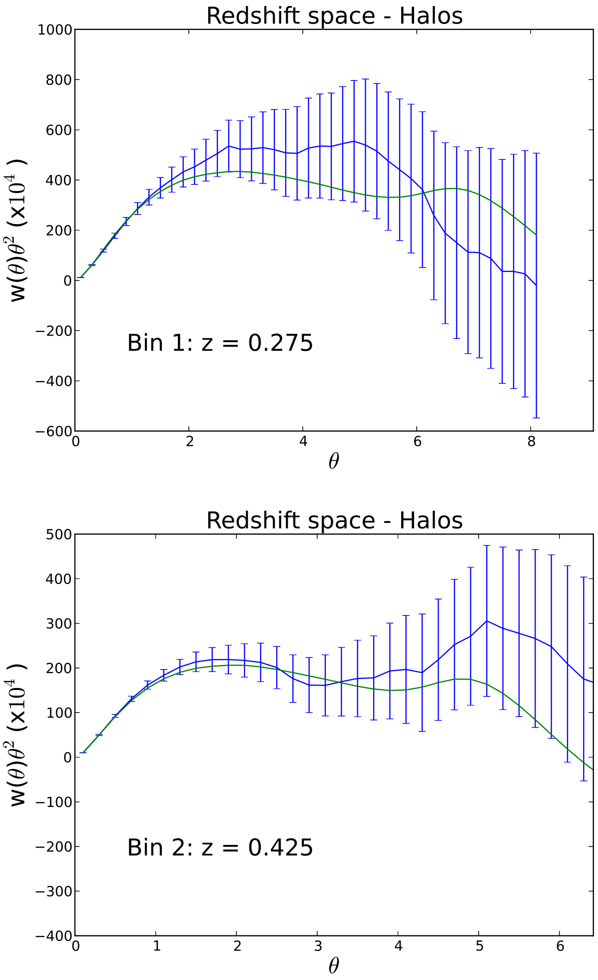

Figure 5.19: We show the redshift space halo auto-correlations of bins 1 and 3 in blue, while the theoretical prediction is shown in green. Top panel corresponds to first bin and the comparison for auto-correlation of the second bin is shown in the bottom panel.

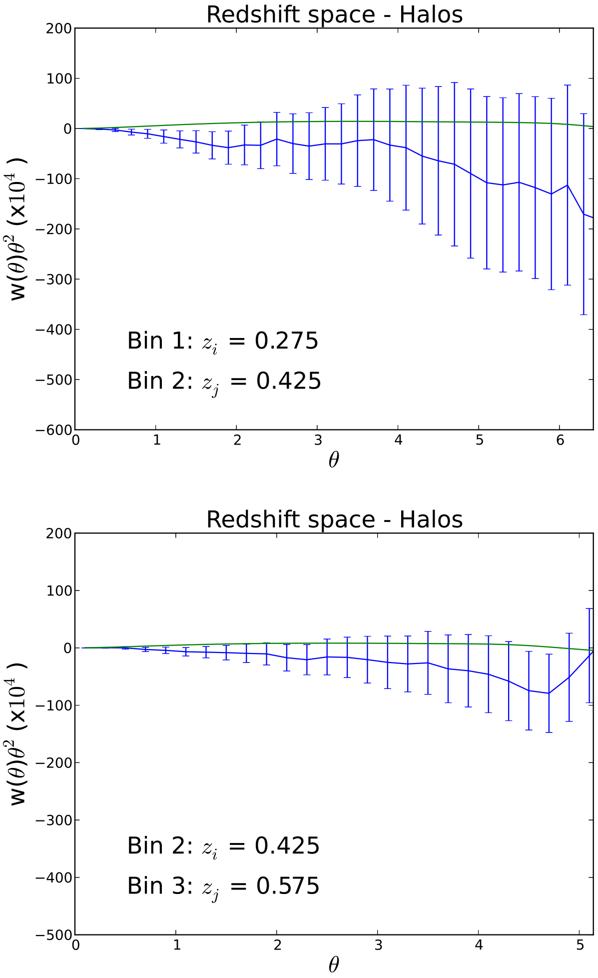

Figure 5.20: Redshift space cross-correlations of halos between bin 1 and 2 (top panel) and between bin 2 and 3 (bottom panel)

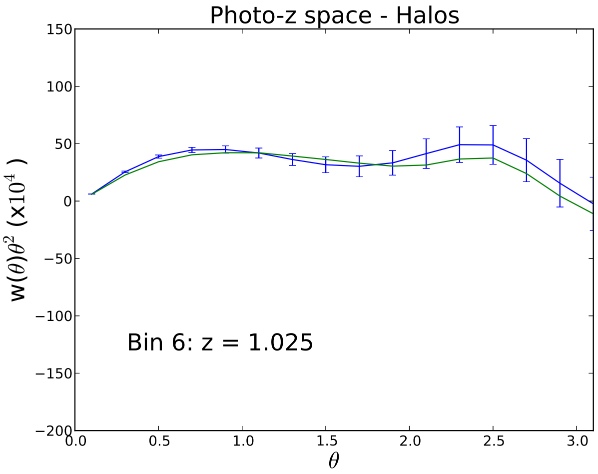

Figure 5.21: Bin 6 auto-correlation when including RSD and photo-z given by $\sigma_z/(1+z) = 0.03$

Photo-z space

Finally, we study a mock sample of biased galaxies from a photometric survey. In figures 5.22 and 5.21 we present the auto-correlations for the photometric sample of biased galaxies with the theoretical prediction, used the corresponding radial selection function and the clustering is well predicted. The global amplitude is degraded with respect to the previous case because of the photometric redshift. But the effect is not as big than for the unbiased sample because this sample has better radial accuracy and therefore the amplitude of clustering in photo-z space is greater.

In figure 5.23 we show the cross-correlations. They are bigger because of the overlap of redshift bin selection function but this expected result is well described by the theoretical modeling.

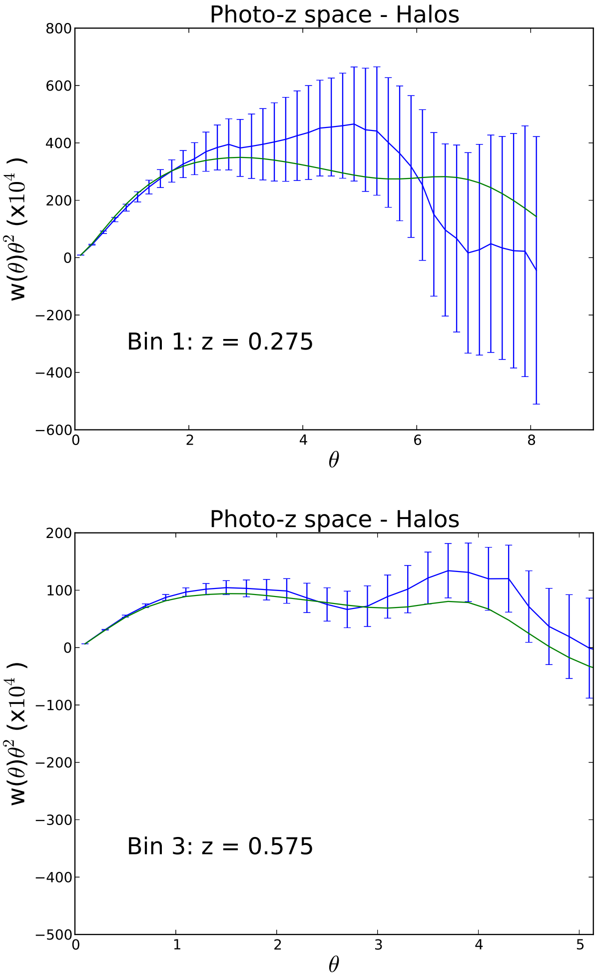

Figure 5.22: We show the auto-correlations for the most general case and the biased tracer. We selected bins 1 and 3, shown in blue, while the the theoretical modeling is in green.

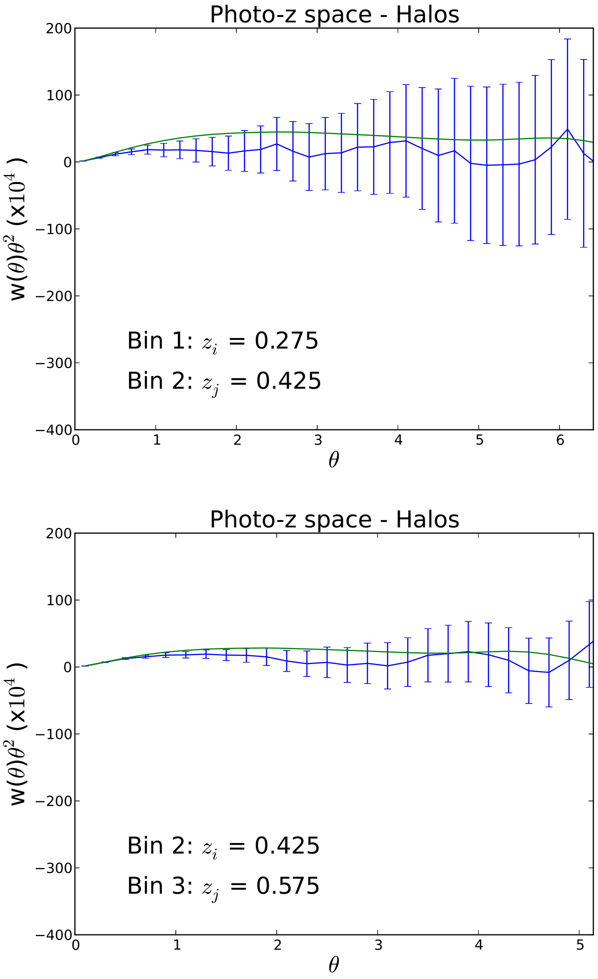

Figure 5.23: Cross-correlations between bins 1-2 (top panel) and 2-3 (bottom panel) when including the photo-z effects on top of linear peculiar velocities

5.6 Discussion

In this chapter we have tested the framework that we consider for the analysis of 3D clustering with angular auto- and cross- correlations using N-body simulations. N-body simulations allow us to study a more realistic and less optimal scenario than forecasting with models. Simulation checks are the last step before using the data because we can discriminate so many effects that are not considered in theoretical forecasts.

The modeling proposed predicts the theoretical angular clustering in a redshift bin (auto- correlations) and between different redshift bins (cross-correlations). It accounts for the intrinsic linear clustering of matter, according to the power spectrum given by an initial almost scale invariant power spectrum, with modes beyond the equality suppressed in the radiation dominated Universe, which is account solving first order Boltzmann equations, and a linear growth in the matter dominated phase. This is projected in radial shells in order to compare with the angular clustering of galaxies.

Then, we also modeled how galaxies trace the matter field by adding a multiplicative galaxy bias to the clustering power spectrum.

We have taken into account the fact that the galaxies are observed in redshift space, which distorts the apparent positions of galaxies with respect the real position. This is account using the configuration space version of the Kaiser effect (Kaiser 1987; Hamilton 1998).

Finally, we include the projection kernel in the case in which we use photometric redshifts. In this case the apparent positions of the galaxies are randomly distorted. We select the galaxies in photometric top-hat redshift bins and we convert this binning to a true redshift binning by convolving with the probability density of a true redshift to be the actual measured photometric redshift.

Then, in order to test the performance of the model we use the ΛCDM MICE N-body simulations. From a lightcone output of the simulations and from a halo catalogue we produce mock catalogues in real, redshift and photo-z space of unbiased and biased matter tracers. This has been done for eight redshift bins on a region that covers an octant of the sky, with a redshift range $0.2 < z < 1.4$. Then, we produced pixel maps of an angular resolution of3.44 arc-min and we apply an estimator based in pixel maps to estimate the angular auto- and cross- correlations.

Finally, we have compared the prediction with the estimated auto-and cross-correlations and the model agrees with the N-body simulation results, especially at the scales in which sample variance is not the main source of uncertainty. We saw that redshift distortions boost the amplitude at large scales, despite of the binning and therefore, we can use this for RSD probe to test growth history, for a given background expansion. This effect is also seen in photometric redshift space, either in auto- correlations and cross-correlations.

The fact that the cross- correlations can be described is crucial in what corresponds to this thesis because they are needed in order to recover the radial clustering information in which we call full 2D clustering analysis. A main result is the imprint of redshift distortions in the cross- correlations between adjacent bins

We have also obtained a covariance matrix from the map, using Jackkniffe technique, which is a cheap alternative way compared to building covariance matrices using hundred or thousands of survey mocks from simulations.

Finally, let us mention that this results will encourage us to use this modeling in order to do parameter estimation in the nearby future and to try to use this modeling to the full-DES data to test the model and put constraints on growth of structure, using linear redshift space distortions in photo-z space.

Chapter 6

Conclusions

Here, we summarize the main conclusions presented in this monograph. In chapter 1 we exposed the main topic and the outline of the thesis. In chapter 2 we described the assumptions that we include in our model and the notation used in the thesis. Then, in chapter 3 we compared an study of clustering in 2D space with respect to 3D space.

1. We compare the 3D predictions with the 2D predictions in a full sky spectroscopic survey with redshift range $0.45 < z < 0.65$ for different k_{max} values, defining in this way the scales included in the analysis. We predict the error on Ω_m for different surveys using as observable the linear 3D anisotropic power spectrum in different redshift bins and we find that the error on Ω_m does not change much when we change the number of redshift bins and we use the full 3D information inside each bin.

2. On the other hand, we find that the error on Ω_m decreases with the number of redshift bins used in a 2D tomographic analysis of the survey clustering. The shot noise per bin increases when increasing the number of bins. At the same time, the amplitude of the correlations in each bin, i.e., the signal, increases due to the fact that we use thinner bins. Then, the shot noise per bin is preserved. Therefore, the the error decrease when we combine of all the redshift bins.

3. For Ω_m we find that the improvement on the figure of merit is moderate when adding the cross-correlations between redshift bins to the auto-correlations. This is because there are fewer radial modes than transverse, while Ω_m information is mainly encoded in the shape of the power spectrum $P(k)$.

4. We find that 3D information is recovered when the width of the radial shells used in the 2D tomography is given by $\Delta r = c\Delta z/H(z) \simeq 0.8\lambda^{3D}_{min}$ where $\lambda^{3D}_{min} = 2\pi/k_{max}$.

5. In the redshift distortions case, the recovery of 3D information occurs when the width bin used in the 2D analysis is $\Delta r \simeq 0.6\lambda^{3D}_{min}$. We have seen that if we do not include the cross-correlations this recovery may not happen because redshift space distortions depend strongly on the comparison of the amplitude of the clustering of radial and transverse modes.

6. We consider a narrow-band photometric survey, such as PAU, covering a range $0.45 < z < 0.65$. The figure of merit on Ω_m is close to the the figure of merit for a full spectroscopic survey. The optimal bin configuration is the same as in the spectroscopic case. This is true as long as the photo-z error scale is smaller than the minimum scale, k_{max} considered in the 3D analysis.

7. Finally, for a broad-band photometric survey, like DES, the recovery does not depend strongly on the k_{max} because the radial resolution of the photometric redshifts $\sigma_r = \sigma_z c/H(z)$ is larger. In this case the optimal bin width is $\Delta_z \simeq 2\sigma_z$

Then, in chapter 4, we continued applying the cross-correlations technique to large scale structure probes, in this case to redshift space distortions using photometric surveys.

1. We see that including cross-correlations in the analysis improves the constraints on the linear growth index γ by a factor of 2, because we are adding the radial information, missed when only considering auto-correlations.

2. A population with higher bias will produce worse results because the relative importance of redshift distortions is lower than in a population with less bias. The population with better radial precision and higher densities will reach stronger constraints.

3. If we cross-correlate two populations with different bias, we are oversampling radial and transverse modes and therefore sample variance is reduced. This allows us to constrain linear growth index γ with 5-10% accuracy using an unbiased population with $\sigma_z/(1+z) = 0.05$ and a biased tracer $b = 2$ with $\sigma_z/(1+z) = 0.03$. The combination of the results from different areas of the sky is less optimal than cross-correlating populations in the same area. The impact of shot noise is not relevant for expected samples from ongoing photometric surveys.

4. We also forecast the error on the linear growth rate, $f(z)\sigma_8(z)$, and the optimal analysis includes all the cross-correlations between two populations. In this case we will be able to constrain it at high redshifts $z > 1$ with 10-15% errors per bin.

5. We also compared the performance of a narrow-band photometric survey in a redshift range $0.94 < z < 1.06$. In this case, the narrow-band survey can determine γ 20 times better than a broad-band survey in the same redshift and area range.

6. Photometric surveys will constrain the growth rate per bin at high redshifts ($z > 1$), complementing spectroscopic surveys constraints at low redshifts.

Finally, in chapter 5 we evaluated how the linear model performs compared with simulations.

1. Mock galaxy surveys were built from simulations of dark matter and halos in the light-cone, in real space, redshift space (i.e. including the effect of the peculiar velocities of the galaxies) and photometric redshift space.

2. We measured the angular auto and cross correlations of an unbiased galaxy sample, generated from a dark matter lightcone, and a biased sample, generated from the halos

3. For the unbiased sample we compared the auto- correlations and the cross- correlations with the theoretical model for angular clustering in real, redshift and photometric redshift and we have found a clear agreement between theory and the simulations.

4. Redshift distortions are clearly seen in the auto- and cross- correlations in redshift and photometric redshift space, confirming the theoretical considerations.

5. Using the auto correlations in real space we studied the clustering of a biased (halo) sample with respect to the clustering of dark matter. We find that the bias increases with redshift, but in a smooth manner

6. For the bias sample we also find good agreement of theory and simulations in real, redshift, and photometric redshift spaces. The most important conclusion is that the amplitude of clustering in this cases is higher than for the unbiased sample because of the biasing. We also notice that, as expected redshift distortions are weaker than in the unbiased case because the RSD term is relatively smaller compared with the bias term.

7. Overall we observe that theory, including the fitted evolving bias, matches the measured auto- and cross- correlations.

6.1 Future and ongoing projects

We plan to use the simulations and the theoretical model developed in chapter 5 for cosmological parameter estimation, using also the cross-correlations between different populations. One of our main interest is to extract information on the linear growth index γ and the linear growth rate $f(z)\sigma_8(z)$.

In addition, we would like to explore the extensions on the modeling to inclide the non-linear regime effects that happen at small scales where the signal to noise is typically higher.

The development of such an analysis pipeline will be of uttermost importance for the upcoming analysis of real data from DES and PAU. This will help us to understand the nature of the growth of structure.

References

Albrecht A., Steinhardt P.J., 1982, Cosmology for grand unified theories with radiatively induced symmetry breaking Nature, Phys. Rev. Let. **48**, 1220

Albrecht A., Bernstein G., Cahn R, Freedman W. L., Hewitt J., Hu W., Huth J., Kamionkowski M., Kolb E. W., Knox L., Mather J. C., Staggs S.; Suntzeff N. B., *Report of the Dark Energy Task Force*, astro-ph/0609591

Alcock C., Paczynski B., 1979, *An evolution free test for non-zero cosmological constant*, Nature **281**, 358

Annis J, Bridle S, Castander F. J., Evrard A. E., Fosalba P, Frieman J. A., Gaztañaga E., Jain B, Kravtsov A. V., Lahav Ofer, Lin Huan, Mohr J, Stebbins A., Walker T. P., Wechsler R. H., Weinberg D. H., Weller J., 2005, *Constraining Dark Energy with the Dark Energy Survey: Theoretical Challenges*, astro-ph/0510195

Asorey J., Crocce M, Gaztañaga E., Lewis A., 2012, *Recovering 3D clustering information with angular correlations* MNRAS **427**, 1891

Asorey J., Crocce M, Gaztañaga E., 2013, *Redshift-space distortions from the cross-correlation of photometric populations* arXiv:1305.0934

Banerji M., Abdalla F. B., Lahav O., Lin, H., 2008, *Photometric redshifts for the Dark Energy Survey and VISTA and implications for large-scale structure* MNRAS **386**, 1219

Bardeen J. M., 1980, *Gauge-invariant cosmological perturbations*, Phys. Rev, D22, 1882

Bardeen, J. M., Steinhardt, P. J., Turner, M. S. ,1983, *Spontaneous creation of almost scale-free density perturbations in an inflationary universe* Phys.Rev. D, **28**, 679

Bardeen J. M., Bond J. R., Kaiser, N., Szalay A. S., 1986, *The statistics of peaks of Gaussian random fields*, **304**, 15

Barriga, J., Gaztaaga, E., 2002, *The three-point function in large-scale structure - I. The weakly non-linear regime in N-body simulations*, MNRAS, **333**, 443

Benitez N., et al., 2009, *Measuring Baryon Acoustic Oscillations Along the Line of Sight with Photometric Redshifts: The PAU Survey*, ApJ, **691**, 241

Blake C, Collister A, Bridle S, Lahav O., 2007, *Cosmological baryonic and matter densities from 600000 SDSS luminous red galaxies with photometric redshifts*, MNRAS, **374**, 1527

Blake C., Brough S., Colless M., et al., 2011, *The WiggleZ Dark Energy Survey: the growth rate of cosmic structure since redshift z=0.9*, MNRAS **415**, 2876

Bonvin C., Durrer R., 2011, *What galaxy surveys really measure* Phys. Rev. D **84**, 063505

Budavári T. et al. , 2003, *Angular Clustering with Photometric Redshifts in the Sloan Digital Sky Survey: Bimodality in the Clustering Properties of Galaxies*, ApJ, **595**, 59

Cabré A., Fosalba P., Gaztañaga E., Manera M., 2007, *Error analysis in cross-correlation of sky maps: application to the Integrated Sachs-Wolfe detection* MNRAS **381**, 1347

Cabré, A., Gaztañaga, E., 2009, *Clustering of luminous red galaxies - I. Large-scale redshift-space distortions*, MNRAS **393**, 1183

Cai Y. C., Bernstein G., 2012,*Combining weak-lensing tomography and spectroscopic redshift surveys* MNRAS **422**, 1045

Casas R., et al. , 2010, *The PAU Camera*, SPIE **7735**10.1117/12.856928

Castro P. G., Heavens A. F., Kitching T. D., 2005, *Weak lensing analysis in three dimensions*, Phys. Rev. D, **72**, 023516

Challinor A., Lewis A., 2011, *Linear power spectrum of observed source number counts* Phys. Rev. D **84**, 043516

Contreras C, et al., 2013, *The WiggleZ Dark Energy Survey: measuring the cosmic growth rate with the two-point galaxy correlation function*, MNRAS **430**, 924

Crittenden, R. G., Turok N. G., 1998, *Exactly Azimuthal Pixelizations of the Sky*, astro-ph/9806374

Crocce M., Fosalba P., Castander F. J., Gaztañaga E., 2010, *Simulating the Universe with MICE: the abundance of massive clusters*, MNRAS, **403**, 1353

Crocce M., Cabré A., Gaztañaga E., 2011, *Modelling the angular correlation function and its full covariance in photometric galaxy surveys*, MNRAS **414**, 329

Crocce M., Gaztañaga E., Cabré A., Carnero A., Sánchez E., 2011, *Clustering of photometric luminous red galaxies - I. Growth of structure and baryon acoustic feature*, MNRAS **417**, 2577

Davis, M., Efstathiou G., Frenk C. S., White S. D. M., 1985, *The evolution of large-scale structure in a universe dominated by cold dark matter*, ApJ, **292**, 371

dePoy D.L., et al. , 2008, *The Dark Energy Camera (DECam)*, Proceedings of the SPIE, **7014**, id. 70140E

de la Torre S., Guzzo L., Peacock J. A., et al., 2013, *The VIMOS Public Extragalactic Redshift Survey (VIPERS). Galaxy clustering and redshift-space distortions at z=0.8 in the first data release* A&A submitted, e-print arXiv:1303.2622

Di Dio E., Montanari F., Lesgourgues J., Durrer R., *The CLASSgal code for Relativistic Cosmological Large Scale Structure*, arXiv:1307.1459

Dodelson, S., 2003, *Modern Cosmology*, Academic Press Inc., U.S., 342 p.

Eisenstein, D. J., & Hu, W. 1998, *Baryonic Features in the Matter Transfer Function* ApJ, 496, 605

Eriksen, H. K., Lilje, P. B., Banday, A. J., Grski, K. M., *Estimating N-Point Correlation Functions from Pixelized Sky Maps*, ApJS, **151**, 1

Fisher K. B., Scharf C. A., Lahav O., 1994, *A spherical harmonic approach to redshift distortion and a measurement of Omega(0) from the 1.2-Jy IRAS Redshift Survey* MNRAS **266**, 219

Fosalba P., Gaztañaga E., Castander F. J., Manera M.,2008, *The onion universe: all sky lightcone simulations in spherical shells*, MNRAS, **391**, 435

Fry J. N., Gaztañaga E., *Biasing and hierarchical statistics in large-scale structure*, ApJ, **413**, 447

Fry J. N., 1996, *The Evolution of Bias* ApJ, 461, L65

Gaztañaga E., Eriksen M., Crocce M., Castander F. J., Fosalba P., Marti P., Miquel R., Cabré A., 2012, *Cross-correlation of spectroscopic and photometric galaxy surveys: cosmology from lensing and redshift distortions* MNRAS **422**, 2904

Gil-Marín H., Wagner C., Verde L., Jimenez R., Heavens A. F., 2010,*Reducing sample variance: halo biasing, non-linearity and stochasticity*, MNRAS **407**, 772

Górski, K. M., Hivon, E., Wandelt, B. D., 1999, *Analysis issues for large CMB data sets* in Proc. MPA- ESO Conf., Evolution of Large-Scale Structure: From Re- combination to Garching, p.37. Ed. A.J.Banday, R.K.Seth, and L.A.N. da Costa (Enschede: PrintPartners Ipskamp)

Górski, K. M., Hivon, E., Banday, A. J., Wandelt, B. D., Hansen, F. K., Reinecke, M., Bartelmann, M., 2005, *HEALPix: A Framework for High-Resolution Discretization and Fast Analysis of Data Distributed on the Sphere*, ApJ, **622**, 759

Guth A., 1982, *Inflationary universe: A possible solution to the horizon and flatness problems*, Phys. Rev. D, **23**,347

Guth A. H., Pi S.-Y., *Fluctuations in the new inflationary universe*, Phys. Rev. Let., **49**, 1110

Guzzo L., et al., 2008, *A test of the nature of cosmic acceleration using galaxy redshift distortions*, Nature **541** ,451

Hamilton A. J. S., 1992, *Measuring Omega and the real correlation function from the redshift correlation function*, ApJ, **385**, L5

Hamilton A. J. S., 1998,"Linear redshift distortions: A review", in "The Evolving Universe", ed. D. Hamilton, pp. 185-275 (Kluwer Academic, 1998) [eprint arXiv: astro-ph/9708102]

Harrison E. R., 1972, *Fluctuations at the Threshold of Classical Cosmology*, Phys. Rev., **D1**, 2726

Hawken A. J., Abdalla F. B., Htsi G., Lahav O., 2012, *Lifting the degeneracy between geometric and dynamic distortions using the sound horizon from the cosmic microwave background*, MNRAS, **424**, 2

Hawking S., 1982, *The development of irregularities in a single bubble inflationary universe*, Phys. Let. B, **115**, 295

Heavens, A., 2003, *3D weak lensing*, MNRAS, **343**, 1327

Heath, D. J., 1977, *The growth of density perturbations in zero pressure Friedmann-Lemaitre universes*, MNRAS, **179**, 351

Hodapp K. W., Kaiser N., Aussel H., Burgett W., Chambers K. C., Chun M., Dombeck T., Douglas A., Hafner D., Heasley J., Hoblitt J., Hude C., Isani S., Jedicke R., Jewitt D., Laux U., Luppino G. A., Lupton R., Maberry M., Magnier E., Mannery E., Monet D., Morgan J., Onaka P., Price P., Ryan A., Siegmund W., Szapudi I., Tonry J., Wainscoat R., Waterson M., 2004, *Design of the Pan-STARRS telescopes*, Astro. Nach., **325**, 636

Jarosik et al. , 2011, *Seven-year Wilkinson Microwave Anisotropy Probe (WMAP) Observations: Sky Maps, Systematic Errors, and Basic Results*, ApJ, **192**, 14

Kaiser N., 1984, *On the spatial correlations of Abell Clusters*, ApJ, **284**, 9

Kaiser N., 1987, *Clustering in real space and in redshift space* MNRAS, **227**, 1

Kitching, T. D., Heavens, A. F. , Miller, L., 2011, *3D photometric cosmic shear* MNRAS, **413**, 2923

Kodama H., Sasaki, M., 1984, *Cosmological Perturbation Theory*, Progr. Theoret. Phys. Suppl., 78, 1

Lahav O, Lilje Per B., Primack, J. R., Rees Martin J., 1991 *Dynamical effects of the cosmological constant*, MNRAS, **251**, 128

Lange et al. , 2001, *Cosmological parameters from the first results of Boomerang*, Phys. Rev. D, **63**, 042001

Laurejis R. et al. , 2011, *Euclid Definition Study Report*, arXiv:1110.3193

Lewis A., Challinor A., Lasenby A., 2000, *Efficient Computation of Cosmic Microwave Background Anisotropies in Closed Friedmann-Robertson-Walker Models*, ApJ **538**, 473

Lewis A., Bridle S., 2002, *Cosmological parameters from CMB and other data: A Monte Carlo approach*

Liddle A. R., Lyth D. H., 2000, *Cosmological Inflation and Large-scale Structure*, Cambridge Universitary Press, Cambridge, UK, 400 p

Lifshitz E., 1946, On the gravitational stability of the expanding Universe, J. Phys.(USSR), 10, 116

Limber D. N., 1953, *The Analysis of Counts of the Extragalactic Nebulae in Terms of a Fluctuating Density Field* ApJ **117**, 134

Limber D. N., 1954, *The Analysis of Counts of the Extragalactic Nebulae in Terms of a Fluctuating Density Field II* ApJ **119**, 655

Linde A. D., 1982. *A new inflationary universe scenario: A possible solution of the horizon, flatness, homogeneity, isotropy and primordial monopole problems*, Phys. Let. B, **108**, 389

Linde A. D., 1983. *Chaotic Inflation*, Phys. Let. B, **109**, 177

Linder, E. V. 2005, *Cosmic growth history and expansion history* Phys. Rev. D **72**, 043529

LoVerde M., Afshordi N., 2008, *Extended Limber approximation*, Phys. Rev. D, **78**, 123506

LSST Dark Energy Science Collaboration, 2012, *Large Synoptic Survey Telescope: Dark Energy Science Collaboration*, arXiv:1211.0310

Ma C.-P., Bertshinger, 1995, Cosmological Perturbation Theory in the Synchronous and Conformal Newtonian Gauges, ApJ, 455, 7-25

Ma Z, Hu W, Huterer D, 2006, *Effects of Photometric Redshift Uncertainties on Weak-Lensing Tomography*, ApJ, **636**, 21

Malik A. M., Wands D., 2009, Cosmological Perturbations, Phys. Rep., 475, 1-51

McDonald P., Seljak U., 2009, *How to evade the sample variance limit on measurements of redshift-space distortions*, JCAP **0901**, 007

Miller R. G., 1974, *The jackknife-a review*, Biometrika, **61**, 1

Montanari F., Durrer R., 2012, *New method for the Alcock-Paczynski test* Phys. Rev. D **86**, 063503

Mukhanov, V. F.; Chibisov, G. V., 1981, *Quantum fluctuations and a nonsingular universe*, JETPL, **33**, 532

Mukhanov V. F., Feldman H. A., Brandenberger R. H., 1992, Theory of cosmological perturbations, Phys. Rep., 215, 203

Mukhanov V., 2005, *Physical Foundations of Cosmology, Cambridge University Press*, Cambridge, UK, 442 p

Nock K., Percival W. J., Ross A. J., 2010, *The effect of redshift-space distortions on projected two-point clustering measurements* MNRAS **407**, 520

Norberg, P., Baugh, C. M., Gaztaaga, E., Croton, D. J.,*Statistical analysis of galaxy surveys - I. Robust error estimation for two-point clustering statistics*, MNRAS, **396**, 19

Okumura T., Matsubara T., Eisenstein D. J., Kayo I., Hikage C., Szalay A. S., Schneider D.P., 2008,*Large-Scale Anisotropic Correlation Function of SDSS Luminous Red Galaxies* ApJ **676**, 889

Padmanabhan N., 2005, *Calibrating photometric redshifts of luminous red galaxies*, MNRAS, **359**, 237

Padmanabhan N., et al., 2007, *The clustering of luminous red galaxies in the Sloan Digital Sky Survey imaging data* MNRAS **378**, 852

Peebles P. J. E., 1970, *Primeval Adiabatic Perturbation in an Expanding Universe*, ApJ, **162**, 815

Peebles P. J. E., 1973, *Statistical Analysis of Catalogs of Extragalactic Objects. I.*

Theory, ApJ **185**, 413

Peebles, P. J. E., 1980, *The large-scale structure of the universe*, Princeton University Press, Princeton, N.J., 435 p.

Percival W., et al., 2004, *The 2dF Galaxy Redshift Survey: spherical harmonics analysis of fluctuations in the final catalogue*, MNRAS **353**, 1201

Planck Collaboration, 2013, *Planck 2013 results. XVI. Cosmological Parameters*, arXiv:1303.5082

Planck Collaboration, 2013, *Planck 2013 results. XXII. Constraints on inflation*, arXiv:1303.5082

Reid B., et al., 2012, *The clustering of galaxies in the SDSS-III Baryon Oscillation Spectroscopic Survey: measurements of the growth of structure and expansion rate at $z = 0.57$ from anisotropic clustering*, MNRAS **426**, 2719

Reyes R, Mandelbaum Rachel, Seljak Uros, Baldauf Tobias, Gunn J. E., Lombriser Lucas, Smith R. E., *Confirmation of general relativity on large scales from weak lensing and galaxy velocities*, Nature, **464**, 256

Ross A. J., Percival W. J., Crocce M., Cabré A., Gaztañaga E., 2011, *Measuring redshift-space distortions using photometric surveys* MNRAS **415**, 2193

Seo H., Eisenstein D. J. 2003, *Probing Dark Energy with Baryonic Acoustic Oscillations from Future Large Galaxy Redshift Surveys*, Astrophys. J. 598, 720

Shao J., 1986, *Jackknife, Bootstrap and Other Resampling Methods in Regression Analysis*, Annals of Statistics, **14**, 1322.

Simon P., 2007, *How accurate is Limber's equation?*, A&A, **473**, 711

Springel V., 2005, *The cosmological simulation code GADGET-2*, MNRAS, **364**, 1105

Starobinsky A. A., 1980, *A new type of isotropic cosmological models without singularity*, Phys. Let. B., **91**, 99

Starobinsky A. A., 1982, *Dynamics of phase transition in the new inflationary universe scenario and generation of perturbations*, Phys. Let. B, **117**. 175

Taylor K., et al. , 2013, *JPCam: A 1.2Gpixel camera for the J-PAS survey*, arXiv:1301.4175

Tegmark M., 1997, *Measuring Cosmological Parameters with Galaxy Surveys* Physical Review Letters 79, 3806

Tegmark M. et al., 2006, *Cosmological constraints from the SDSS luminous red galaxies*, Phys. Rev D **74**, 123507

Thomas, S. A., Abdalla, F. B., Lahav, O. 2011,*The angular power spectra of photometric Sloan Digital Sky Survey luminous red galaxies*, MNRAS, **412**, 1669

Tukey J. W., 1958, *Bias and confidence in not quite large samples*, Ann. Math. Statist. **29** 614.

Wang L., Steindhardt P. J., *Cluster Abundance Constraints for Cosmological Models with a Time-varying, Spatially Inhomogeneous Energy Component with Negative Pressure*, ApJ, **508**, 483

Weinberg S., 1989, *The cosmological constant problem*, Rev. Mod. Phys. **61**, 1

Weinberg D. H., Mortonson, M. J., Eisenstein D. J., Hirata C.; Riess A. G., Rozo E., *Observational Probes of Cosmic Acceleration*, arXiv:1201.2434

White M., Song Y-S., Percival W. J., 2009, *Forecasting cosmological constraints from redshift surveys* MNRAS, **397**, 1348

Yoo J., Fitzpatrick A. L., Zaldarriaga M., 2009, *New perspective on galaxy clustering as a cosmological probe: General relativistic effects*, Phys. Rev. D **80**, 083514

Yoo J., 2010, *General relativistic description of the observed galaxy power spectrum: Do we understand what we measure?*, Phys. Rev. D **82**, 083508

Zaldarriaga M., Seljak U., 1996, *A Line-of-Sight Integration Approach to Cosmic Microwave Background Anisotropies*, **469**, 437

Zeldovich Yaa B., 1968, *Special Issue: the Cosmological Constant and the Theory of Elementary Particles*, Sov. Phys., Usp., **11**, 381

Zeldovich Yaa B., 1972, *A hypothesis, unifying the structure and the entropy of the Universe*, MNRAS, **160**, 1

Appendix A

Modifying CAMB sources to sample growth rate and bias

In order to consider the *bias free* case we had to modify `CAMB_sources` to accept as (independent) inputs bias and growth rate (parameterized through γ as in Eq. (2.42)). In addition this case does not involve changes in the shape of the real space spectrum, thus one should be able to sample parameter space without the need to compute the transfer functions at each point of parameter space.

To fulfill these needs we have factorized the terms in our observables that depend on the cosmic history (for our reference cosmology) from those that depend on the bias b and growth index γ. The factorization in the case of auto and cross-correlation is given by:

$$
\begin{aligned}
C_\ell^{ii} &= b_i^2 C_\ell^{ii\ (0)} + 2 b_i f_i C_\ell^{ii\ (2)} + f_i^2 C_\ell^{ii\ (4)} && (1) \\
C_\ell^{ij} &= b_i b_j C_\ell^{ij\ (0)} + b_i f_j C_\ell^{ij\ (2)} \\
&\quad + b_j f_i C_\ell^{ij\ (2')} + f_i f_j C_\ell^{ij\ (4)}, && (2)
\end{aligned}
$$

where b_i is the bias of the bin i and f_i is the growth rate given by Eq. (2.42), evaluated at the mean redshift of the bin i. This factorization assumes $f(z)$ does not vary much within the redshift range of the bin (neither b). We have tested this assumption using the exact `CAMB_sources` evaluation or the reconstruction of Eqs. (1,2) and found an excellent match for the bin widths considered in this paper.

Using the observed C_ℓ and solving a linear set of equations using different values for b_i we can store the value of $C_\ell^{ii\ (2)}, C_\ell^{ij\ (2)}, C_\ell^{ij\ (2')}, C_\ell^{ii\ (4)}$ and $C_\ell^{ij\ (4)}$. The values of $C_\ell^{ii\ (0)}$ and $C_\ell^{ij\ (0)}$ are obtaining by excluding RSD in C_ℓ. Then, we sample b and γ space using these factors and the reconstruction given by Eqs. (1) and (2) obtaining C_ℓ^{mod} in parameter space.

In the reconstruction we assume the underlying value of given by the corresponding reference cosmology while the growth factor $D(z)$ is included in the integrals that are contained in the cosmic history dependent factors $C_\ell^{ij\,(n)}$.

When using two tracers α and β, the procedure is the same, using 2 converting i, j into i_α, j_β where α and β can be the same population.